8-2003

Thermodynamics and Kinetics of Defects at Surfaces

Tianjiao Zhang
University of Tennessee - Knoxville

To the Graduate Council:

I am submitting herewith a dissertation written by Tianjiao Zhang entitled "Thermodynamics and Kinetics of Defects at Surfaces." I have examined the final electronic copy of this dissertation for form and content and recommend that it be accepted in partial fulfillment of the requirements for the degree of Doctor of Philosophy, with a major in Physics.

Zhenyu Zhang, Major Professor

We have read this dissertation and recommend its acceptance:

Adolfo Eguiluz, E. Ward Plummer, Hanno Weitering, Ziling Xue

Accepted for the Council:

Carolyn R. Hodges

Vice Provost and Dean of the Graduate School

(Original signatures are on file with official student records.)

To the Graduate Council:

I am submitting herewith a dissertation written by Tianjiao Zhang entitled "Thermodynamics and Kinetics of Defects at Surfaces". I have examined the final electronic copy of this dissertation for form and content and recommend that it be accepted in partial fulfillment of the requirements for the degree of Doctor of Philosophy, with a major in Physics.

Zhenyu Zhang, Major Professor

We have read this dissertation

and recommend its acceptance:

Adolfo Eguiluz

E. Ward Plummer

Hanno Weitering

Ziling Xue

Acceptance for the Council:

Anne Mayhew

Vice Provost and Dean of Graduate Studies

* (Original signatures are on file with official student records)

THERMODYNAMICS AND KINETICS OF DEFECTS AT SURFACES

A DISSERTATION PRESENTED FOR

THE DOCTOR OF PHILOSOPHY DEGREE

THE UNIVERSITY OF TENNESSEE, KNOXVILLE

Tianjiao Zhang

August 2003

Dedication

to

My friends Wu Jun-Ming and Xu De-Ming

My wife, sharing the fate of my life since I knew her

My parents, brother and sister, making me always missing them and the childhood never end

Acknowledgements

I shall thank Dr Zhenyu Zhang for his help ever since I got tangled with him to start my PhD in the University of Tennessee, Knoxville. His characters have changed me quite a lot. And his effort in broadening my world has been a precious gift to me.

I shall thank Drs Robert Compton, Adolfo Eguiluz, Ward Plummer, Hanno Weitering and Ziling Xue for serving in my PhD committer and making their time available to me. Especially I shall thank Dr Plummer for his careful reading and correction of my writings, whenever I give him something.

The efforts from Nikki, Pam and many others in helping my initial relocation to Knoxville are sincerely acknowledged.

Also I shall especially show my appreciation to Dr Chia C. Shih for his effort in helping me to continue my study after more than 3 years of lapse.

Helps from my friends Jiahong, Kuijuan and Ying Lu also eased my life and study here. In my commuting between Knoxville and Oak Ridge, a lot of colleagues had given me their helps in making it not a nightmare. Ali, Danie, Ismail, K.-J., Kuijuan, Jay, Jiandi, John, Jun-hyung, Larry, Ming-Che, Song, Tolik and Wei may be just part of it.

Abstract

Fundamental understanding of the various electronic and structural properties at surfaces is a prerequisite for improved control of nanometer-scale patterning of surfaces for potential technological applications. In this dissertation, we have used multi-scale theoretical approaches to investigate the thermodynamic and kinetic properties of a few elemental types of surface defects. The multi-scale approaches range from first-principles calculations within density functional theory to empirical embedded atom method (EAM) to statistical analysis to kinetic Monte Carlo simulations. In studying the thermodynamic properties of intrinsic line defects on a vicinal TaC(910) surface, our Monte Carlo simulations in comparison with scanning tuning microscope (STM) images have established the existence of long-range attractive interaction between the steps. For extrinsic point defects underneath a GaAs surface, we have established through our theoretical analysis in comparison with STM observations that many-body effects in a system with purely repulsive interactions can give rise to an effective attractive interaction between the dopants at high dopant densities. In the study of the morphological evolution of monatomic-layer-high islands grown on metal surfaces, we have carried out Kinetic Monte Carlo simulations to demonstrate the importance of the island corner barriers. Our study has shown that if the island corner barrier effect is operational in preventing adatoms

located at an island edge to reach a neighboring edge defining the island corner, the islands thus formed must be non-compact, and develop fractal or dendritic shapes. Based on our EAM calculations of the diffusion barriers for various atomic processes and rate equation analysis, we have explained why fractal islands have rarely been observed on metal fcc(100) surfaces. For ideal surfaces, we have investigated the various driving forces for lattice relaxation based on first-principles calculations, and have proposed a new approach that has the promise to predict the direction of relaxation of the atoms in the surface layer strictly based on bulk properties of the given system. Finally, our fist-principles based interpretation of STM images within the framework of the Tersoff-Hamann theory has resulted in good agreement with STM experiments in revealing the anisotropy of electron density corrugations on several open metallic surfaces.

Table of Contents

List of Tables

List of Figures

Chapter 1 Introduction

The overall trend in device miniaturization has been a persistent driving force for fundamental research. Recent progress in nanotechnologies has increased the likelihood of eventual mass production of nanometer-scale devices with atomic-scale precision. As such devices become smaller and smaller, their surface-to-volume ratios keep increasing accordingly, making it more stringent to fully understand and control the various properties of the surfaces and interfaces involved. In particular, the structural properties of the surfaces, interfaces, and thin films will greatly influence the overall performance and stability of the devices. It is therefore scientifically intriguing and technologically significant to study on a fundamental level various structural properties of surfaces, interfaces, and thin films.

A surface is created when one half of the volume of an ideal and infinitely large solid is removed in a Gedanken experiment. Such an ideal surface thus created is of course energetically unstable, and various electronic and atomic relaxations are bound to take place. As a simple form of relaxation, the atomic positions in the surface region preserve their registry as in the bulk in the directions parallel to the surface, but adjust the interlayer spacings in the direction perpendicular to the surface. To reliably determine the directions and magnitudes of the interlayer relaxations at a surface is by no means a trivial exercise, as we will demonstrate in the present thesis

for the cases of metallic systems. It is also quite common that the atoms in the top few layers lose their registry in the parallel directions, as manifested in various fascinating forms of surface reconstruction. One well-known example of symmetry reduction via surface reconstruction is the (7x7) reconstruction of Si(111) as observed by Binnig et. al. using the scanning tunneling microscopy (STM) [1]. The structure of Si(111)-(7x7) reconstruction was later theoretically clarified by Takayanagi and coworkers [2](see Figure 1.1). As it turned out, the invention of STM is perhaps the most important development in surface science over the past few decades, enabling dramatic advances in microscopic understanding of various structural, thermodynamic, dynamic, and kinetic properties and processes at the surfaces of a wide variety of systems. Furthermore, STM has also been proven to be a powerful tool for nanopatterning and nanofabrication at surfaces [3]. As an important preparation step of the present thesis project, we will use specific examples to demonstrate the working principles and important applications of the STM in characterizing surface electronic properties.

If understanding the structural and electronic properties of an infinitely flat surface is challenging, the physics involved is further greatly enriched by the fact that in the real world, any surface unavoidably contains many defects. Such defects can be classified into different kinds following the classic work of Burton, Cabrera and Frank (BCF) [4]. In the BCF model, a surface contains terraces, ledges (or steps),

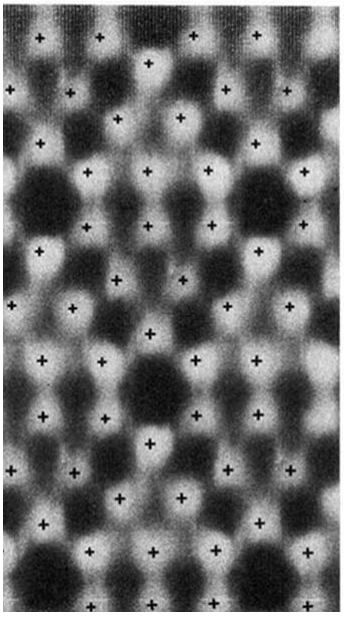

(a)

(b)

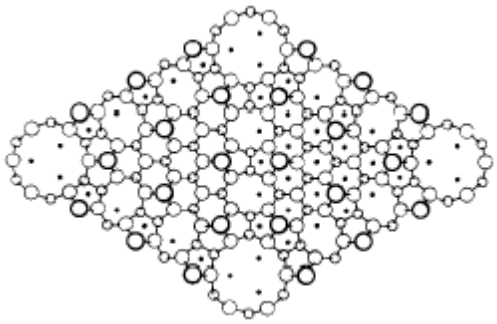

Figure 1.1 Reconstructed Si(111)-(7x7) surfaces. (a) First observation with the STM [1]; (b) the proposed theoretical model for the 7x7 reconstruction [2].

and kinks. The ledges or steps are one kind of line defects, and the kinks along the ledges are viewed as point defects along the line defects. Atoms adsorbed on the terraces (or adatoms), and vacancies are other common types of point defects. Furthermore, in many cases point defects on surfaces are actually in thermal equilibrium with point defects in the bulk, and for this reason a complete understanding of surface properties also require knowledge about defect properties underneath a surface. An example of understanding point defects inside a compound semiconductor will be demonstrated, together with its connection with corresponding defect properties on the surface.

The central theme of the thesis is to investigate, using multi-scale theoretical approaches, the thermodynamic, kinetic, and dynamic properties of surface defects in a few representative model systems. The thermodynamic properties include the equilibrium distribution of steps on a vicinal surface of an ionic metal substrate under the influence of long-range step-step interactions, and many-body effects in dopant clustering inside a compound semiconductor. As examples of kinetic and dynamic properties, we elucidate the importance of certain atomic rate processes in determining the morphological evolution of monatomic-layer-high islands on metal surfaces. The multi-scale approaches invoked range from first-principles calculations within density functional theory to empirical embedded atom method to statistical analysis to kinetic Monte Carlo simulations.

The scientific rationals behind such studies are twofold. First, a precise understanding

of the properties of such intrinsic and external line and point defects in principle should offer us potential new opportunities in the drive for nanopattening of surfaces. In this regard, we refer to two recent examples. The first is the formation of Ag nanoclusters with a narrow size distribution on a strain-induced network of surface superstructure formed when 2 monolayers (ML) of Ag are deposited on a Pt(111) substrate [5] (Figure 1.2(a)). Here the narrow size distribution is achieved because atoms deposited within one unit cell of the superstructure cannot escape from the cell if the growth kinetics are carefully controlled, making them self-assembled into a single cluster. In the second example, beautiful arrays of metal nanoclusters with identical size and equal spacing have been achieved most recently, again taking advantage of self-assembly of adatoms induced by the surface reconstruction together with a fine tuning of the growth kinetics [6] (Figure 1.2(b)). It is anticipated that, atomic steps on a vicinal surface bunched together can significantly suppress the meandering of the steps and the populations of kinks, making such systems ideal templates for growth of low-dimensional structures such as quantum well superlattices [7], quantum wires [8], and quantum dots [9]. Needless to say, the point defects may also significantly influence the structures to be formed on a surface. These considerations illustrate at least partially the underlying motivations of the research projects to be presented in the thesis.

Another major theme of the thesis is to identify the ultimately important atomic rate processes determining the compactness of monatomic-layer-high islands formed

(a)

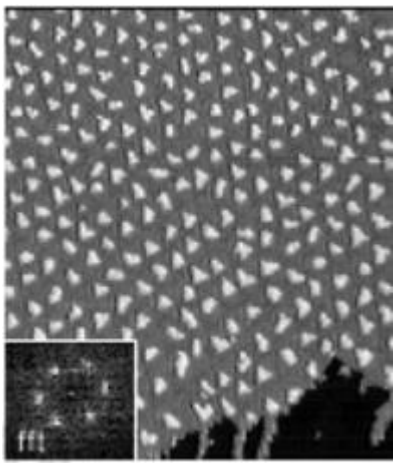

(b)

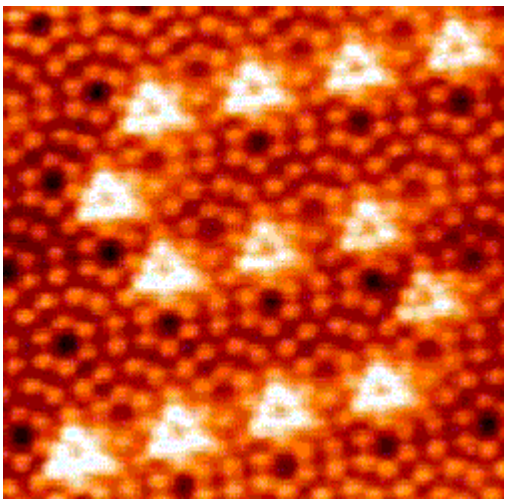

Figure 1.2 Nanoclusters formed on reconstructed substrates. (a) STM image of Ag nanoclusters formed on the reconstructed substrate of 2MLAg/Pt(111)[5]. (b) STM image of In nanoclusters formed on Si(111)-(7x7) surface. Each nanocluster contains precisely six In atoms, and at higher coverages the magic In clusters form spatially ordered arrays [6].

on a surface in the initial stages of epitaxial growth. As mentioned in the two examples of nanocluster formation on 2MLAg/Pt(111) and Si(111)-(7x7), even in the cases where the surface superstructures played essential roles in leading to the self-assembly of the adatoms, proper controls of the growth kinetics (deposition rate, substrate temperature, etc.) was still essential. In the case of nanopatterning via island formation on an elemental surface without reconstruction, proper control of the atomic rate processes involved would be ever more crucial.

The dissertation is organized as follows. First, in Chapter 2, I present brief coverage of the theoretical methodologies employed in carrying out the studies presented in the rest of the thesis. Then as preparation efforts, I present in Appendix A some generic discussions about lattice relaxation of an ideal surface, and propose a new method that has the promise to predict the direction of relaxation of the atoms in the surface layer strictly based on bulk properties of the given system. These studies are carried out using first-principles calculations within density functional theory. Also presented as a preparation step, in Appendix B we show how to interpret the STM images as taken on a few representative metal surfaces. Here the calculations are again first-principles based, within the framework of the Tersoff-Hamann theory [10].

After those preparation studies, we move on to the three major chapters of the thesis, all of which motivated by intriguing experimental observations using the STM. In Chapter 3, I present the results from a study of the thermodynamics of the intrinsic

line defects in surfaces. Specifically, I will consider the step-step interactions on a vicinal surface of TaC(910), and use Monte Carlo simulations in comparison with STM results to establish the existence of long-range attractions [11].

Chapter 4 is focused on studies of one type of extrinsic point defects underneath surfaces. Here we use statistical mechanics and Monte Carlo simulations to explain the STM observation of the clustering of charged Zn dopants in GaAs. Through our theoretical analysis, it is established that many-body effects in a system with purely repulsive interactions can give rise to an effective attractive interaction at high dopant densities [12]. The present study may have an important impact on better understanding and possibly overcoming the fundamental solubility limits in doping of semiconductors.

In Chapter 5, we study the morphological evolution of island grown on surfaces. Here we first carry out Kinetic Monte Carlo simulations to study the effect of island corner barrier on island morphologies. We will show that, if the island corner barrier effect is operational in preventing adatoms located at an island edge to reach a neighboring edge defining the island corner, then the islands thus formed must be non-compact, in the form of fractal or dendrite. We will further explain why fractal islands have rarely been observed on fcc(100) surfaces, based on embedded atom method (EAM) calculations and rate equation analysis [13].

Finally, Chapter 6 presents a summary of the main findings of the thesis.

Chapter 2 Methodologies

As mentioned in Chapter 1, typical surfaces contain many defects. Studies of surface defects are usually carried out using both first-principle and semi-classical approaches, corresponding to different degrees of approximation. In our research, we mainly use Monte Carlo (MC) simulations [14] to study thermodynamic properties of defects, such as the intrinsic step-step interactions on a vicinal TaC(910) surface [11] and extrinsic dopant-dopant interactions underneath GaAs surfaces with Zn as the dopant [12]. In the study of the nucleation mechanisms in initial stages of epitaxial growth [13], we use Kinetic Monte Carlo (KMC) simulations [15]. The difference between MC and KMC will be explained later. We also use Embedded Atom Method (EAM) [16] to calculate the essential adatom diffusion barriers on fcc(100) surfaces. These EAM results serve as good estimates for the diffusion barriers used in the KMC simulations of morphological evolution of the two-dimensional (2D) islands [13]. For more accurate calculations of the diffusion barriers, ab initio calculation is the direction to pursue. Nevertheless, when the system of interest has very low symmetry, such as the motion of adatom around a fractal island on a surface, it is still beyond the scope of ab initio calculation, which makes EAM a plausibly compromised alternative. In our calculation of surface relaxation [17] and STM image [18], ab initio calculation is the main method. In the following, we give a short

description for each of the three main methods used: ab initio, EAM, and MC/KMC. Descriptions of many other analytic approaches employed, such as rate equation, distribution function, pair correlation function, Green function, and tensor analysis, will be scattered in the respective chapters.

2.1 Ab Initio Method

In 1964, Hohenberg and Kohn rigorously proved that the ground state energy of an interacting inhomogeneous electron gas in a static potential *v(r)* can be written as:

$$E=\int v(\mathbf{r})n(\mathbf{r})\,d\mathbf{r}+\frac{1}{2}\int\int\frac{n(\mathbf{r})n(\mathbf{r}')}{|\mathbf{r}-\mathbf{r}'|}\,d\mathbf{r}\,d\mathbf{r}'+G[n] \qquad (1)$$

where *n(r)* is the electron density, and G[n] is a universal functional of the electron density [19]. However, in their original work, there is no suggestion on an explicit *form* of the functional that links the energy and the electron density.

One year later, Kohn and Sham proposed the local density approximation (LDA) of the exchange-correlation energy and made it possible to accurately calculate the total energy of systems with "slowly varying or high density" [20]. Within the Kohn-Sham theory, we have

$$G[n]\equiv T_s[n]+E_{xc}[n] \qquad (2)$$

where T_s[n] is the kinetic energy of a *non-interacting* system with electron density n.

$E_{xc}[n]$ is defined as the exchange-correlation energy of an *interacting* system with electron density n. For a system where its Wigner-Seitz radius (r_s) is much shorter than the typical length (r_0) over which there is appreciable change in electron density, namely, a system with slowly varying density, $E_{xc}[n]$ can be approximated by the exchange-correlation energy per electron $\varepsilon_{xc}(n)$ of a *uniform* electron gas with density n :

$$E_{xc}[n] = \int n(\mathbf{r}) \epsilon_{xc}(n(\mathbf{r})) \, d\mathbf{r} \qquad (3)$$

The error involved is of the order of $(r_s/r_0)^4$. In the high-density regime where r_s is much smaller than the Bohr radius a_0, E_{xc} is in the order of r_s/a_0 smaller than the kinetic energy T_s, and the error in the above local density approximation is negligible.

Within the above framework, they established a procedure to self-consistently calculate the total energy of a system by taking an initial electron density distribution as the beginning of the iteration. In regions where the above approximations do not apply, such as adatoms on surfaces or the overlapping regions in molecules [20], non-local correction is needed, which is the subject of the more recent development of the generalized gradient approximation (GGA) [21].

In our calculations of surface relaxation and STM images, we use the WIEN97 [22] code. It is a full-potential method with linear augmented plane wave (LAPW) basis, and has GGA build-in [22].

2.2 The EAM Approach

For physically realistic systems, there are many defects with no or severely reduced symmetry, and ab initio calculations would demand construction of huge unit cells. However, self-consistent determination of the electron densities of such systems with huge unit cells is very slow and computationally expensive. Therefore, to determine the structure and properties of such large systems, coarser approximations often become unavoidable, with the input of some essential parameters derived from experiments or ab initio calculations of smaller or idealized systems.

One typical example along this line of the approach is the embedded atom method (EAM). According to density function theory [19], the total electronic energy for an arbitrary arrangement of nuclei can be written as a unique functional of the total electron density. EAM [16] is based on the fact that usually the total-electron density in a metal can be well represented by the linear superposition of the contributions from the individual atoms. The electron density in the vicinity of each atom can then be expressed as a sum of the density contributed by the atom in question plus the electron density from all the surrounding atoms. As this latter part is a slowly varying function in space, within the EAM it is assumed to be a constant. This defines an embedding energy as a function of the background electron density and the atomic species, which is given in the following formula:

$$E_{tot} = \sum_i F_i(\rho_{h,i}) + \frac{1}{2}\sum_i \sum_{j(\neq i)} \phi_{ij}(R_{ij}) \qquad (4)$$

Here, $\rho_{h,i}$ is the host electron density at atom i due to the remaining atoms of the system, $F_i(r)$ is the energy to embed atom i into the background electron density ρ, and $\phi_{i,j}(R_{ij})$ is the core-core pair repulsion between atoms i and j separated by distance R_{ij}. (Note that F_i only depends on the elements of atoms i and j.) The electron density is, as stated above, approximated by the superposition of the atomic densities. Details about how to construct these quantities are given in Chapter 5.

In our study of the essential diffusion barriers against adatom motion on metal surfaces, we have used EAM to calculate the energy of a given configuration along the diffusion path. The results from such EAM calculations enable us to establish certain qualitative understanding of the trends of island formation on various metal surfaces.

2.3 (Kinetic) Monte Carlo Simulations

Since the introduction of Metropolis walk [14], Monte Carlo simulations has been frequently employed to study both the dynamic and the static behaviors of large systems. The reason is because of the fact that for large systems, the energetically most favorable configuration is usually extremely difficult to determine reliably from analytic approach and the ensemble of the possible configurations is simply too large

to do calculations configuration by configuration.

In systems where thermal equilibrium is established, the simulation is used to generate the statistically most important configurations. The Metropolis walk [14] samples the configuration space to find the states of the lowest free energy. The sequence of the configurations generated during the simulation does not necessarily correspond to the real evolution of the system towards the states of the lowest free energy. But because the intermediate transient states are statistically unimportant, MC simulations provide an efficient way to reach the equilibrium state.

In studying the kinetics of non-equilibrium phenomena such as those taking place during epitaxy, the sequence of configurations generated by the Monte Carlo procedures becomes important. Therefore, one must invoke kinetic Monte Carlo simulations in order to avoid missing the metastable but physically important configurations.

In general, the execution of Monte Carlo simulations can be described by the following stochastic process [23]:

$$\frac{dP(f,t)}{dt} = \sum_{i \neq f} \frac{w(i,f)P(i,t)}{\tau} - \sum_{i \neq f} \frac{w(f,i)P(f,t)}{\tau} \qquad (5)$$

Here P(f,t) is the probability distribution of configuration f at time t, and w(i,f) is the probability of a successful hop from the configuration i to f. $1/\tau$ can be taken as the attempt frequency. In most practical applications, w(i,f) takes the following form [14,15]:

$$w_m(i,f) = e^{-\frac{\delta E}{k_B T}} \quad \text{for } \delta E > 0$$
$$= 1 \quad \text{for } \delta E \leq 0 \qquad (6)$$

For MC simulations, $\delta E = E(c_i) - E(c_f)$; while for KMC simulations, $\delta E = E(c_b) - E(c_i)$. (See Figure 2.1).

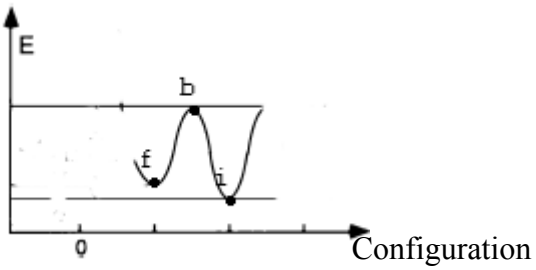

Figure 2.1 Configuration changes in (Kinetic) Monte Carlo simulations.

Chapter 3 Step-Step Interactions on Vicinal Surfaces

3.1 Introduction

In this chapter, we describe the properties of intrinsic line defects existing on the surfaces. When we create some new surface structure, there is always some vicinality away from an ideal crystalline index. On a vicinal surface, its macroscopic surface index forms small angle to a low index crystal face. In the ideal case, a vicinal surface consists of terraces of the low index plane, separated by regularly spaced monatomic steps. In reality, the spacing is never perfectly regular, as the surface reconstructs to form thermodynamically more stable structures. The step height can vary from one step to another. The width of step separation also has a broad distribution instead of some sharp peaks. Furthermore, atoms may meander along the steps.

The existence of steps on a surface is not necessarily a bad thing. As stated by Lagally [24], "a surface may actually be 'too good' for the best film growth because it contains too few steps". There have been studies of the stability of vicinal surfaces because of their technological importance in serving as templates for epitaxial growth of well-ordered thin film systems and nano devices [7,8,9,25,26].

Because the spatial distribution of these line defects is defined on a scale

much larger than the atomic distance, there has been a long tradition of utilizing macroscopic concepts such as surface stress, surface strain and surface energy to analyze their properties. As STM becomes popular in observing surface morphologies, it is now possible to verify the validity of classical models and the step dynamics from microscopic results. For example, recent quantitative studies of the terrace width distribution have allowed determination of the nature of step-step interactions [26-33].

Theoretical determination of step-step interaction and its dependence on the distance between steps can be obtained in two ways. One involves simulations, as to be demonstrated in our analysis of the step-step interaction on a TaC(910) surface. The other employs theory of elasticity and thermodynamics, as demonstrated in the classical works of Marchenko and Parshin [34] and Andreev and Kosevich [35].

In the following, we will review some basic concepts used in the continuous theory of elasticity, such as strain and stress tensors. Based on these, we will deduct in detail the step-step interactions on vicinal surfaces. Afterwards, we will explore the microscopic interactions that have been included in such a macroscopic description. Beyond this microscopic origin, we will consider other possible step-step interactions on vicinal surfaces. For the purpose of clarity and completeness, we have used these literature as our major references: Landau and Lifshitz [36], Marchenko and Parshin [34], Andreev and Kosevich [35], Steward, Poland, and Gibson [37], Ibach [25], Redfield and Zangwill [25]. In the end, we will give our studies of step-step

interaction on TaC(910) surfaces.

3.2 Description of Surfaces within Continuous Theory of Elasticity

In this section, our derivation mainly follows that of Landau and Lifshitz [36].

3.2.1 Strain tensor

Let us put a solid in an abstract space **S**. Different parts of the solid are measured and represented in this virtual space. Under the action of external forces, because of the lack of strict rigidity, the solid bodies exhibit deformation to some extent, i.e., they change in shape and volume. All measures of length, area and volume are still carried out in this virtual space **S**. Before and after the deformation, the extensions of the same body in the space may be different. When measured within this space, its density can be different as well. Here we only consider external forces that cause *no* movement of the center of mass of the solid.

The deformation of a body is described mathematically in the following way. *Before* the deformation, let vector **r** (with components x_1,x_2,x_3) represents the position of one point in the body as located in the space S. In the neighboring region of this point, we assign a small volume dV to it. *After* the deformation, this point will make small shift; we use **r'** to denote the new position, which is a function of **r**. The mass

inside the volume dV is also likely to occupy a different amount of space dV'. The displacement of this point due to the deformation is denoted as:

$$\mathbf{u(r)} = \mathbf{r'} - \mathbf{r} \qquad (1)$$

If **u** is known as a function of **r**, the deformation of the body is completely determined.

Under the condition that the deformation is small, which means that there is no mass flow and neighboring atoms are still neighboring atoms, we can take the differential form of Eq. (1) and get

$$\mathbf{dr'} = \mathbf{du} + \mathbf{dr} \qquad (2)$$

After the deformation, the change of distance *l* between two points has the following relation:

$$dl'^2 = dl^2 + 2\frac{\partial u_i}{\partial x_k} dx_i dx_k + \frac{\partial u_i}{\partial x_k}\frac{\partial u_i}{\partial x_l} dx_k dx_l \qquad (3)$$

Here $dl'^2 = |\mathbf{dr'}|^2, dl^2 = |\mathbf{dr}|^2$. In a simplified and symmetric form, Eq (3) can be written as $dl'^2 = dl^2 + 2u_{ik} dx_i dx_k$ (4)

where

$$u_{ik} = \frac{1}{2}\left(\frac{\partial u_i}{\partial x_k} + \frac{\partial u_k}{\partial x_i} + \frac{\partial u_l}{\partial x_i}\frac{\partial u_l}{\partial x_k}\right) \qquad (5)$$

The tensor u_{ik} is called strain tensor, which is symmetric. Like any symmetrical tensor[36], we can diagnolize this tensor by choosing its principal axes.

If we further assume that the deformation is so small that we can neglect the

second or higher order contributions of the deformation in measuring the dimensions, the volume change under the deformation is

$$dV' = (1 + u_{ii})dV \qquad (6)$$

In obtaining the above term, we have also taken into account the fact that the sum of the principal values of a tensor is invariant.

3.2.2 Stress tensor

Suppose that before the application of the external force, the solid we considered above is in such a state that the arrangement of the atoms leads all parts of the solid in mechanical equilibrium. Here the mechanic equilibrium has statistical meaning, in the sense that physical quatities are measured in a reasonably long time t so that the time average of the position

$$\mathbf{r} = \frac{1}{\tau}\int_{t}^{t+\tau} \mathbf{r}(t_1)dt_1 \qquad (7)$$

is a constant independent of t and a longer t gives the same constant. Displacements or vibrations within a time scale shorter than τ gives the thermal energies of the solid.

Upon the application of the external force $f_i^{ex}(\mathbf{r})$, the atoms respond by displacements, leading to a macroscopic deformation of the solid. After certain time, atoms arrive at their new mechanic equilibrium. In this state, there exists internal force $f_i^{in}(\mathbf{r})$ at each point such that

$$f_i^{in}(\mathbf{r}) + f_i^{ex}(\mathbf{r}) = 0 \qquad (8)$$

Next, we assume that *the atomic forces have a very short range of action*, such that the effect of these atomic forces extends only to the neighborhood of the atom exerting them, over a distance of the same order as that between the atoms [36]. This restriction implies that we exclude cases such as pyroelectic and piezoelectric materials where the deformation of the solid results in macroscopic electric fields [36]. Under these restrictions, we have a well-defined mathematical problem in which the resultant force on a tiny volume dV of the solid is an infinitesimal quantity and is proportional to the volume dV. Under this condition, $f_i(\mathbf{r})$ has the physical meaning of force *density* at position **r**.

Next we consider the virtual work done by the internal force. Given a tiny deformation $\boldsymbol{\delta u(r)}$ of the solid, the work done by the internal forces is

$$\int \delta W dV \equiv \int f_i^{in}(\mathbf{r})\, \delta u_i dV \qquad (9)$$

Next we introduce a symmetric tensor σ_{ik} such that

$$f_i^{in}(\mathbf{r}) = \frac{\partial \sigma_{ik}}{\partial x_k} \qquad (10)$$

Then Eq. (9) becomes

$$\int \delta W dV = \oint \sigma_{ik}\, \delta u_i dS_k - \int \sigma_{ik} \frac{\partial \delta u_i}{\partial x_k} dV \qquad (11)$$

Let us further assume that the external force does not cause deformation at the infinite boundary of the solid, then the first term representing the surface integration at the infinity of the solid is zero. Taking the symmetric form of the tensor

σ_{ik} and the definition of strain tensor in Eq. (5), we get:

$$\int \delta W dV = -\int \sigma_{ik} \delta u_{ik} dV \qquad (12)$$

This indicates that the tensor σ_{ik} is a conjugate quantity associated with the strain tensor, therefore it is called stress tensor. It is essential to notice that the stress tensor is not uniquely defined. Any transformation of the following form is acceptable since it gives the same force:

$$\tilde{\sigma}_{ik} = \sigma_{ik} + \frac{\partial \chi_{ikl}}{\partial x_l} \qquad (13)$$

A proper choice of χ_{ikl} can make it symmetric [36].

3.2.3 Thermodynamics of the deformation [36]

Now we consider the recovery process after the removal of the external force. Suppose this process is reversible. In unit volume, the change of internal energy U can be related to the absorption of heat Q and the work done by the solid W as:

$$\begin{aligned} dU &= dQ - dW \\ &= TdS + \sigma_{ik} du_{ik} \end{aligned} \qquad (14)$$

The change of the free energy per volume F is

$$dF = -SdT + \sigma_{ik} du_{ik} \qquad (15)$$

The stress tensor can be expressed as

$$\sigma_{ik} = \left(\frac{\partial F}{\partial u_{ik}}\right)_T \qquad (16)$$

For a small deformation, the free energy of the system can be expanded as a function of the strain tensor. In general,

$$F = \frac{1}{2} \lambda_{ikm} u_{ik} u_{lm} \qquad (17)$$

For an isotropic system, it can be further simplified as

$$F = \frac{1}{2} K u_{ll}^2 + \mu (u_{ik} - \frac{1}{3} \delta_{ik} u_{ll})^2 \qquad (18)$$

in which K and μ are the bulk and shear modulus respectively.

The stress tensor for an isotropic system then becomes

$$\sigma_{ik} = K u_{ll} \delta_{ik} + 2\mu (u_{ik} - \frac{1}{3} \delta_{ik} u_{ll}) \qquad (19)$$

3.2.4 Differential equation for the deformation field **u(r)** of an isotropic solid [36]

Here we look at the distribution of the displacement field caused by the external force. If the deformation is very small and is elastic [36], after substituting (19) and the symmetric form of the strain tensor (5) into the mechanical equilibrium equation (8), we get

$$\mu \frac{\partial^2 u_i}{\partial x_k^2} + (K + \frac{1}{3}\mu) \frac{\partial^2 u_k}{\partial x_i \partial x_k} + f_i^{ex}(\mathbf{r}) = 0 \qquad (20)$$

or

$$\mu \Delta \mathbf{u} + (K + \frac{1}{3}\mu) \nabla (\nabla \cdot \mathbf{u}) + \mathbf{f}^{ex}(\mathbf{r}) = 0 \qquad (21)$$

In the following, the method adopted in Ref. [36] is used. Also we suppose

the external force only exists on the surface. We seek a solution in the following form

$$\mathbf{u} = \xi + \nabla \varphi \qquad (22)$$

in which φ is a scalar, and the vector ξ fulfills the Laplace equation:

$$\Delta \xi = 0 \qquad (23)$$

Then we get the following equation

$$2(1-\sigma)\nabla(\Delta\varphi) + \nabla(\nabla \cdot \xi) = 0 \qquad (24)$$

in which σ is defined as

$$\sigma = \frac{1}{2}\frac{(3K - 2\mu)}{3K + \mu} \qquad (25)$$

In the case of simple extension or compression of a rod, the above quantity has the meaning of Poisson's ratio [36]. We can further simplify Eq.(24) after we integrate it and neglect the integration constant, which leads to

$$2(1-\sigma)\Delta\varphi = -\nabla \cdot \xi \qquad (26)$$

3.2.5 Green's function for the displacement field on the surface

In the following, we consider a system occupying the half space z>0. The force distribution is concentrated at the origin (x,y,z = 0,0,0),

$$\mathbf{f}^{ex}(\mathbf{r}) = \mathbf{F}\,\delta(x)\,\delta(y)\,\delta(z) \qquad (27)$$

For z>0, we need to solve the equation (26). First, let us look at the boundary condition. Integrating Eq.(8) and using the force given in Eq.(27), we get

$$\int dydz\,\sigma_{i1}((+\infty,y,z)-\sigma_{i1}(-\infty,y,z))+\int dzdx\,\sigma_{i2}((x,+\infty,z)-\sigma_{i2}(x,-\infty,z))$$
$$+\int dxdy\,\sigma_{i3}((x,y,0)-\sigma_{i3}(x,y,-\infty))+\int F_i\,\delta(x)\,\delta(y)dxdy=0 \quad (28)$$

Because we assume that the effect of the force disappears at infinity, the above equation is simplified to

$$\sigma_{i3}(x,y,0)=-F_i\,\delta(x)\,\delta(y) \quad (29)$$

The left deduction follows that in [36] and is omitted here. For the specific force given in Eq (27), the distribution of the displacement field is

$$u_i=G_{ik}(x,y,z)F_k \quad (30)$$

where G_{ik} takes the role of the Green's function and is given by the following matrix

$$G_{ik}(x,y,z)=\frac{1+\sigma}{2\pi E}\begin{pmatrix}\frac{2(1-\sigma)r+z}{r(r+z)}+\frac{x^2[2r(\sigma r+z)+z^2]}{r^3(r+z)^3} & \frac{xy[2r(\sigma r+z)+z^2]}{r^3(r+z)^3} & \frac{xz}{r^3}-\frac{(1-2\sigma)x}{r(r+z)}\\ \frac{xy[2r(\sigma r+z)+z^2]}{r^3(r+z)^3} & \frac{2(1-\sigma)r+z}{r(r+z)}+\frac{y^2[2r(\sigma r+z)+z^2]}{r^3(r+z)^3} & \frac{yz}{r^3}-\frac{(1-2\sigma)y}{r(r+z)}\\ \frac{xz}{r^3}+\frac{(1-2\sigma)x}{r(r+z)} & \frac{yz}{r^3}+\frac{(1-2\sigma)y}{r(r+z)} & \frac{2(1-\sigma)}{r}+\frac{z^2}{r^3}\end{pmatrix} \quad (31)$$

Here

$$E=\frac{9K\mu}{3K+\mu} \quad (32)$$

and it has the physical meaning of Young's modulus [36]. For an arbitrary surface force $f_i(x,y)$, the displacement field is given by

$$u_i=\int G_{ik}(x-x',y-y',z)f_k(x',y')dx'dy' \quad (33)$$

3.3 Elastic Theory of Step-Step Interactions on Vicinal Surfaces

3.3.1 General derivation of the step-step interactions

On the surface of a crystal, there are many steps. Her we deduct the interaction between two steps. The influence of the step atoms on the surface is illustrated in Figure 3.1 [37]. All the actions and influence of the atoms of the two steps on the properties of the substrate are included in the forces acting on the flat surface, which are $f_i^{(1)}(x)$ and $f_i^{(2)}(x-d)$ per area respectively. Here the two steps run along the y-axis and are separated by d. The induced displacement fields by these two steps are

$$u_i(x,y,z) = \int G_{ik}(x-x',y-y',z)(f_k^{(1)}(x') + f_k^{(2)}(x'-d))dx'dy' \qquad (34)$$

Now let us consider the work done by these two forces. This work should be equal to the change of energy in the surface. Because these forces are limited in the surface, i.e. z=0, we can write the work per unit length along the y axis as

$$w = \int dxdx'[(f_i^{(1)}(x) + f_i^{(2)}(x-d))(f_k^{(1)}(x') + f_k^{(2)}(x'-d))]\int dy'G_{ik}(x-x',y-y',0) \qquad (35)$$

The interaction part then becomes

$$w_{int} = \int dxdx'[f_i^{(1)}(x) * f_k^{(2)}(x'-d) + f_i^{(2)}(x-d) * f_k^{(1)}(x')]\int dy'G_{ik}(x-x',y-y',0) \qquad (36)$$

Here, how to choose or justify a reasonable force distribution because of the presence of the step is a matter of controversy [34-35,37,81,39-40]. Let us first obtain the integration of the Green's function to learn about how far the interaction can propagate through the substrate,

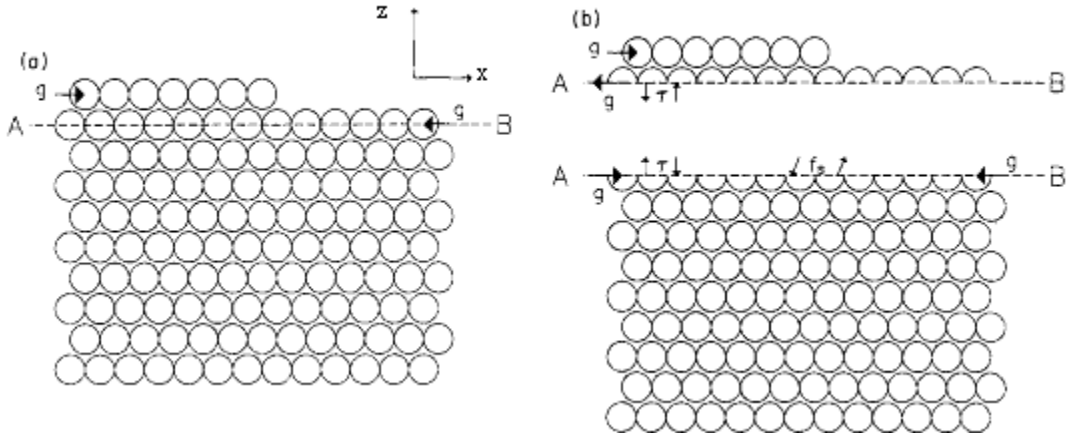

Figure 3.1 Illustration on how to treat the effect of a step. It assumes that the plane AB communicates all the influence of the step atoms on the substrate [37].

$$\overline{G}_{ik}(x) \equiv \int dy' G_{ik}(x, y - y', 0) \tag{37}$$

First let us suppose the step runs from y'=-L to y'=L. y is a point between the two ends and far away from the boundary. The integrated result is

$$\overline{G}_{ik}(x) = \frac{(1+\sigma)(1-\sigma)}{\pi E} \begin{pmatrix} \overline{G}_{33}(x) + \frac{\sigma}{1-\sigma}(2 - \frac{1}{2}\frac{x^2}{L^2}) & 0 & -\frac{1-2\sigma}{1-\sigma}(\frac{\pi}{2} - \frac{x}{L}) \\ 0 & \overline{G}_{33}(x) + \frac{\sigma}{1-\sigma}(2 - \frac{1}{2}\frac{x^2}{L^2}) & 0 \\ \frac{1-2\sigma}{1-\sigma}(\frac{\pi}{2} - \frac{x}{L}) & 0 & 2\ln 2 + \frac{1}{2}\frac{x^2}{L^2} - \ln(\frac{x^2}{L^2}) \end{pmatrix} \tag{38}$$

Because of the divergence with L, we do not take the infinite limitation of L at this moment.

3.3.2 Step-step interaction with the force distribution proposed by Marchenko and Parshin

Next let us suppose that indeed the stepped surface is subjected to a force distribution as proposed by Marchenko and Parshin [34]. We put it in a more general form as:

$$\begin{aligned} f_1^{(i)}(x) &= F_1^{(i)} \frac{\partial \delta(x)}{\partial x} \\ f_2^{(i)}(x) &= 0 \\ f_3^{(i)}(x) &= F_3^{(i)} \frac{\partial \delta(x)}{\partial x} \end{aligned} \tag{39}$$

In the above equations, i =1,2. $F_1^{(i)}$ and $F_3^{(i)}$ represent the strength of force components tangential (along the x direction) and normal (along the z direction) to the surface,

respectively. They lie in the x-z plane with the x component (z component) equal to the σ_{xx} (σ_{zz}) element of the surface stress tensor associated with the step [35]. There is no force along the steps since these steps are supposed to run freely (along the y direction). Substituting Eqs. (39) and (38) into Eq. (36) and taking the infinite limit of L, we get the following results

$$w_{int} = \frac{4(1-\sigma^2)}{\pi E} \frac{1}{d^2} (F_1^{(1)} F_1^{(2)} + F_3^{(1)} F_3^{(2)}) \qquad (40)$$

We note that this is twice as large as in [34]. The discrepancy may be due to that in their original definition, Marchenko and Parshin only took into account one half of the total interaction energy.

Blakely and Schwoebel [39] also demonstrated long ago that surface stress [40] can drive atomic relaxation in the vicinity of steps, which in turn induces elastic distortions in the bulk. Therefore, the elastic interaction between steps is caused by the displacements of the step atoms relative to the positions these atoms would assume in the bulk.

We can understand the above origin of step-step interaction from the following microscopic argument proposed by Ibach [25], namely, step atoms do not have as many bonds with others as terrace atoms have. According to our studies of the surface relaxation (Appendix 1) taking into accounting the difference of bond numbers, it is not unusual that the step atoms should be displaced relative to the positions of the normal terrace atoms. These displacements cause elastic deformation

of the material around the steps. Based on Eq.(36), the overlapping of the displacements due to neighboring steps causes the step-step interaction. The perpendicular and parallel components of the displacement vectors have different orientation and spatial distributions, as sketched in Figure 3.2. (a) and (b) respectively [25]. The interaction from perpendicular components can be repulsive or attractive, depending on their relative orientations. The parallel components always lead to repulsive interaction, regardless of the relative orientation of the steps.

From Eq. (39) we note that the displacement field is calculated by assuming a pair of line dipole forces at the position of the step, as in the original work of Marchenko and Parshin [34] and Andreev and Kosevich [35]. This is justified as long as the distance between the steps is large compared to the inter-atomic distances [25,43,37]. The $1/d^2$ -dependence given in Eq.(40) has been confirmed experimentally on surfaces vicinal to Si(111) [31], hcp He^4 [44], Cu(1,1,11) [45] and Cu(1,1,13) [33], and by general EAM calculations of Tian et al on Cu(11n) surfaces [33]. However, the strength of the interaction is a matter of controversy. The theoretical and experimental agreement on vicinal Si(111) surfaces is good [31,33,25]. The study on hcp He^4 [44] also agrees well with the result from the estimate of the surface stress [46]. In contrast, on vicinal Cu(11n) surfaces, the theoretical interaction strength is an order of magnitude stronger than experiment values [33]. It is worth to note that the contribution arising from the parallel components is neglected [25] in Si(111) [31].

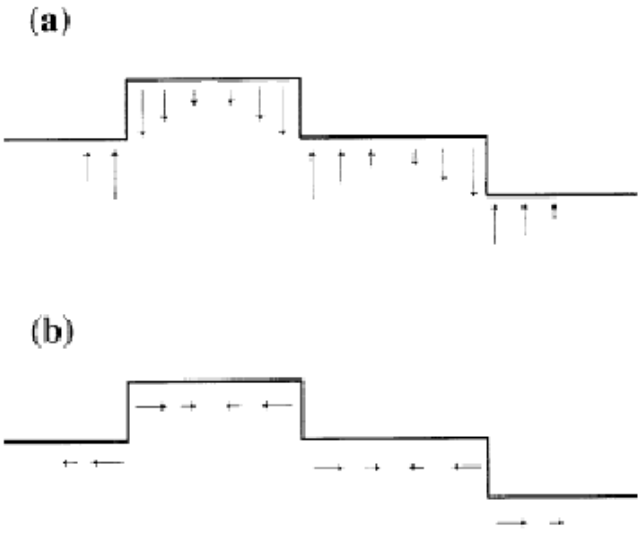

Figure 3.2 Displacements of the step atoms. Displacements are separated into components (a) perpendicular and (b) parallel to the terrace [25].

From Eq. (39), we need more information about the force dipoles in order to have a quantitative value of the interaction strength. Marchenko and Parshin [34] set the perpendicular force dipole $F_3^{(i)}$ equal to the product of the surface stress and the step height, which was confirmed later by considering the torque balance on a stepped surface [37]. However, EAM calculations by Shilkrot et al indicated that Eq. (40) overestimates the perpendicular force dipoles by more than a factor of 2 [40], (or a factor of 4 using our Eq.(40)).

The parallel force dipole $F_1^{(i)}$ was calculated by Andreev and Kosevich [35] to be equal to the first derivative of the step energy with respect to the strain perpendicular to the surface, suggesting that $F_1^{(i)}$ were a quantity that is microscopically unrelated to $F_3^{(i)}$ [25]. However, Shilkrot et al [40] showed that the ratio of $F_1^{(i)}$ and $F_3^{(i)}$ is determined by the elastic constants. For the special geometry they considered, $F_1^{(i)}$ and $F_3^{(i)}$ are about equal. The estimation of the repulsion by this method made the discrepancy between the theory and experiment even larger [25].

From Eq. (40) and Figure 3.2, the constraint of the surface orientation by the substrate makes it very likely that the elastic interaction is purely repulsive [38]. Redfield and Zanwill [38] suggested that it is possible to imagine a symmetry breaking situation in which the atomic distortions near alternative steps differ in such a way that the elastic force becomes attractive. They sketched a scenario on a semiconductor surface [47] where the reconstruction occurs in such a way that the surface stress of the terrace between two closely spaced steps switched from

compressive to tensile (or vice versa). For metal surfaces, since reconstruction is difficult, they excluded such a possibility [38].

It is essential to notice that so far our discussions of the $1/d^2$ elastic interaction is based on the assumption of the force density as indicated in Eq. (39). If we have a successive array of steps with an alternating force density along x direction given by the force monopoles $\pm F_0\delta(x-x_i)$ [81,39,48], the following form of step-step interaction energy per length can be obtained:

$$w_{int} = -\frac{F_0^2}{2\pi}\ln\left(\frac{d}{\pi a}\right) \quad (41)$$

Here a is a microscopic cutoff length, introduced via Lorentzian broadening of the delta function [81]. The intensity of F_0 is the constant to justify the monopole nature of the above force distribution [81,17].

3.4 Other Possible Step-Step Interactions on Vicinal Surfaces

So far we have focussed on effective step-step interaction arising from elastic interactions mediated by the substrate. In the following, we discuss other possible step-step interactions in the literature.

One important type of step-step interaction considered is of entropy nature [49-55]. It was measured on He^4 vicinal surface as well [44]. At high temperatures, steps have many kinks and meander in space. However, the meandering behavior is constrained by neighboring steps, which is the source of the entropic repulsion. It has

been thought that the entropic repulsion is rather weak and the terrace width distribution resulting from entropic repulsion alone is rather broad [25]. It takes the form [53]:

$$w_{entropy} = \frac{2k_B T a_\perp^{\,2}}{d^2 a_\parallel} \frac{\exp(-\varepsilon / k_B T)}{1 + 2\exp(-\varepsilon / k_B T)} \qquad (41)$$

Here $a_\perp$ and $a_\parallel$ represent the microscopic kink protrusion perpendicular to the step and the flatness parallel to the step respectively, and ε is the kink excitation energy.

A $1/d^2$-interaction is also found for the interaction of steps via the electric dipole moment [51] associated with the steps [56-57]. For ionic crystal surfaces, the existence of attractive electrostatic interaction between steps was recognized long long ago in the work of Kossel [58] and Stranski [59] based on the terrace-step-kink model of vicinal surfaces. For metal surfaces, steps do not exhibit net charge but a dipole moment can occur due to the spillout of the electrons in the vicinity of the step [60-61]. The energy of interaction per unit length between two steps is [62]

$$w_{e-dipole} = \frac{2\mathbf{p}_1 \cdot \mathbf{p}_2 - 4(\mathbf{p}_1 \cdot \mathbf{n})(\mathbf{p}_2 \cdot \mathbf{n})}{d^2} \qquad (43)$$

Here, $\mathbf{p}_1$ and $\mathbf{p}_2$ are the dipole moments of the step-charge distributions, and **n** is a unit vector defined by $\mathbf{p}_1$ and $\mathbf{p}_2$. The perpendicular components of the dipole moments cause repulsion, while the parallel components cause an attraction. So far, people have little knowledge about the magnitude of the dipole moment at steps. Evidence that such dipole moments exist is from measurements of the work function

as a function of the step density and the energy contribution of the electric dipole moments appears to be much smaller than the repulsion arising from the elastic strain field as given in Eq. (40) [25]. Given that experimental values for the step-step interaction on Cu(11n) are much smaller than that from Eq. (40) [33] as well, we can not exclude that a possible contribution from the electric dipole moment indeed exists [25].

On metal surfaces it has been suggested that step-step interaction can also be originated from the electronic screening associated with the presence of each step, which is an oscillatory Friedel type of interaction and can be attractive at some distances [28,32,38]. The interaction energy between two adatoms weakly adsorbed onto a flat substrate separated by a large distance d is given as [63-64]:

$$E_{a-a} \sim \frac{1}{d^m} \cos(2k_F d) \qquad (44)$$

The exponent m is equal to 5 for the simplest case where the Fermi energy does not lie in a surface band [38]. Now consider the case where we have two parallel *row*s of atoms weakly adsorbed on a flat substrate and separated by a distance d. As an approximation, the interaction energy between the rows can be computed by simply adding the above atom-atom interaction over all atoms in each row. For small k_F, one finds the asymptotic (large d) result [38]

$$w_{screen} \sim \frac{1}{d^{m-1/2}} \cos(2k_F d + \frac{\pi}{4}) \qquad (45)$$

Note that the interaction falls off with separation more slowly than the atom-atom

interaction given in Eq.(44). Also, it is important to note that Eq.(45) is the energy of two *rows*, not two *steps*. The interaction between two steps is given by summing over all rows in the half planes that constitute the terraces bounded by the steps, which is an oscillatory interaction energy that decays as $1/d^{9/2}$ [38].

3.5 Attractive Step-Step Interactions Observed on TaC(910) Surfaces

In the following, we present our study [11] of the step-step interactions on TaC(910) using scanning tunneling microscopy and Monte Carlo simulations. In particular, we show that a weak, long-range, attractive step-step interaction must be combined with a strong, medium-range, repulsive step-step interaction in order to interpret the measured step separation distribution. The likely physical origin of the atomic-range attractive interaction that leads to the formation of multi-height steps is also discussed.

Generally, when cooled below a roughening temperature T_R, a vicinal surface can undergo a step-bunching (or faceting) transition in which a number of steps bunch closely or coalesce to become a multi-height step [30,65-70]. Based on x-ray scattering data from the vicinal Si(310) surface [30], Song and Mochrie speculated that such step bunching could involve step-step attraction. This speculation has stimulated much theoretical interest, and the faceting has been predicted to arise from a competition between *short-range attraction and long-range repulsion* between the

steps [70-73], where the *short-range is about one atomic spacing.* Earlier, in a paper by Frohn et al. [31], scanning tunneling microscopy images of a sequence of carefully prepared and equilibrated Cu(1,1,19) surfaces vicinal to (100) were presented. A short-range repulsion (1-2 atomic rows) in combination with a medium-range attraction (3-5 atomic rows) has also been used to explain the measured step separation distribution. If such forces exist, it would have important implication for theories of surface phase transitions [47,74], thermal meandering of steps [53], and the kinetics of step motion [75-77,39] as well as the stability of vicinal surfaces [78]. However, despite these observations, the existence of an attractive interaction still remains speculative because there is no clear understanding on how the combination of attractive and repulsive interactions can lead to the experimentally observed step separation distributions. The microscopic origin for the atomic range step-step attraction as assumed in theories [71-73] to explain step bunching remains unknown.

3.5.1 Experimental results

Experiments by Zuo et al were performed in an ultrahigh vacuum chamber with a base pressure ~ 1.0 x 10^{-10} Torr. The chamber was equipped with an STM system, low-energy electron diffraction (LEED) optics, a cylindrical mirror analyzer for Auger electron spectroscopy (AES), and an ion-sputter gun. TaC is an ionic crystal with the sodium chloride structure and has an extremely high melting point, ~ 3983 °C. TaC(910), vicinal to the (100) plane, was cut 6.34° from the [100] direction

towards [010], and polished to the desired orientation to within 0.25°. The surface was routinely cleaned by heating to ~ 2000 °C using electron bombardment. During the heating, the sample housing was cooled by liquid nitrogen to maintain good vacuum. After cleaning, no impurities were detected with AES, and a LEED pattern with spot splitting energy dependence indicative of dominant double-height steps was observed. Note that the high-temperature heating also served as an activation process for faceting. All STM images were taken at room temperature (RT) in the constant current mode with a typical sample bias of 1-2 V and a tunneling current of ~ 1.0 nA.

First, we determine a minimum annealing temperature (T_{min}) at which obvious mass transport occurs on the surface. Below T_{min} the morphology is essentially frozen as the sample is cooled slowly from higher annealing temperatures towars RT. Therefore, the morphology imaged at RT reflects the same morphology at T_{min}. A slow cooling is required in order to get the well-ordered faceting phase below T_R. Figure 3.3 shows the STM images obtained after annealing the sample at different temperatures (T). The dwell time during each annealing process is ~ 60 seconds for T < 1500 °C and ~ 30 seconds for T >1500 °C. (Note that for T ~ 2000°C, 30-second annealing is long enough for the surface to reach a steady state). The lowest annealing temperature at which there is indication of single-height steps is about 1000 °C (Figure 3.3(a)), which also indicates obvious mass transport on the surface at this annealing temperature. The morphology imaged at RT after annealing at T ~ 2000 °C (Figure 3.3(d)) represents an equilibrium morphology frozen in around 1000 °C as the

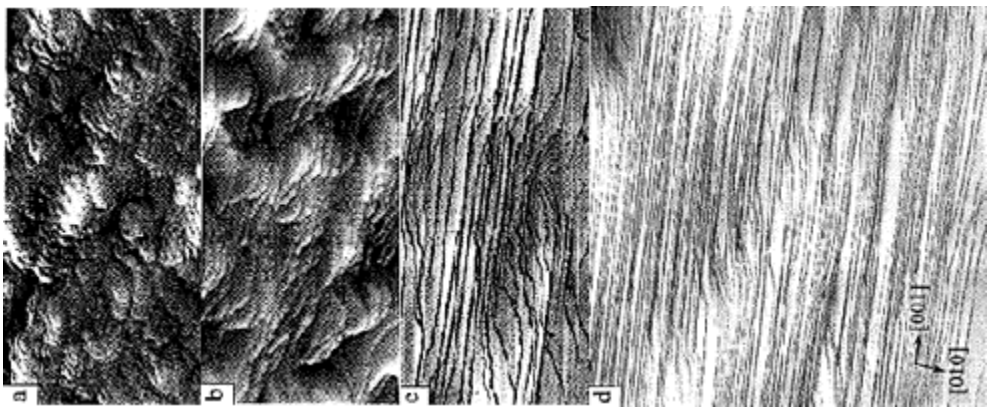

Figure 3.3 STM images of TaC(910) annealed at different temperatures. (a) T = 1000 ºC, (b) T = 1500 ºC, (c) T = 1750 ºC and (d) T = 2100 ºC). The size in (a) - (c) is 1000 x 500 $Å^2$ and in (d) is 3000 $Å^2$.

sample cools slowly, which was confirmed by repeated experiments at $T \sim 2000$ °C with various cooling time.

Other more important features in Figure 3.3 are: (1) single-height steps appear first and are dominant after the lower temperature annealing ($T \leq 1500$ ºC) and these single-height steps merge from off-[001] directions to become multi-height steps along the [001] direction as T increases. At $T \geq 2000$ ºC (Figure 3.3(d)), the step distribution is stabilized and consists of 12% single-, 56% double-, 31% triple-, and 1% quadruple-height steps. (2) These multi-height steps along [001] are very straight, which implies a high kink excitation energy (or very strong bonding) and the step meandering is suppressed.

3.5.2 Short range interaction

Multi-height steps can be regarded as an extreme case of step bunching and the step-wall represents the (010) facet. This phenomenon has also been observed on TaC(n10) (n = 1, 2, 3), where even higher multi-height steps are formed [66,68-69]. The fact that these multi-height steps are only activated at high temperatures is consistent with the existence of the atomic-range attraction between steps as suggested in theories [71-73]. We suggest that an attraction of such a short range can originate from the orbital affinity between broken bonds or electron-density spillout at steps [60-62]. It is important to notice that Lennard-Jones potential is also of short-range type and can be important here since the existence of multi-height step is a

phenomenon in the range of atomic distance. Our calculations of two parallel ionic chains of Ta(+)C(-) indicate that the step-step interaction potential can be well fitted by a Lenard-Jones type function. When the charge center has a relative shift of one atomic distance, it is attractive; when there is no shift, the interaction is repulsive. When a sample is cooled from above T_R where step fluctuations can cause single-height neighboring steps to randomly move together, this short-range attraction can overcome a medium-range repulsion ($2 < x < 13$ atomic rows, see the discussion below) to make neighboring steps coalesce. The formation of multi-height steps reduces the repulsive interaction energies among the single-height steps [66,68-69] because the average step separation must be increased to preserve the net surface orientation. Also, the step-edge energy is lowered by creation of a low-index step-wall facet due to a reduction in the number of broken bonds at steps. Thus the total energy of the multi-height steps is more energetically favorable than the collection of purely single-height steps. This picture is not only consistent with the trend observed for vicinal Si [65,67,30,70,27,79] and TaC surfaces [66,68-69], where steps with larger heights form with increasing miscut angle, but also supports the conclusion of a very recent effective-medium-theory calculation by Frenken and Stoltze [78]. They predicted that due to a very short-range step-step attraction, many metallic vicinal surfaces should be faceted into low-index planes, but due to the entropic contribution of step vibrations (even at RT) to the surface free energy, the faceting of these surfaces is not usually observed. However, for TaC surfaces, the step meandering is

small (as can be observed from the straightness of the steps in Figs. 3.3(c) and (d)) due to very strong ionic bonding (as indicated by the extremely high melting point of 3983 °C). In addition, the orbital affinity responsible for this atomic-range attraction is strongly orientation-dependent, which is the general nature of ionic bonding. Because of these special properties, the entropic contribution to the free energy of TaC surfaces may be neglected; thus it is possible that the multi-height step facets can be stabilized by the atomic-range step-step attractions.

3.5.3 Long-range attraction

Next, we focus on the step-separation distribution for the steady-state images for the sample annealed at $T > 2000$ °C for 30 seconds (Figure 3.3(d)). We can see a landscape of alternating step bunches and relatively wide terraces with irregular size. The step-step separation ((100)-terrace width) within *these step bunches* is measured to be 13 atomic rows on average, where the atomic row spacing $a = 2.228$ Å. With the measured configuration of 12% single-, 56% double-, 31% triple-, and 1% quadruple-height steps, the *facet* formed by a step bunch has an average orientation close to (610), which is different from the overall orientation (910) of the surface. A line-cut profile from Figure 3.3(d) in the [010] direction is shown in Figure 3.4. From systematic measurements of the step separations along the [010] direction, the probability distribution $P(x)$ is plotted in Figure 5(b) (labeled as Tac910). This distribution has a highly skewed shape with a very sharp peak at $x_p \sim 13$ atomic rows

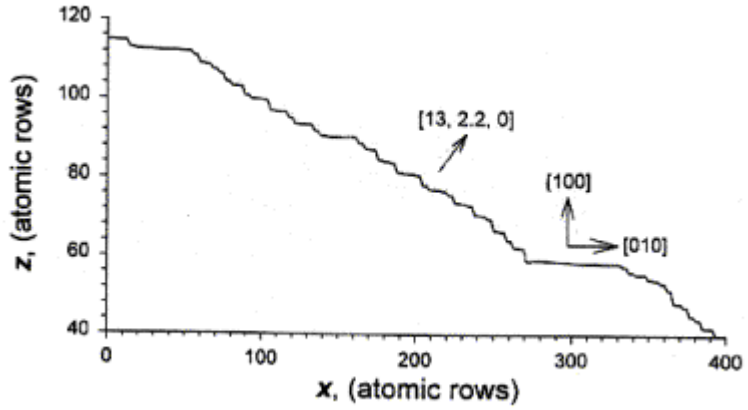

Figure 3.4 Cross-section profile of the step configuration. It was obtained from STM images shown in Figure 3.3(d).

and a mean step separation at x_m ~18.6 atomic rows. This is quite different from those reported for vicinal silicon surfaces [27,79] and even for the TaC(n10) surfaces (n = 1, 2, 3) [66,68-69], where the observed Gaussian-like step-step separation distributions result from a strong step-step repulsion varying as d^{-2}. The sharp peak position x_p represents the most probable step separation within the *step bunches*, and the mean step separation x_m is close to the mean (100) terrace width of 18 rows expected for dominant double-height steps with the (910) orientation. More interestingly, the rapid decay for $x < x_p$ and the approach to zero for $x < 5$ indicate the existence of a strong step-step repulsion in this range, so that the distribution of narrow terraces within step bunches is highly restricted. The slow decay for $x > x_p$ indicates a large variation in the width of the relatively wide (100) terraces between the (610) facets. The skewed shape of the distribution indicates that only a medium-range repulsive potential between the steps is unlikely to account for the observation, which is confirmed by our Monte Carlo simulations to be discussed below. A weak but longer-range attractive potential must be included. One can expect that, if we cut a vicinal surface with the (100) terrace much smaller than that of the (910) surface, the step-separation distribution will be determined predominantly by the repulsive step-step interaction, so that the distribution will be Gaussian when the repulsive interaction varies as d^{-2} [27]. This is exactly what has been previously observed on the TaC(310) surface [66,69]. The origin of the repulsive interaction is believed to come from the elastic dipolar effect because from a LEED *I-V* study [80], the

TaC(100) terrace is slightly buckled with the C atoms displaced outward (~ 0.2 Å) relative to the Ta atoms. This obvious surface strain may be relieved at steps, resulting in a force dipole at steps.

To see quantitatively how the competition between the *medium-range repulsion and long-range attraction* between the steps leads to such a skewed step-separation distribution, we have performed Monte Carlo simulations of 5the step thermodynamics. In the simulation, a one-dimensional (1D) array of 300 sites is initially given a uniform distribution. The system starts to approach equilibrium as the simulation time proceeds under the influence of a step-step interaction potential,

$$V(x) = \frac{A}{x^2} - \frac{B}{x^\alpha} \qquad (47)$$

in which A, B, and α are positive parameters. The first term represents medium-range repulsion, and the second term long-range attraction. The 1D approximation is justified by the observation of straight steps along [001] due to very high kink excitation energy. In order to reduce the fitting parameters, the first repulsive term in Eq. (47) is determined from the Gaussian distribution of step separations observed for the TaC(310) surface because in this case the step-step repulsion dominates. The fitting result is indicated in Figure 3.5(a), where T is the dimensionless temperature. T=0.005 gives the best parameters to be used in fitting TaC(910).

In Figure 3.5(b) we present the best simulation results for α=0.5, 1 and 1.5. In these three cases only B is the adjustable parameter. We also present the result for

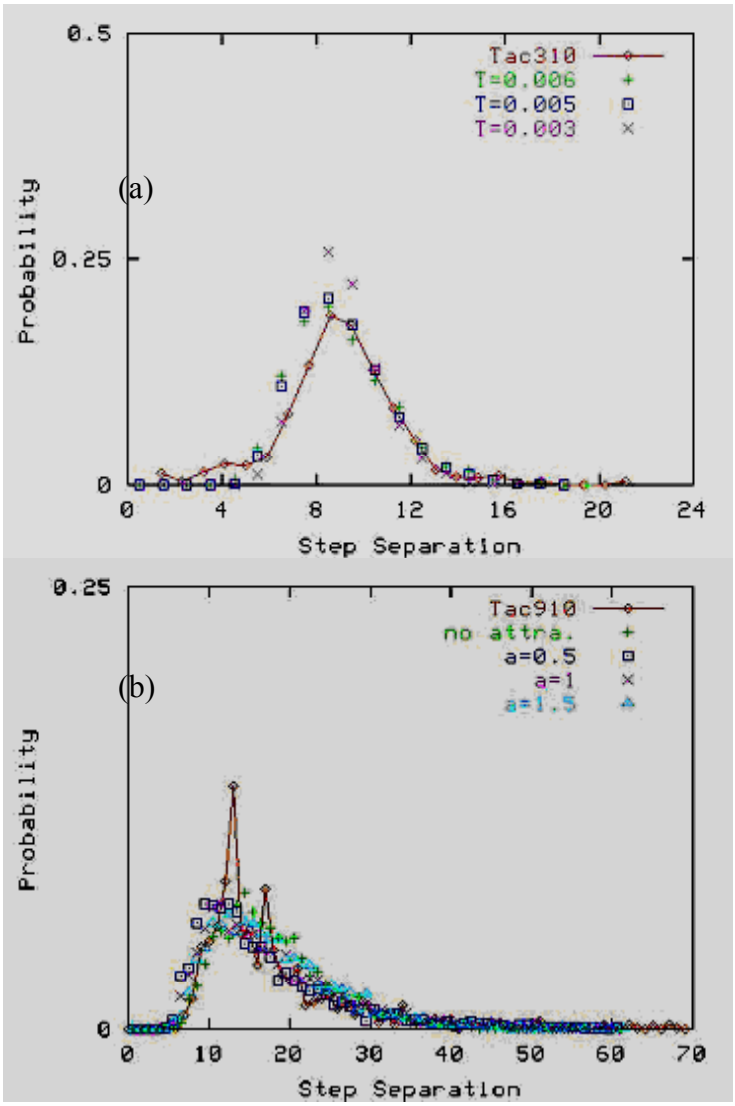

Figure 3.5 Step distributions from STM and Monte Carlo simulations. (a) Step distributions on TaC(310) from STM (as indicated by Tac310) and that from three Monte Carlo simulations at different temperatures. (b) Step distributions on TaC(910) from STM (as indicated by Tac910) and that from four Monte Carlo simulations with different power index α (1.5, 1, 0.5) and the case where no attraction is included.

B=0, which means no attraction. In this case, there is no free parameter. *Note that a repulsive term alone cannot produce the observed skewed distribution*. The skewed distribution obtained with no attraction in Figure 5(b) is because the value of A that gives the best fit for TaC(310) can not give the best for TaC(910). Using free parameters as that for Figure 5(a), the shape is Gaussian-like as well. To obtain the skewed shape of distribution found on TaC(910), it is necessary to include an attractive step-step interaction.

3.5.4 Summary

Using scanning tunneling microscopy, we have studied the step configuration on TaC(910), which is vicinal to the (100) plane, miscut 6.34º towards [010]. After annealing at ~ 2000 ºC, the surface is dominated by double-height steps which are bunched between relatively long intervening (100) terraces. The step-separation distribution is very skewed and sharply peaked at x_p ~ 13 atomic rows, which represents the most probable step separation within step bunches. Monte Carlo simulations show that besides the short-range repulsion, a long-range, attractive interaction must be included to interpret the measured distribution. Here we should also note on the limitation of our analysis. First, from the STM images, it is clear that there are complicated atomic movements at high temperature. This should be accompanied by the breaking of the chemical bonds. This fact casts doubt on the approach of using the concept of step-step interaction while ignoring the breaking and

rearrangement of the atomic rows. Second, here we have supposed that the short-range interaction and the long-range interaction act independently. It is very possible that the formation of multi-height steps and the skewed distribution of the step separations are intertwined. Thirdly, our experiment and previous study [28] indicate that the non-equilibrium nature of system can strongly influence the distribution of the step separations. All these would weaken the suitability of extracting the physical interaction by adopting rigid step-step simulations to fit the step separations.

Chapter 4 Dopant-Dopant Interactions underneath Surfaces

4.1 Introduction

The ability to incorporate reproducibly dopant atoms with precisely controlled concentrations and spatial distributions is essential in various technological applications of semiconductor materials. As the effort for device miniaturization continues to intensify, to achieve this goal is becoming increasingly difficult. In particular, the fabrication of nanometer-scale devices, the distributions of dopants underneath the surfaces may significantly influence the performance of these devices.

Dopant incorporation in submicrometer- and nanometer-scale systems is ultimately governed by the intrinsic interactions between the dopant atoms. The generally accepted view is that the charge of a dopant atom is screened by the charge carriers in a given semiconductor, which results in a repulsive screened Coulomb interaction between the dopants [12]. Such repulsion in turn leads to a rather homogeneous distribution of the dopant atoms in the semiconductor. In this chapter, we will show that cross-sectional scanning tunneling microscopy (XSTM) experiments actually indicate that negatively charged Zn dopant atoms in GaAs are inhomogeneously distributed and form clusters of dopant atoms. At first sight, the

clustering behavior seems to suggest the existence of a possible attractive interaction in addition to the screened Coulomb repulsion between the dopants. But our quantitative analysis of the dopant distributions by Monte Carlo simulations convincingly shows that the effective attraction actually results from strong many-body effects in the repulsive dopant-dopant interactions. We also illustrate the methodology to determine quantitatively the intrinsic screening length of point charges in the semiconductors based on XSTM images [82].

4.2 Experimental Results

Ebert et al investigated Zn-doped GaAs crystals with different carrier concentrations (n) ranging between 2.5 x10 ^{18} and 2.5 x 10 ^{20} cm $^{-3}$ [12]. The Zn dopant atoms were introduced into the crystals during growth ($n<10^{20}$ cm $^{-3}$) or by Zn diffusion at ~1180 K ($n>10^{20}$ cm^{-3}). The crystals were slowly cooled down to room temperature after growth with the exception of Zn-diffused crystals, which were quenched to room temperature. Thus the dopant atoms reached an equilibrium at a freeze-in temperature of GaAs or in the case of Zn-diffused material at ~1180K. Samples cut from the different crystals were cleaved in ultrahigh vacuum (5 x 10 $^{-9}$ Pa) and the isolated dopant atoms exposed on the (110) cleavage surfaces were imaged with atomic resolution by XSTM.

Figure 4.1(a) shows a typical STM image of such a cleaved surface of a GaAs

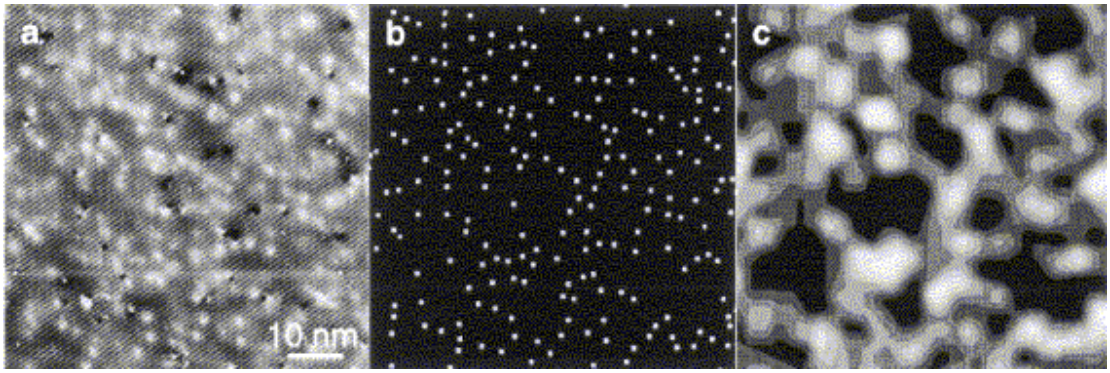

Figure 4.1. STM images of the clustering of dopant atoms. (a) STM image of a (110) cleavage surface of Zn-doped GaAs acquired at -2.4 V. A long-range contrast variation is superposed onto the atomic-scale corrugation of the atomic rows along the [1$\underline{1}$0] direction. The bright and dark contrast features are dopant atoms and vacancies, respectively. (b) Positions of the dopant atoms in (a). (c) Local concentration of the dopant atoms. A high concentration is shown as white contrast.

crystal doped with 2.5 x 10^{20} Zn cm^{-3}. The image shows the occupied density of states above the As atoms acquired at negative sample voltage [83]. The atomic-scale corrugation arising from the atomic rows along the [1$\underline{1}$0] direction can be recognized as rows from the upper right to the lower left corner. Localized bright contrast features arise from isolated dopant atoms [84]. The few localized dark contrasts are due to vacancies formed mostly after cleavage [85]. The localized contrast of the dopant atoms and vacancies arises from the imaging of the local screening potential around the isolated defects or dopants [86].

One of the most distinctive features in the STM images is the long-range contrast change (on the scale of about 5 to 10 nm) superposed on the localized features of the dopant atoms. The long-range contrast becomes more pronounced at lower magnitudes of the voltage, indicating that it is the signature of variations of the local band bending, namely, the position of the valence band edge changes locally relative to the Fermi level [85]. In order to unravel the origin of this effect, we deduced from Figure 4.1(a) the positions of all the dopant atoms based on their local contrast discussed in Ref. [84] [Figure 4.1(b)] and calculated the local concentrations [Figure 4.1(c)]. High concentration of dopant atoms is displayed as white areas; in contrast, the local concentration of dopants is a factor of 8 lower in the dark areas. Figure 4.1(c) demonstrates that the concentration of the dopant atoms varies by nearly 1 order of magnitude on the scale of about 10 nm and all the bright areas in Figure 4.1(c) correspond to the bright areas in Figure 4.1(a). Thus local fluctuations of the

dopant concentration on the scale of about 10 nm by nearly 1 order of magnitude cause fluctuations of the Fermi level on the same scale imaged as long-range contrast in Figure 4.1(a). Figure 4.1 also demonstrates that the dopant atoms tend to cluster. We have observed the clustering of dopants in all the samples investigated, including those grown by different methods, doped by diffusion and during crystal growth, and in different materials (GaAs and InP). Thus the observed effect is not simply due to sample preparation, but rather an intrinsic nature of the dopants.

As mentioned earlier, all the dopant atoms are negatively charged and should therefore mutually interact with the repulsive screened Coulomb potential. Nevertheless, the clustering behavior suggests the possible existence of a long-range attractive interaction between the dopants. In trying to identify the physical origin of the attraction, several candidates may come to mind, such as stress effects associated with the dopants [87], attractive forces caused by the oscillatory nature of the screening charge surrounding each dopant, or just a statistical distribution. In the following, we will show that, rather than any of those possibilities, the effective attraction is most simply accounted for by considering the many-body (or correlation) effects in the otherwise strictly repulsive screened Coulomb interaction. As described below, consideration of the correlation effects also naturally resolves another puzzle related to the apparent screening length of the repulsive potential in the semiconductor.

4.3 Extract Interaction through Pair Correlation Function

We proceed by first studying the effects of the short-range repulsion on the dopant distribution. The existence of the short-range repulsion is clearly indicated by the fact that although clustering occurs the probability of finding a very close pair of dopant atoms is negligible. In order to quantify the repulsive interaction we deduced from the XSTM images the positions of all the dopant atoms and calculated the distances r between all possible pairs of dopants [88-90]. This gives us the measured probability distribution of pair distances. Dividing the measured probability distribution of pair distances by the one for noninteraction, randomly distributed dopant atoms results in the pair correlation function *c(r)*, which is related to the mean force potential, *W (r)*, through [91]

$$W(r) = -kT \ln[c(r)] \qquad (1)$$

It should be noted that only if the extension of the interaction is smaller than the average separation of the dopants, correlation effects can be neglected and the mean force potential equals the interaction energy. On the other hand, the deviation of the mean force potential as derived from Eq.(1) away from the true interaction energy at low particle density limit should indicate the existence of correlation or many-body effect.

Figure 4.2(a) shows the values –ln[c(r)] for three carrier concentrations as a function of the distance *r*. First, we observed in all cases a repulsive interaction,

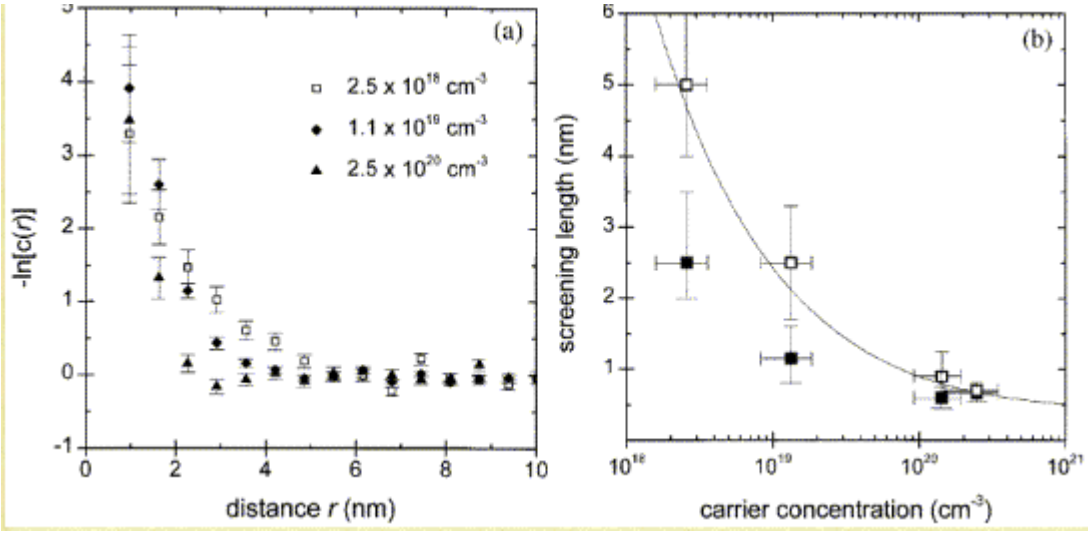

Figure 4.2. Pair correlation functions from STM and comparison of screening lengths. (a) Negative logarithm of the pair correlation function for three carrier concentrations and (b) values for screening lengths Rs determined in (a) as a function of the carrier concentration (filled squares). The solid line represents the theoretical screening length calculated according to Eq. (3). The open squares show the screening length corrected for many-body interactions.

whose extension increases from 2 to 5 nm if the carrier concentration decreases from 2.5 x 10^{20} to 2.5 x10^{18} cm^{-3}. This reflects the repulsive screened Coulomb interaction between two equal charges and the carrier concentration dependence of the screening. It is well known that the charge carriers screen charges of dopants in semiconductor, which leads to a screened Coulomb potential surrounding each dopant [82]

$$V(r) = \frac{e}{4\pi\varepsilon_0\varepsilon_r}\frac{1}{r}e^{-\frac{r}{Rs}} \qquad (2)$$

with Rs being the screening length

$$Rs = \sqrt{\frac{2\pi^2\varepsilon_0\varepsilon_r\hbar^3}{e^2(m_e)^{3/2}(2\pi kT)^{1/2}F_{-1/2}(\eta)}} \qquad (3)$$

$F_k\{h\}$ are the Fermi-Dirac integrals with the reduced Fermi energy $h=E_F/kT$. If we assume the low dopant density limit, we can fit the data shown in Figure 4.2(a) with a Yukawa potential and determine the screening length as a function of the carrier concentration [filled squares in Figure 4.2(b)]. As expected, the screening length increases with decreasing carrier concentration. However, the data do not agree quantitatively with the theoretical values for the screening length [solid line in Figure 4.2(b)] determined according to Eq. (3) for a freeze-in temperature of 900 K.

4.4 Many-Body Effect Discovered from Monte Carlo Simulations

The effective attraction between the dopants and the substantial discrepancy in the screening lengths described above both strongly suggest the importance of many-

body effects in the otherwise repulsive interaction between the dopants. As known previously, for a collection of mutually repelling particles, strong many-body effects can result in oscillatory features in the pair correlation function, with the minima indicating effective attractive interactions [88,91]. Furthermore, if the repulsion is a screened one such as that described by Eq. (2), many-body effects can also result in a shorter apparent screening length than the true one. To demonstrate that this is indeed the case for the present system, we have performed Monte Carlo simulations of the experiment. In the simulations, we positioned randomly 8000 dopant atoms surrounded by a screened Coulomb potential in a three-dimensional model crystal and allowed them to migrate to reach an equilibrium configuration. We took the boundary effects into account. In a real crystal the dopant atoms have to overcome some migration barrier in order to change their lattice position. It is rather difficult to implement this in our calculation, because the exact diffusion mechanism of Zn dopant atoms in GaAs is very complex. It is usually assumed that the dopant atoms diffuse in interstitial sites rather fast until they retake a substitutional lattice site by kicking out the Ga atom on that site [92]. This process occurs at elevated temperature and freezes in during the slow cooling process of the crystal growth procedure. From the data about Zn diffusion [92] we estimate the freeze-in temperature to be about 900 K. Because the electrostatic screened Coulomb potential affects the energy of a specific lattice site induced by neighboring dopants, we can assume that the effect of Coulomb interactions is felt by the dopants independent of the details of the migration

path. This consideration allows us to simulate the effect of the pair screened Coulomb interactions on the final spatial configuration of the dopant atoms without specifying the exact diffusion path. Specifically, we assume that the dopant interaction leads to an additional potential added to the trapping potential at a substitutional site. Therefore we allowed the dopant atoms to migrate with an energy equivalent to a temperature of about 50 K only within the screened Coulomb pair interaction potentials. In the real crystal this simulates the case where the diffusion occurs at freeze-in temperature plus 50 K. Simulations with different temperatures showed that within a reasonable temperature range the exact choice of the temperature does not change the results significantly.

After reaching the equilibrium configuration we analyzed the spatial distribution as we did for the XSTM images. We determined the (output) screening length from the simulated pair correlation function for different (input) screening lengths of the Yukawa potential. The results show that for very low dopant concentrations the input and output screening lengths are equal. At the experimental dopant concentrations the output screening lengths are considerably smaller than the input screening lengths due to many-body effects, i.e., interactions between more than two dopant atoms. Using these simulations we determined the intrinsic screening length in the GaAs crystals as a function of the carrier concentration by comparing the measured screening length with the output screening length of the simulation. The corresponding input screening length is the intrinsic one. The input screening lengths

[empty squares in Figure 4.2(b)] agree very well with the theoretical calculations according to Eq. (3) at 900 K (solid line). (The data obtained on Zn-diffused GaAs at 1180 K agree too, because at $n > 10^{20}$ cm $^{-3}$ the screening length is only very weakly dependent on the temperature.) The error bars of the corrected values arise from the error bars of the measurement and the error estimation of the simulation. We note that Figure 4.2(b) shows the first quantitative microscopic measurement of the screening length in semiconductors.

The good agreement in the screening length with consideration of many-body effects and that from the classical screening theory indicates that the present system can be well described by the classical screening. The importance of many-body effects is further corroborated by the simulated pair correlation function in Figure 4.3, which shows a clear attractive part beyond a short-range repulsive core. We note that an attractive part becomes most pronounced in the experimentally determined pair correlation function for the highest doped sample. The effective attractive interaction potential is the result of many-body effects [91] and leads to the clustering of dopant atoms observed experimentally. This conclusion is consistent with the observation that clustering of dopant atoms occurs independent of the semiconductor material, growth conditions, dopant element, and the technique of dopant incorporation. The model used is based only on the presence of charges in a material with a limited carrier concentration.

At this stage we discuss other possible sources of attractive dopant

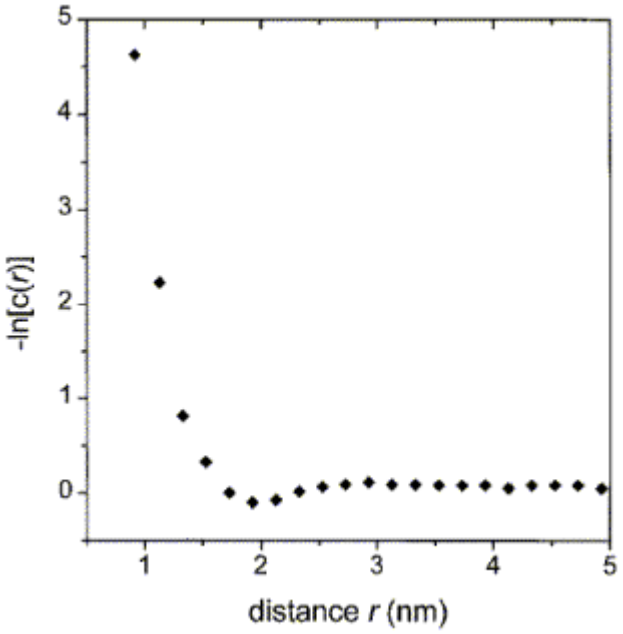

Figure 4.3. Pair correlation function from simulation, indicating many-body effect. Simulated negative logarithm of the pair correlation function with many-body interactions for a dopant concentration of 1.5 $x10^{20}$ cm^{-3}.

interactions. Stress-related forces induced by substitional Zn atoms can be excluded, because Zn atoms have nearly the same covalent radius as Ga atoms, which they substitute. Friedel oscillations can also be ruled out, because they should be too weak in strength at the elevated temperatures, and we found no indication of them in STM images. Van der Waals forces induced by fluctuations of the screening cloud can result in attractions, which are, however, also too weak compared to the direct Coulomb interactions. The simulations and the measured data also excluded statistical variations of dopant concentrations with no many-body interactions to be the origin of the clustering. Thus there are so far only many-body effects of the screened Coulomb interactions of dopant atoms, which are consistent with the experimental data.

In conclusion, we have used cross-sectional scanning tunneling microscopy to demonstrate that negatively charged Zn dopant atoms in GaAs are inhomogeneously distributed and form clusters of dopant atoms. The clustering behavior suggests the existence of a possible attractive interaction in addition to the screened Coulomb repulsion between the dopants. Our quantitative analysis of the dopant distributions by Monte Carlo simulations leads to the conclusion that the effective attraction actually results from strong many-body effects in the otherwise repulsive dopant-dopant interactions. Many-body effects are also shown to be important in extracting the intrinsic screening length of the Yukawa potential as a function of the carrier concentration in the system. Our study reveals a basic physical origin limiting the homogeneity of dopant atoms achievable in semiconductors.

Chapter 5 Kinetics of Extrinsic Defects: 2D Growth Mechanisms

5.1 Introduction

In this chapter, I present the studies of growth phenomena during the early stages of epitaxy. Unlike the studies presented in chapters 3 and 4, in epitaxial thin film growth, non-equilibrium kinetic processes play important roles, as many atomic diffusion processes required to achieve thermal equilibrium are significantly limited by the continuous deposition of new atoms on the surface [93]. However, thermodynamics provides the guidance on the *stability* of the thin films obtained. There are three classes of growth modes for thin film growth: Frank-van der Merwe (two-dimentional, 2D) growth, Volmer- Weber (three-dimensional, 3D) growth, and Stranski-Krastanov growth (2D followed by 3D). Under equilibrium conditions, the growth modes are determined by the specific surface free energy of the substrate (γ_s), that of the deposited material (γ_a) and the specific free energy of the interface (γ_i). If $\gamma_s > \gamma_a + \gamma_i$, adatoms prefer to form bondings with the substrate and the growth proceeds in smooth layer-by-layer mode (Franck-van der Merme growth); otherwise, adatoms prefer to form bonding among themselves and the growth proceeds in rough 3D growth. Stranski-Krastanov growth is the intermediate case, where the growth first

proceeds in the 2D mode, but beyond certain critical thickness the growth proceeds in the 3D mode [94-95].

In reality, realization of any of the above growth modes based on thermodynamic free energy arguments is through the various complicated kinetic processes taking place during the growth. And how to obtain an epitaxial growth morphology in the desired mode is usually a challenge. As demonstrated by examples presented in Chapter 1, a good control and understanding of the growth conditions is important in growing high quality surface structures. Especially, the high demand in improving 2D growth capabilities requires that people can have the flexibility in choosing the properties of adatom and substrate materials, so that the devices made can adapt to various physical environment. In the design of certain systems, the intrinsic properties of adatoms simply do not allow them to wet the substrate (for example, the interaction strength among adatoms themselves is stronger than that between adatoms and substrate atoms [94]). In this case, artificial effects such as strains or various defect structures are usually introduced to achieve the goal [93-94,25,96]. In molecular beam epitaxy (MBE), high growth temperature is utilized to achieve both a saturated adatom vapor and a high adatom surface diffusion so that the growth can proceed rapidly. How to avoid side effects such as intermixing becomes important and an intimate knowledge of the atomic diffusion mechanisms is critical in improving the product quality [93]. In this aspect, one important contribution is the microscopic observation that the size of the Schwoebel- Ehrlich barrier [97-98]

encountered by adatoms at the step edges can significantly determine whether the growth mode is 2D or 3D. If the barrier is small, adatoms can easily jump down at the steps before being trapped by arriving adatom, leading to the formation of layer-by-layer flat growth.

In the growth of thin films or nano devices from the vapor phase, single atom diffusion on the surface is the most fundamental process. It gives rise to nucleation of islands on substrate terraces or to step flow growth at elevated temperatures. Rigorously speaking, the adatoms navigate on an energetic landscape that has many local minima. In our below studies of surface diffusion presented below, we generally assume that a diffusion barrier can characterize the diffusion process. When atoms are in the local minima, they have enough time to establish thermal equilibrium with the substrate. Once they are thermally activated out of the local minima, they diffuse into other local minima.

The kinetics in semiconductor MBE [99-100,24] can be quite different from that of metallic systems [93]. This is due to the fundamental difference between the localized bonding nature for semiconductors and the delocalized electron nature on metal surfaces. Recently there has been significant progress in the understanding of electrons in determining the growth mechanism [101], which allows us to go beyond the classical atomic picture and explore the quantum origin of the different growth behaviors.

5.2 Mean-Field Nucleation Theory of Surface Diffusions

Let us suppose that during epitaxy, atoms from the vapor hit the solid substrate with a rate F (in monolayer per second, i.e. MLs^{-1}). These atoms make random diffusion on the surface until they meet other adatoms to create dimers and islands of larger sizes. For simplicity, let us assume that dimers are stable against splitting and immobile. As the deposition proceeds, the population of dimers increases about linearly with the time until their mean separations become comparable to the mean diffusion length of a single atom. Thereafter, the probability for a diffusing monomer to meet another monomer or a dimer becomes comparable and the growth of larger islands competes with the creation of more dimers. After the density of stable nuclei n_x (in number of islands per monolayer, x standing for any size that is stable) has increased sufficiently, any further deposition would exclusively lead to island growth, which means the saturation of the island density. Further deposition of atoms can cause coalescence of the existing islands to form larger ones.

Theoretical analysis of the above phenomena dated back to the work by Frenkel and many others [102,58]. Later Zinsmeister [103] used rate equations to describe the above growth process quantitatively. In the following, we take the simple case of 2D island growth, with the further assumption of no evaporation and no mobility or splitting of the dimers. A more general description can be found in the classic work of Venable [104]. The rate equations for the density of monomers and

stable islands can be written as

$$\frac{dn_1}{dt} = F - 2\sigma_1 D n_1^2 - \sigma_x D n_1 n_x - k_x F(Ft - n_1) - 2k_1 F n_1 \qquad (1)$$

$$\frac{dn_x}{dt} = \sigma_1 D n_1^2 + k_1 F n_1 - 2n_x(F - \frac{dn_1}{dt}) \qquad (2)$$

Here D represents the diffusion constant of the adatoms. σ_x and k_x represent respectively the capture area of diffusing atoms and impingement area of the atoms being deposited for an island of size x. The terms on the right-hand side of Eq.(1) denote, respectively, the increase of monomer density due to deposition with flux F, the decrease due to the creation of a dimer when two diffusing adatoms encounter, the decrease when a monomer is captured by a stable islands, and the decrease due to impingement on stable islands or monomers. In Eq. (2), the first two terms account for the increase of stable island density, n_x, due to the creation of dimers when two monomers meet by diffusion and direct impingement onto a monomer. The last term represents the coalescence of islands, which is neglected in the low coverage regime [95].

It is important to note that in the above we essentially have neglected the distinct characters of islands with different size (x) or configurations. The capture areas σ_1 and σ_x only reflect the local geometries statistically. Equation (1) and (2) only describe the general time evolution of the average values of n_1 and n_x. The capture areas can be evaluated from the following diffusion equation [105]

$$\frac{\partial N_1(\mathbf{r},t)}{\partial t} = D\nabla^2 N_1(\mathbf{r},t) + F\alpha - D\zeta^{-2} N_1(\mathbf{r},t) \qquad (3)$$

with

$$\alpha = 1 - \sum_{x=1}^{\infty} k_x n_x$$
$$\zeta^{-2} = 2\sigma_1 n_1 + \sum_{x=1}^{\infty} \sigma_x n_x + \frac{F}{D} k_1 \qquad (4)$$

Here the spatial variation of the monomer density $N_1(r,t)$ is related to n_1 by requiring that $N_1(r \to \infty, t) = n_1(t)$. r is the position of a monomer as measured away from the island under consideration. ξ is the average distance traveled by a monomer before being captured by an island or another monomer and α represents the fraction of the flux hitting the bare substrate. Usually we are interested in the saturated island density ($\frac{dn_1}{dt} = 0$) as it reflects the mean free path for monomer diffusion. Under this condition, the capture area σ_x can take the simple constant value of σ_1=3, σ_x=7, [104,106], which agree well with the above self-consistent calculation.

If we also neglect the effect of impingement (α=1), in the regime of complete condensation with negligible evaporation, the saturated island density can be obtained as [106-107],

$$n_x = \eta(\theta, i)\left(\frac{D}{F}\right)^{-\lambda} e^{E_i/(i+2)k_B T} \qquad (5)$$

θ is the saturation coverage, η is a dimensionless nucleation density and its calculation is given in [108,95]. The scaling factor λ is evaluated as

$$\lambda = \frac{i}{i+2} \qquad (6)$$

Here i denotes the critical island cluster size, defined by the condition that incorporating one more atom (i+1) would make the cluster stable. E_i is the critical cluster binding energy (E_1=0).

The temperature dependence of the saturated island density as given in Eq.(5) allows the extraction of information on surface diffusion, which is the underlying principle of using STM to detect diffusion mechanism.

The above nucleation theory can be applied to predict the relative importance of various processes involved in nucleation and the average island densities can be estimated reasonably accurate. However, the estimated distribution of island size is far from being realistic [109,105]. It also can not describe coalescence very accurately [93,110-111].

Studies of island growth in Ag/Pt(111) [93,111] and Cu/Ni(100) [112] suggested that the scaling laws of classical nucleation theory are valid only when nucleation takes place solely during deposition. When the ratio D/F is low, during the deposition adatoms would not have sufficient time to diffuse. After the completion of deposition, due to the existence of largely unsaturated bonding, there are still finite mobilities. However, their contributions to final island densities and size distributions are not determined by the competition between flux and monomer diffusion, but solely by the monomer distributions at the end of the deposition process [93].

5.3 Microscopic View of Nucleation Using FIM and STM

In this section, we give an introduction of the essential experimental apparatus that have been used to study surface diffusion and nucleation. However, I will limit my scope to FIM and STM. Other experimental designs such as utilizing field emission microscope [113], helilium-beam-atom scattering [114] or high-resolution low-energy electron diffraction [115] to carry out similar studies are not covered here.

5.3.1 Detection of the diffusion mechanisms using FIM [116]

In early 1950's, Müller [117] introduced the important apparatus Field Ion Microscopy (FIM). The use of FIM to view an individual atom has constantly provided us detailed information about atomic processes [118,116]. Some of these important contributions include the discoveries of the existence of step-edge barrier [97] and exchange diffusion [119-120].

In FIM, the image obtained is from protruding atoms of the tip itself. In such experiments, a high positive voltage (3-20kV) [116] is applied between the tip and the detector. In the chamber, there is a background imaging gas, which is usually He or Ne because of their chemical stability and easiness to be purified [116]. These imaging gas atoms are ionized at a few Å away from the surface and accelerated toward the detector where image spots are formed. The different levels of protrusion of the tip atom give rise to the non-uniform distribution of the electric field at the

surface, which is the origin of the imaging contrast in FIM [116].

In the cleaning procedure of FIM, it has a unique field evaporation process, which removes surface atoms as ions by a high electric field [118]. It occurs when the applied voltage to the tip is increased to a value beyond that required for field ion imaging. This process can generate well-defined substrate surfaces for precise study of atomic features [116]. The evaporation process from a (111)-oriented Ir tip is illustrated in Figure 5.1 [116].

In FIM, we can obtain the activation barrier of surface diffusion through the following equation,

$$E_d = k_B T \ln\left(\frac{l^2 \nu_0 t}{\langle r^2 \rangle}\right) \qquad (7)$$

Here ν_0 is commonly referred to as the attempt frequency, which is about 10^{12} s^{-1}. t is the observation time. l is the average distance during each jump, which is about the surface lattice constant. E_d and k_B are the diffusion barrier and Boltzman constant, respectively. $\langle r^2 \rangle$ is the mean-square distance as determined from the site-mapping procedure [116] used in FIM. T is the substrate temperature. The temperature range is limited by the onset of adatom motion in a reasonable observation period (lower limit) and the loss of adatom from the terrace because of its small size (upper limit). Usually it is possible to collect data at 4 to 8 temperatures over a range from 20 to 50 K [116]. The above equation can be derived from 2D random walk with Einstein equation.

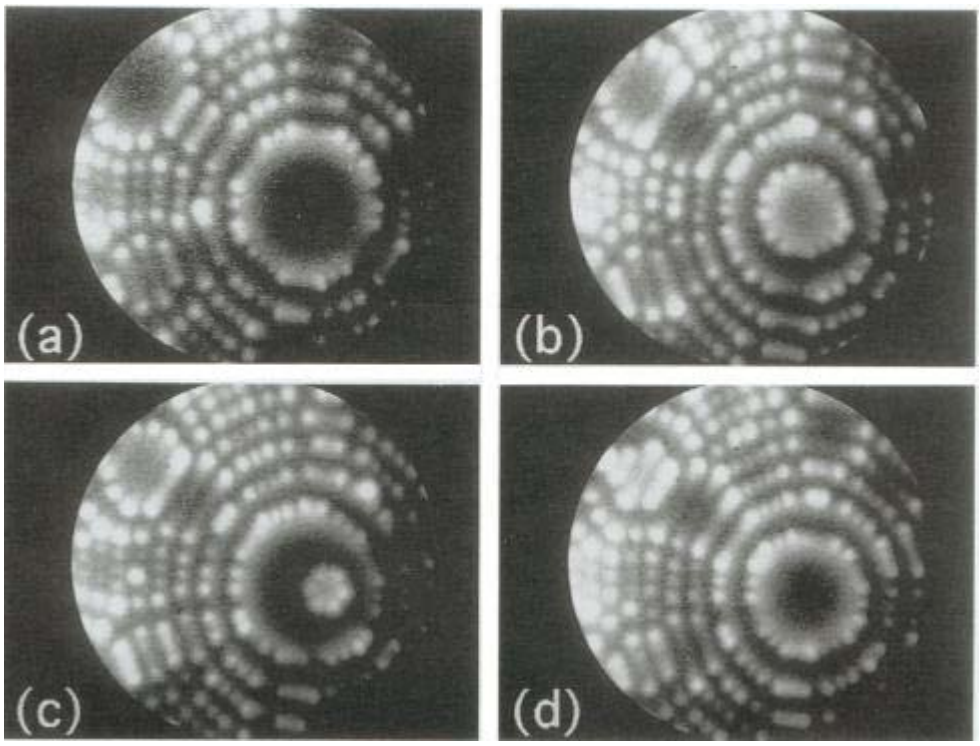

Figure 5.1. Determination of diffusion barrier from FIM. With the increase of electric field, atoms in the most protruding layer are torn off gradually. The circular planes in the images are (111) oriented. According to the experiment, the decrease in diameter of the (111) plane from (a) to (b) indicates that atoms are removed from the surface at 4.0kV. Further removal of atoms results in a heptemer indicated in (c). In (d) the evaporation reveals a new (111) surface. We can see from (c) that FIM can have atomic resolution [116].

Because of the high electric fields in the evaporation and imaging processes, FIM is limited to study adatoms which are stable under such high fields. For example, it is difficult to study adsorbates of non-metallic elements since these atoms are easy to be desorbed by the high imaging field [113]. The diameter of a typical plane on a field ion tip ranges from 25 to 100 Å, which may become comparable with the effective diffusion length of the surface atoms, therefore limiting the statistics, and placing an upper limit on the tip temperature.

5.3.2 Detecting microscopic information using STM

The extension of STM to variable substrate temperatures [121,1] provides an unprecedented microscopic view of activated atomic processes taking place on surfaces. By tuning the temperature, each process can be slowed down to the time scale that makes real-time observation possible. The working principle of STM for detecting diffusion mechanisms is mainly based on the observation of island densities at variable temperatures, as given by Eq.(5). From simple random walk analysis, the diffusion constant D can be written in the following form:

$$D = \frac{1}{2d} \nu_0 e^{-\frac{E_d}{k_B T}} \qquad (8)$$

where d is the dimensionality of the diffusion. For the simple case where dimers are stable and immobile islands on the terrace (i=1 in Eq.(6)), after substituting Eq.(8)

into Eq.(5), we can express the diffusion barrier according to the form:

$$E_d = k_B T \ln[\frac{\nu_0}{F}(\frac{n_2}{n})^3] \qquad (9)$$

In Figure 5.2, we reproduce the earlier STM images taken by Stroscio et al in identifying stable cluster sizes based on the observed island density distributions for the case of Fe/Fe(100) [122]. The growth temperatures in (a-c) are 20°C, 108°C and 163°C respectively. The plot in (d) shows that the island density follows an Arrhenius dependence with temperature until about 250°C. Above 250°C, the island density decreases more sharply, indicating the activation of other diffusion process(es). They obtained the adatom diffusion barrier by assuming that dimers are stable. Despite the relatively high temperature, this assumption was later verified to be valid [123]. The derived diffusion barrier is 0.45±0.08eV.

On close-packed surfaces, because the surface is flat and the activation energies, such as the dimer dissociation barrier, are generally small, it requires low substrate temperature to guarantee i=1. For heteroepitaxy of Ag on Pt(111), it was verified that dimers constitute stable nuclei up to 110K [124].

The above determination of the diffusion barriers of various processes relied on the dependence of saturated island density obtained at different *growth* temperature. There have been STM studies of adatom diffusion based on the onset of Ostwald ripening [124,111,125-127]. Initially the experiment starts from an island population predominantly consisting of dimers. Afterwards, the annealing

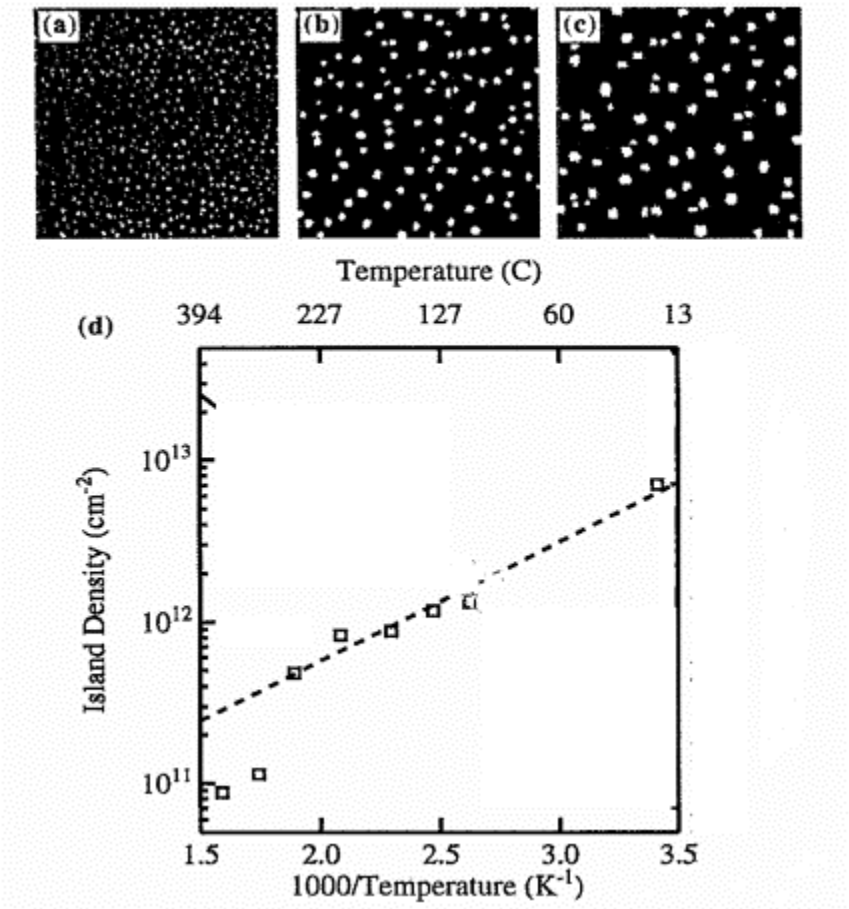

Figure 5.2 STM determination of diffusion barrier based on nucleation theory. Shown here are experiments on Fe/ Fe(100) [122].

temperature is increased gradually and the island density is monitored by STM during the annealing. One generally observes that the island size stays constant until reaching a well-defined temperature where it suddenly increases, indicating the onset of Ostwald ripening [93].

There are also STM studies of diffusion mechanisms without invoking nucleation theory. For example, Bott et al [128] deposited small amount of atoms on the terrace and measured the onset temperature of nucleation arising from the onset of diffusion. The diffusion barrier is derived by comparing the dependence of the island density on the temperature with that obtained from Kinetic Monte Carlo simulations.

It is essential to notice that in all the above STM-based measurements of the diffusion barriers, one central assumption is that a dimer is stable and immobile and the activation of dimer diffusion is well separated from that of monomer. There exists indications that whether dimer diffusion sets in before dissociation strongly depends on lattice geometry. On hexigonal lattices, the experiments for Ag/Pt(111) [124,129] suggest that dimers in this system dissociate before they could start to diffuse. On square lattices, ab initio calculations for Al/Al(100) [130,131] and FIM measurements for Pt/Pt(100)[132] and Pt/Rh(100) [133] all indicate that dimer diffusion via exchange may have an even lower activation barrier than monomer diffusion. From our EAM calculations (E_2 in Table 5.2), it is also clear that through a shear splitting process, dimers can diffuse with a barrier very close to that for monomer diffusion. On anisotropic substrates, the effect of dimer mobility may be more difficult to assess

because of the different diffusion barriers encountered along different directions.

5.4 Calculation of Diffusion Barriers

Purely from experiment, it is usually not possible to determine the microscopic mechanism of a diffusion process. This can be due to the limitation of experimental apparatus. For example, the high voltage requirement in FIM prevents the observation of Cu diffusion on Cu surfaces. It can also be due to the fact that the theoretical principles that these apparatus rely on are too rough for experiments to check some subtle problems, such as the asymmetric diffusion on fcc(111) surface. As we can notice from the above, nucleation theory generally neglects the local environments of the morphologies on the surface, which can be important in reality. In kinetic Monte Carlo simulations, it is also necessary to have inputs of diffusion barriers for certain processes, which may be difficult to obtain from the experiment. All these point to the importance of theoretical calculations of the microscopic diffusion processes. Because of the broken symmetry on surfaces, usually a large number of inequivalent particles are required to be included in the calculations, which puts serious limitations on the size of systems that can be treated in ab initio calculations. Some semi-empirical methods, such as the Embedded Atom Method (EAM)[16], are good compromises between ease of computation and incorporation of the essential physics. EAM method has received considerable attention from

researchers involved with classical atomic computer simulations. It has been applied to treat many surface problems such as diffusion [134-142], shapes of the adsorbed islands [143], reconstruction [144], surface phonons [145], and relaxations [146]. EAM has also been utilized to estimate inter-atomic forces in the simulations of adhesive and frictional interactions between an STM tip and a surface [147,148]. However, as to be noted below, EAM also has serious problems because of its deficiency in accuracy. In the following we also introduce some of the recent developments in first principles approach.

5.4.1 EAM calculation

In Chapter 2, we briefly described the principles of EAM calculation. In this section, we will present some more details on how to set up an EAM calculation.

As explained in Chapter 2, the embedding energy is given in the following formula:

$$E_{tot} = \sum_i F_i(\rho_{h,i}) + \frac{1}{2}\sum_i \sum_{j(\neq i)} \phi_{ij}(R_{ij}) \qquad (10)$$

Here, $\rho_{h,i}$ is the host electron density at atom i due to the remaining atoms of the system, $F_i(r)$ is the energy to embed atom i into the background electron density ρ, and $\phi_{i,j}(R_{ij})$ is the core-core pair repulsion between atoms i and j separated by distance R_{ij}. (Note that F_i only depends on the elements of atoms i and j.) The electron density is approximated by the superposition of the atomic densities:

$$\rho_{h,i} = \sum_{j(\neq i)} \rho_j^a(R_{ij}) \qquad (11)$$

Here ρ_j^a is the electron density contributed by atom j.

In the original development of EAM, the atomic densities were taken from Hartree-Fock calculations of free atoms [16]. However, using this configuration of free atoms to present the electron density in the solid may not be suitable. Considering the easy accessibility of bulk electron densities from LAPW calculations nowadays, it becomes possible to combine these bulk electron densities with free atom configurations to approximate the interested system.

Approximate values of the embedding functions and pair interactions (Eq.(10) of Chapter 2) are usually determined by fitting the known bulk properties such as the sublimation energy, lattice constant, elastic constants, etc [16,149]. In cases where the empirical data are unavailable, it is possible to use first-principles calculations to determine these functions [150].

Under the assumption that the atomic electron densities ρ_j^a (R) and the pair interaction F (R) are known, the embedding energy can be uniquely defined by requiring the total energy of the homogeneous fcc solid, computed using Eq. (10) to agree with the following universal equation of state [16],

$$E(a) = -E_{sub}(1 + a^*)e^{-a^*} \qquad (12)$$

in which E_{sub} is the absolute value of the sublimation energy at zero temperature and zero pressure. The quantity a* is a measure of the deviation from the equilibrium

lattice constant

$$a^* = a\left(\frac{a}{a_0} - 1\right)\left(\frac{9B\Omega}{E_{sub}}\right)^{1/2} \qquad (13)$$

Here, B is the bulk modulus of the material, a is a length scale characteristic of the condensed phase such as the fccc lattice constant, a_0 is the equilibrium lattice constant, and W is the equilibrium volume per atom.

The pair interaction between atoms of types A and B is determined from their electrostatic origin:

$$\Phi_{AB}(R) = Z_A(R)Z_B(R)/R \qquad (14)$$

where the effective charges Z(R) is obtained by fitting to the bulk properties [16]. Shown in Figure 5.3 are fitted functions for the effective charges and embedding functions for Cu, Ag, Au, Ni, Pd, and Pt [16].

5.4.2 First-principle calculation of diffusion barriers

Since the jellium calculation of surface electronic properties by Lang and Kohn [151], there has been a great deal of progress in reducing the computational cost while improving accuracy [152]. However, for systems with low or no symmetries, such as adatoms, islands, kinks or steps on surfaces, first-principles calculations are still computationally costly. Quantitative studies of phase transitions on surfaces are even more demanding. In the following, we present several novel approaches used in first-principles calculations of diffusion barriers. The brief review

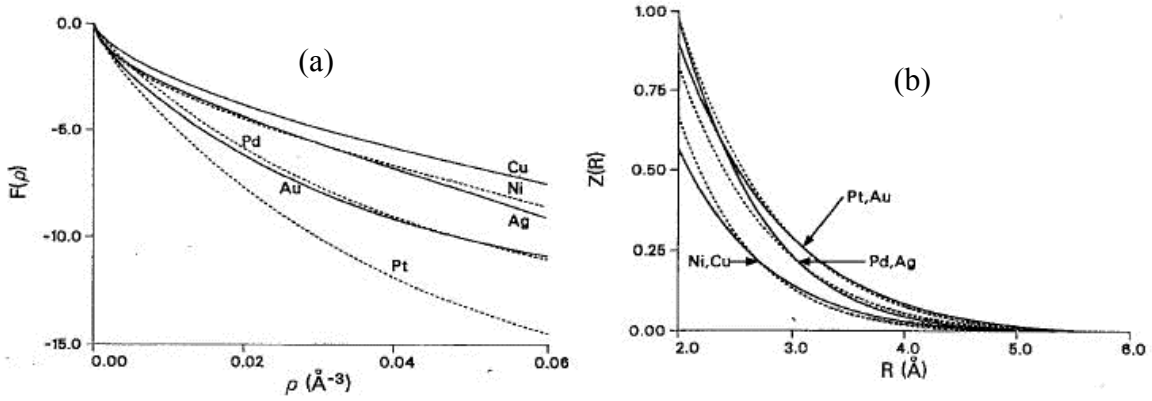

Figure 5.3 Embedding functions and effective charges used in EAM. From [16].

is not intended to be complete.

Feibelman et al introduced the scattering-theory approach [153-154,130-131,155] to the local-density functional energy minimization problem. Within this approach, it is possible to treat the low-symmetry problem of an isolated impurity or defect on an otherwise perfect metal crystal surface via a self-consistent determination of the one-electron Green's function. In the calculation, the problem of a point defect (e.g. the adatom) in a perfect crystalline host is broken into two simpler self-consistentency problems. The first is a linear-combination-of-atomic-orbitals (LCAO) pseudopotential calculation of the Bloch waves of the host. In their study of Pt/Pt (111) [155], the Pt (111) surface was modeled as a slab and the localized orbitals (contracted Gaussians) were selected by requiring that they yield an excellent fit to the well-converged linearized augmented plane wave (LAPW) energy band dispersions for the same slab geometry. However, the selection of the basis is still based on experience instead of a standard process. The scattering of these Bloch waves by the point defect is evaluated in the same orbital basis.

With the novel construction of the surface slab, Stumpf and Scheffler and coworkers [156-160] used standard ab initio calculations to study the adsorption and diffusion of adatoms on different surfaces.

Especially, in their study of adatom diffusion along steps, they used grooved structures with the outmost layer partially occupied [156]. The step structures on

fcc(111) surfaces were realized by choosing suitable vicinal surface of (m,m,m-2) and of (m+2,m,m) orientation. The (m,m,m-2) surface consists of (111) orientation that are m atomic rows wide and separated by {111} faceted steps. The (m+2,m.m) surface has (111) terraces that have m+1 atomic rows in width, which are separated by {100}-faceted steps [161]. These properties are illustrated by vector decompositions:

$$(m, m, m-2) = (m-1)\times(111) + 1\times(11\bar{1})$$
$$(m+2, m, m) = m\times(111) + 2\times(100)$$

After removing the common factor, Miller indices are (m/2,m/2,m/2-1) and (m/2+1,m/2,m/2). Through the above constructions, they studied the difference between {111}- and the {100}-faceted steps as shown in Figure 5.4. On Al(111), they set up isotriangular Al islands purely bounded by {111}- and the {100}-faceted steps. These islands are related to each other by 60° rotation on the terrace. Due to the finite size of islands, it is necessary to exclude the energy difference between edges and corners, which was disentangled by using islands of different sizes. Their calculations showed that the {111}-faceted step (or B step in Figure 5.4) is favored by 0.025eV per corner and 0.017eV per step atom over the {100}-faceted step (A step in Figure 5.4). Diffusion along A step is via normal hopping with a barrier of 0.32eV, while along B step, the exchange mechanism is preferred, with a barrier of 0.42 eV.

Using the scattering theory as introduced above, Feibelman et al [162-163] used the (331) surface to approximate these steps and obtained similar results. These

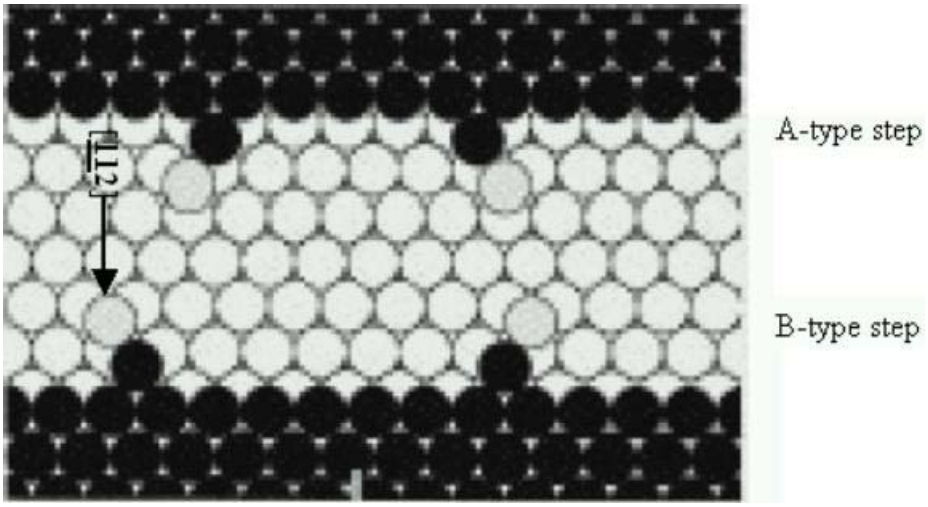

Figure 5.4 Ball model of A-type and B-type steps on fcc(111) surfaces. From [164].

subtle energy differences are important in understanding the orientations of dentrites on fcc(111) surfaces.

As a summary of our introductions of the various tools used to study surface diffusion mechanisms, in Table 5.1 we present some examples of single atom diffusion barriers obtained from these approaches [93].

5.5 Simulation of Island Growth at Surfaces

Purely from experiment, it is usually difficult to assess the importance of certain diffusion process in determining the island morphologies. This is because diffusion on a surface is usually very complicated and there are many conditions to control. In determining the importance of certain diffusion channel, one usual method is the tuning of the growth temperature. However, the flexibility provided by tuning the temperature is very small. For example, on fcc(100) surfaces, the dimer splitting barrier is very close to that of adatom diffusion on the terrace. It would be very difficult to distinguish their roles by tuning the temperature. In simulations, however, we can increase or decrease the diffusion barriers of certain processes and to assess their roles. This recognition of the special roles of Kinetic Monte Carlo simulations has been widely accepted in the community of film growth [15]. We have introduced the principles of this method in Chapter 2. Here we outline the procedures on how to specifically carry out KMC simulations

Table 5.1 Energy barriers for adatom diffusion on isotropic metal surfaces. (simplified from [93] and with minor changes)

System	Experiment (eV)	Exp.Technique	Theory (eV)	Type of calculation
Fe/Fe(100)	0:45 [122]	STM		
Cu/Cu(100)	0.40 [114]	He-Scat.	0.51 [134]	EAM
Ag/Ag(100)	0.33 [165]	STM	0.48 [134] 0.50 [166]	EAM FP-LMTO
Cu/Ni(100)	0.36 [112]	STM	0.47 [112]	EMT
Ag/Pt(111)	0.168 [129]	STM	0.20 [167] 0.15[168]	FP-LDA DFT-LDA
Pt/Pt(111)	0.26 0.25	STM FIM	0.39 [169] 0.38 [155]	ab initio DFT ab initio scattering
Ag/Ag(111)	0.097	STM	0.14/0.10 [169]	DFT-LDA/GGA
Ag/Ag/Pt(111)	0.060	STM	0.060 [168]	DFT-LDA

Consider the motion of adatoms on a crystal surface. This is often simulated with a discrete lattice model. In typical simulations of crystal growth, the interactions among atoms and between atoms and the substrate are simplified with the introduction of diffusion barriers the atoms have to overcome when attempting to move. In some cases, it may be necessary to use some empirical or the real interaction potential. Usually the atoms are only allowed to hop from their original sites to vacant, nearest-neighbor sites. The lattice-coordination number z is dictated by the symmetry of the crystal surface. During the simulation, each time one atom on the surface is selected randomly, and one of the z nearest-neighbor sites is randomly chosen to be the destination. If the chosen nearest-neighbor site is occupied, the procedure restarts. If it is vacant, the probability $w_e^{(i)}$ is computed according to Eq. (6) of Chapter 2 and compared with a random number r ($0 \leq r \leq 1$). In simulations where realistic interactions are built into the energy difference between different configurations, the calculation of the energies would be the bottleneck in improving the speed of the simulation. The atom hops to the new position if $w_e^{(i)} \geq r$; otherwise, it remains at its original site. During the simulation, it is also possible to select many atoms [14,125] because the real physical process is parallel, which implies that every atom on the lattice tries its own fortune at every moment individually. If there are long range forces that do not decay in the vicinity of the chosen atom, it may be necessary to allow all the atoms in the range of the force to try their chances simultaneously. In this case we may need to introduce a normalized temperature to

reflect the difference in the degrees of freedom. By considering many particles and determining their fates collectively, this method allows the existence of local frustration and better chance to overcome local minima. To simulate the *growth* process, it is also necessary to specify how many steps the atoms on surface can make before the arrival of another atom.

As pointed out in Chapter 2, it is important to note the difference when calculating the hopping probability between traditional Monte Carlo and Kinetic Monte Carlo simulations.

5.6 Fractal (Dentrite) Surface Morphologies

In nature, people have found that morphologies of different orders of spatial scales may have the same mathematical or scaling properties. From snowflakes, icicles hanging out of the window in cold weather, the shape of coastline, to the branches of Amazon River, all of them share the so-called self-similarity and hierarchic organization [93]. The correlation functions describing their morphologies have a scale-invariant (power law) form. The power appearing in these laws is a fractal number [93].

In studies of epitaxial growth, islands with fractal morphologies have also been observed at low growth temperatures. By changing the growth conditions such as the substrate temperature, these morphologies can undergo shape transitions.

Usually at high temperatures, islands obtained are compact.

The diffusion limited aggregation (DLA) model [170-172] was proposed long ago to explain fractal morphologies observed on crystal surfaces. In this model, it is assumed that whenever two atoms meet together, they can not diffuse or split any more. Other adatoms can diffuse randomly on the terrace and attach themselves to these immobile dimers or larger clusters following the hit-and-stick scheme. The classical DLA model always produces ramified fractal islands in which there is no preference of orientation. In reality there are many fractal systems having preferred directions. It has been found that anisotropy dominates the transition from ramified to dendrite patterns [93]. Dendritic growth with triangular geometry is commonly observed for low temperature aggregation with moderate deposition flux on hexagonal close-packed surfaces. Such patterns have the common feature that their branches are preferentially grown in three directions which are rotated 120º with respect to each other. In Figure 5.5 we show several dendrite islands observed on hexagonal surfaces. Asymmetric initial branching mechanisms have been explored to understand their origin [173,164].

5.7 Importance of Island Corner Barrier in 2D Growth

5.7.1 Introduction

As we have mentioned earlier, in three-dimensional growth, it is well

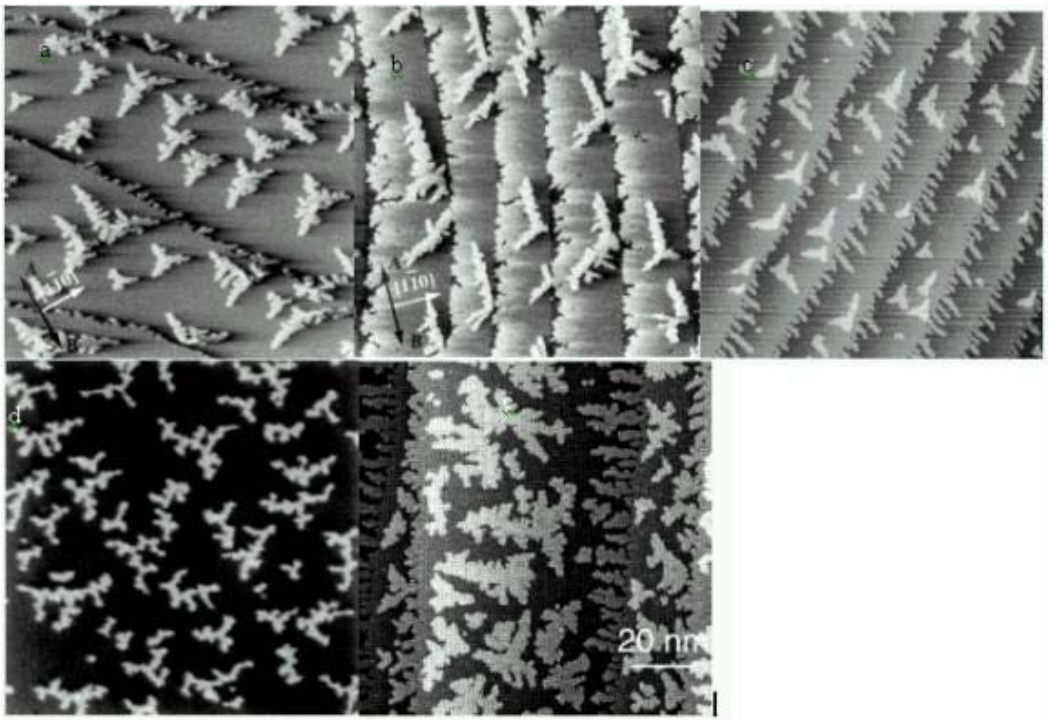

Figure 5.5 Dentrite islands observed on hexagonal surfaces. In this figure, the dendrites were observed on (a) Ag/Ag (111)[173,93]; (b) Ag/1MLAg/Pt (111) [173,93]; (c) Au/Pd (111)[174]; (d) Pt/Pt (111)[164] (e) Pt/Ru (0001)[175].

established that a weak Schowebal- Ehrlich barrier effect [97-98,176] can lead to the layer-by-layer growth mode. In 2D growth, a corresponding island corner barrier effect has been proposed to play the similar role in controlling the compactness of two-dimensional islands [177]. Atomic processes at island corners were considered in understanding the observation that it is easy to grow fractal islands on fcc (111) surfaces but difficult on fcc (100) surfaces [178]. Consideration of such processes has also been invoked to provide the initial asymmetric branching mechanism for formation of dendrite islands on hexagonal surfaces [173,164]. However a clear recognition of the importance of island corner barriers in controlling the compactness of 2-D islands growth was not proposed until recently [177].

The traditional belief was that a small edge diffusion barrier compared to that for terrace diffusion would be sufficient to obtain compact islands. This is partly correlated with the fact in both homoepitaxial and heteroepitaxial metal-on-metal growth, islands formed on substrates of triangular or hexagonal geometry are often noncompact if the growth temperature is sufficiently low, and become compact at higher temperatures [179,173,164,180-184]. For these surfaces, edge diffusion is typically slower than terrace diffusion. In contrast, islands formed on substrates of square geometry are mostly compact [122,185,125-127]; and for these systems, edge diffusion is typically faster than terrace diffusion. The few exceptional cases of Cu/Ni (100) [186] and Ag/Ni (100)[187] are due to strain energy and formation of a triangular lattice, respectively. This conventional view was not questioned until the

attempt to explain the triangular envelope of dendrite islands grown on hexagonal surfaces [173,164], where the importance of an independent corner diffusion process was considered. Recently, the role of edge diffusion is better recognized as the controlling factor for the broadening of the branch thickness in both analytic models [178,188-189] and KMC [190]. The basic idea underlying these studies is that the lateral impingement rate competes with the rate for an atom to diffuse along the edge of a compact seed island. The seed island stays compact until the edges reach a critical width (w) for which both rates become comparable. At that point nucleation of protrusions at the edge can no longer be flattened out and the aggregates become unstable against ramification through the Mullins-Sekerka instability [191]. This instability argument defines the critical size for ramification as well as the mean branch width of the clusters after ramification. Although this stability criterion can yield reasonable estimates for certain systems [190,189]), the drawback is that it neglects significant microscopic processes occurring at the island edges. For example, corner diffusion may require a higher activation energy than edge diffusion, and atoms can be trapped at the edges irrespective of how fast the edge diffusion is.

5.7.2 Important time scales involved in rate equation analysis [13]

Two time scales are important in the rate equation analysis. One is the average time separation, t_a, for two consecutive adatoms on the terrace to arrive at a given island edge. The other is the average time, t_r, for an adatom to reside at the edge

before it escapes via island-corner crossing. It is natural to expect that $t_r >> t_a$ would lead to noncompact or fractal-like islands whereas $t_r << t_a$ would ensure compactness. The center of the crossover region is defined by $R=t_r/t_a \sim 1$.Here we are interested in the temperature ranges where direct adatom detachment from an island edge is negligible. Also we focus our attention on isotropic systems. On anisotropic surfaces, it is possible that detachment can set in easier than corner diffusion [192].

The average residence time t_r can be approximated by the sum of the average time, t_e, spent by an atom at the edge before it reaches the corner, and the average time, t_c for the atom at the corner site to cross around. Let Na denote the length of the island edge, where a is the surface lattice constant of the substrate, and N the number of sites along the given edge. Adatoms randomly arrive at the island edges from the terrace and then diffuse along the edges to the island corners. It can be shown that

$$t_e = \frac{N^2 a^2}{6D_e}$$
$$D_e = a^2 \nu_e e^{-\frac{E_e}{k_B T}} \qquad (15)$$

Here D_e is the edge diffusion coefficient. ν_e the attempt frequency for an atom to hop along the edge. The average time t_c is the product of the inverse of the probability for an adatom to be at either of the two corner sites and the time for the adatom to cross the corner,

$$t_c = \frac{N}{\nu_c} e^{\frac{E_c}{k_B T}} \qquad (16)$$

where ν_c is the attempt frequency for an atom to cross the corner. We then have for the average residence time

$$t_\gamma = \frac{N}{\nu_c} e^{\frac{V_c}{k_B T}} + \frac{N^2}{6\nu_e} e^{\frac{V_e}{k_B T}} \qquad (17)$$

The successive arrival time t_a is given by

$$t_a \sim \frac{n}{F} \qquad (18)$$

Here n is the island density and F is the deposition flux. We suppose that the distribution of monomer on the terrace in a state of dynamic equilibrium so that the net increase of monomers by deposition is transferred to the incorporation with the existing islands. n is given by [104,193,194]

$$n = \left(\frac{3\theta^2}{\nu_t F^2 a^2}\right)^{\frac{1}{3}} e^{\frac{V_t}{3k_B T}} \qquad (19)$$

where θ is the coverage, and ν_t is the attempt frequency for an atom to hop on the terrace. Using $\theta^2 \sim nN^2$ we have for the criterion

$$\begin{aligned} R &= Rc + \mathrm{Re} \\ &= \gamma\left(\frac{\nu_t F a^2}{3\nu_c^2}\right)^{\frac{1}{2}} e^{\frac{2V_c - V_t}{2k_B T}} + \frac{\gamma}{6}\left(\frac{\nu_t^2 F (2a)^4}{9\nu_e^3}\right)^{\frac{1}{3}} e^{\frac{3V_e - V_t}{3k_B T}} \end{aligned} \qquad (20)$$

where the first term R_c and the second term R_e correspond to the contributions of corner crossing and edge diffusion, respectively, and $\gamma \sim 1$ is a parameter that weakly depends on the island geometry. It is clear from Eq. (20) that large values of V_c and V_e are likely to result in $R \gg 1$ at low temperatures, leading to fractal growth. More

importantly, it should be emphasized that, even at temperatures where $R_e<<1$ (corresponding to high edge diffusion), the existence of the island corner barrier V_c can still lead to $R\sim R_c>>1$ and the formation of noncompact islands. Only when both $R_c<<1$ and $R_e<<1$ can the system reach the compact-growth regime. Therefore, the island-corner crossing is the rate-limiting process dividing the noncompact and compact growth regimes.

5.7.3 Kinetic Monte Carlo simulations

5.7.3.1 Model

Here we study the effect of island corner barrier on two-dimension square lattice [134,13] by Kinetic Monte Carlo simulations. The three most important atomic rate processes controlling island compactness are schematically shown in Figure 5.6 for growth on fcc (100) surfaces. The first is the site-to-site hopping of an isolated adatom on a flat terrace, with an activation barrier V_t. The second is diffusion along island edges, with the barrier V_e. The third is corner crossing, with the barrier V_c. In general, we have $V_c > V_e$, because an adatom has to lower its coordination in crossing an island corner, in a manner similar to atom climbing down from an upper layer to a lower layer [97-98].

5.7.3.2 Change of morphologies due to variation of corner crossing barrier

A direct demonstration of the importance of island corner barrier effect would

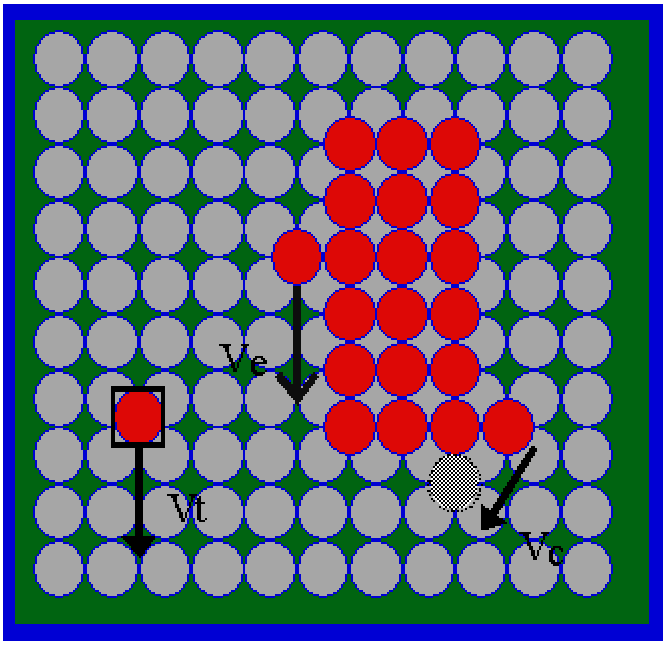

Figure 5.6 Illustration of terrace, edge and corner diffusions. Here we take a fcc (100) surface as an example. The gray circles refers to the substrate, while the red ones represent adatoms. Arrows indicate the potential diffusion directions of the atom(s). Terrace diffusion: Vt; edge diffusion: Ve; island-corner crossing: Vc

be the observation of the change of island morphologies with the change of the corner barrier height while keeping all other growth parameters the same. We demonstrate this by a set of such simulations. The results are demonstrated in Figure 5.7 (a-k). In these simulations, except the corner barrier, all other parameters are the same: size of the substrate 300x300, coverage θ=0.11ML, flux rate F= 41 MLs^{-1}, T=300K, V_t=0.15eV, V_e=0.20eV. The corner barrier height varies from 0.15eV in (a) to 0.65eV in (k). In these simulations, we have also recorded the numbers of events for both edge diffusion and corner crossing. These numbers are plotted in Figure 5.7(l). It is obvious that frequent edge diffusion does not necessarily lead to compact islands. Only when corner diffusion becomes appreciable can the islands become compact. These non-compact islands are directional. The arms are extended along the directions of terrace diffusion. The branches of the arms are so few that these islands have no self-similarity. To certain extent, they are the corresponding dendritic islands we find on square lattices while on hexagonal islands they resemble a triangular shape as illustrated in Figure 5.5.

5.7.3.3 Change of island morphologies due to variation of the growth temperature

In real experiments, it is impossible to adjust the corner barrier height as easily as above. For a given system, the corner barrier is fixed by the properties of the system. For some system it is possible that these barriers are so favorably arranged that we can adjust the growth temperature to observe their effects one by one. We

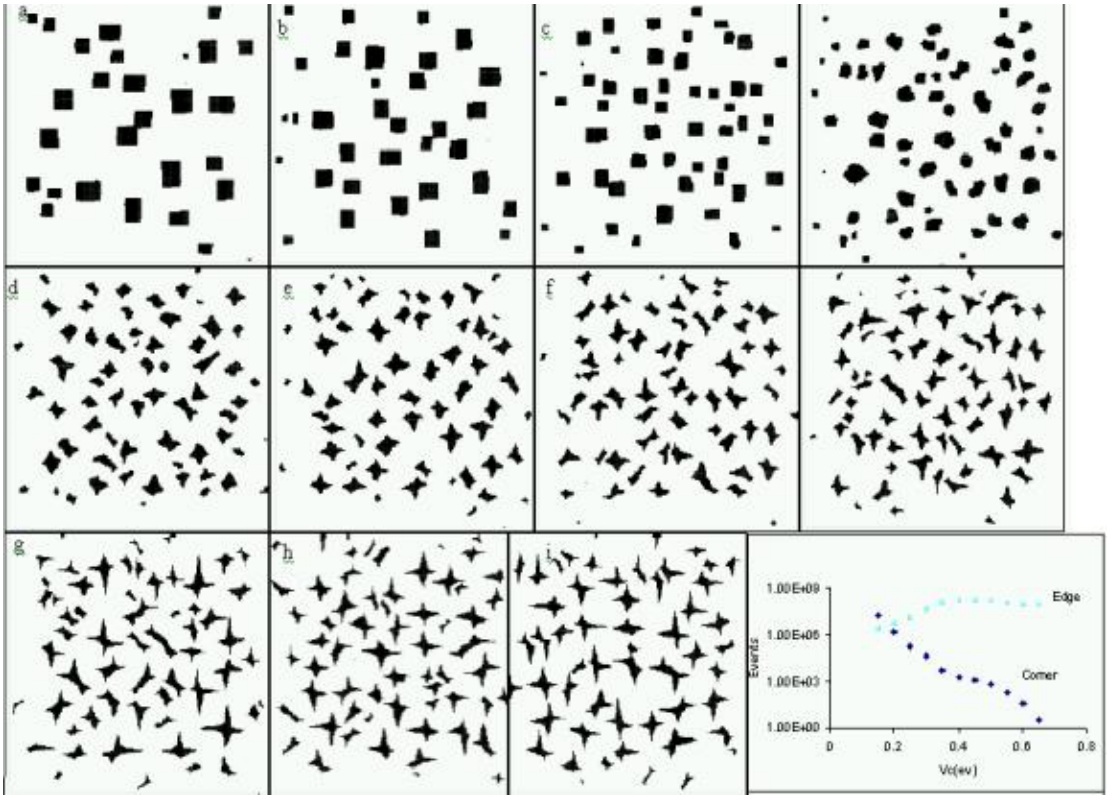

Figure 5.7 Variation of morphologies with corner barriers

define such a set of diffusion barriers to study the shape transitions induced by temperature change. Here V_t=0.15eV, and V_e=0.215eV. The size of the substrate is 300x300, and θ = 0.11 ML. The corner barrier V_c is 0.32eV in Figure 5.8 from (a) to (e). The growth temperature increases from 50K in (a) to 500K in (e). Since in this series, both edge diffusion and corner diffusion are varied, we add (f) obtained with the condition that V_c=0.8eV while all other parameters are the same as that in (e).

The flux rate is chosen such that between the deposition of two consecutive adatoms, at different growth temperatures, each atom on the terrace always has a chance to be chosen to jump 1000 times. This corresponds to F= $1.3\text{x}10^{-12}$, $4\text{x}10^{-4}$, 0.28, 41, and 410 ML/s for T=50, 100, 200, 300 and 500K, respectively. By this way, we ensure to have comparable island densities at different growth temperatures. As to be pointed out later, a change in the flux rate does not change the island morphologies critically once the islands are large enough. We have the numbers of edge diffusion and corner crossing events given by (I_e,I_c)=$(1.6\text{x}10^3,0)$, $(5.0\text{x}10^5,1)$, $(2.8\text{x}10^7, 2.0\text{x}10^3)$, $(4.2\text{x}10^7, 2.2\text{x}10^4)$, $(2.6\text{x}10^7,1.7\text{x}10^5)$, and $(2.2\text{x}10^8, 290)$ from Figure 5.8(a) to Figure 5.8(f) respectively. At 50K (Figure 5.8(a)), each island has many randomly extended arms without resemblance of the symmetry of the substrate. In this case, although both edge and corner diffusion events are effectively frozen, our simulations indicate that if edge diffusion is slow, corner barrier does not influence the island morphologies. So the islands in Figure 5.8 (a) are the traditional ramified fractals caused by slow edge diffusion [170-172]. We should note on the almost unrealistic

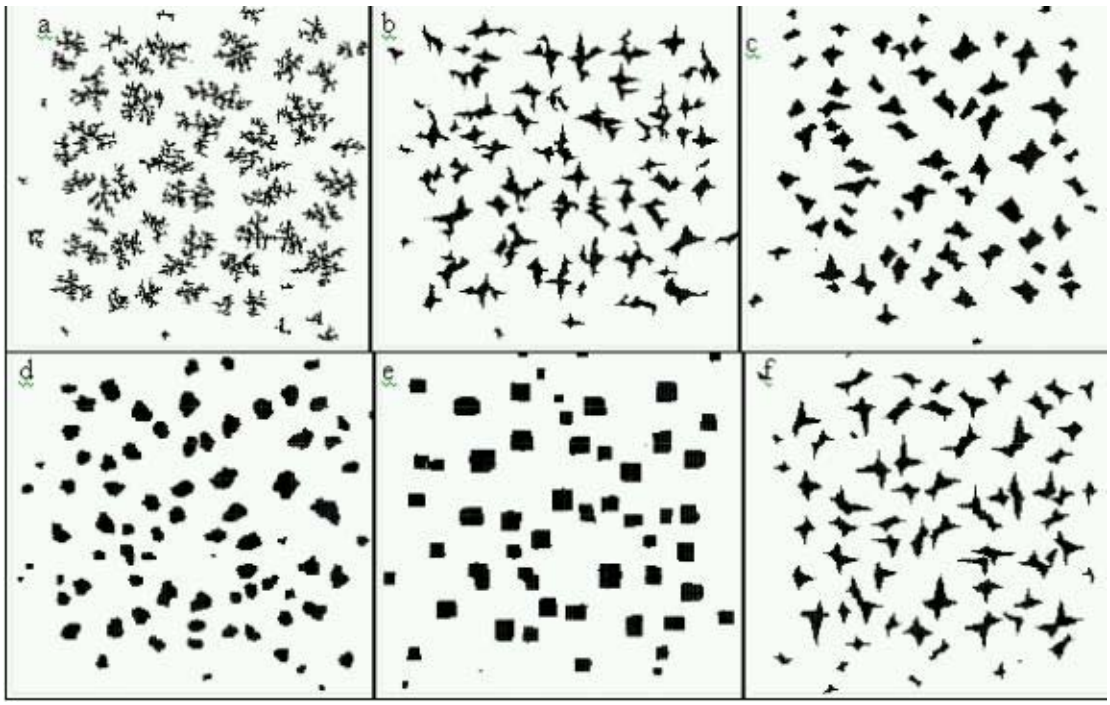

Figure 5.8 Variation of island morphologies with temperature. KMC simulations of two-dimensional island grown on a square lattice at temperature (a) 50K; (b) 100K; (c) 200K; (d) 300K; (e) and (f) 500K. The only difference between (e) and (f) is the higher corner barrier for the latter case.

slow flux rate. Here a smaller terrace diffusion barrier can result in a higher flux rate. Unfortunately on fcc (100) surfaces, the terrace diffusion barriers are usually even higher (~0.4eV). Let us suppose a realistic slow flux rate $F \sim 10^{-5}$ ML/s and obtain islands having similar sizes as Figure 5.8. For V_t=0.4eV, this would require the substrate temperature to be as high as 250K.

The crossover in island morphology from Figure5.8 (a) to Figure5.8 (e) is caused by the increase in temperature. A comparison between Figure5.8 (e) and (f) shows that, even though edge diffusion is very frequent in both cases (in fact more frequent in Figure 5.8(f)), the islands can still be noncompact if the events of corner crossing is too infrequent (as in Figure 5.8(f), corresponding to a higher corner barrier). This comparison also allows us to conclude that even before the temperature increases to 200K (Figure5.8 (c)), the effect of edge diffusion in influencing the island morphologies should have been saturated. All changes of morphologies thereafter are due to the activation of corner diffusion.

We have also used the parameters employed in these simulations to crosscheck the validity of Eq. (32) quantitatively. For parameters corresponding to Figs.5.8 (a-f), we obtain (R, Re, Rc)= (2.3×10^{12}, 130, 2.3×10^{12}), (1.3×10^{4}, 0.11, 1.3×10^{4}), (1.9, 5.2×10^{-3}, 1.9), (0.014, 4.9×10^{-4}, 0.014), (9.0×10^{-4}, 1.5×10^{-4}, 7.5×10^{-4}), and (16, 6.9×10^{-5}, 16) respectively. Based on these values, we should expect noncompact islands in Figs. 5.8(a), (b) and (f); compact islands in Figs. 5.8(d) and (e); and crossover behavior in Figure 5.8(c). These theoretical predictions are in

complete agreement with the simulation results.

We have adopted many other different sets of diffusion barriers to study what specific roles these diffusion barriers play in sub-monolayer island growth. In these simulations, the standard for the choice of deposition rate is that enough terrace diffusion happens so that we can get an island large enough for us to discuss its shape. All these simulations suggest that if the corner barrier is slow while edge diffusion is fast, islands resemble dendrite morphologies as in Figure 5.7 (k); if the edge barrier is slow, islands resemble random fractal morphologies as in Figure 5.8 (a); if both corner and edge diffusions are active, compact islands are obtained.

5.7.3.4 Simulation of growth in real systems

We first calculate the diffusion barriers on three fcc (100) metal surfaces with EAM (Embedded-Atom Method)[16]. Based on these parameters, 2-D kinetic Monte Carlo simulations are carried out for Cu/Cu (100) and Ag/Ag (100). Some more detailed processes are considered, which are illustrated in Figure 5.9, with corresponding barriers in Table 5.2.

It is important to notice that for these fcc (100) surfaces, the shear splitting barrier of dimers or linear chains are very close or even smaller than that for adatom terrace diffusion, which seems to be contradictory to the assumption made in STM analysis that dimer is more stable than single adatom residing on a terrace. This assumption is important in the theoretical extraction of diffusion barrier from STM

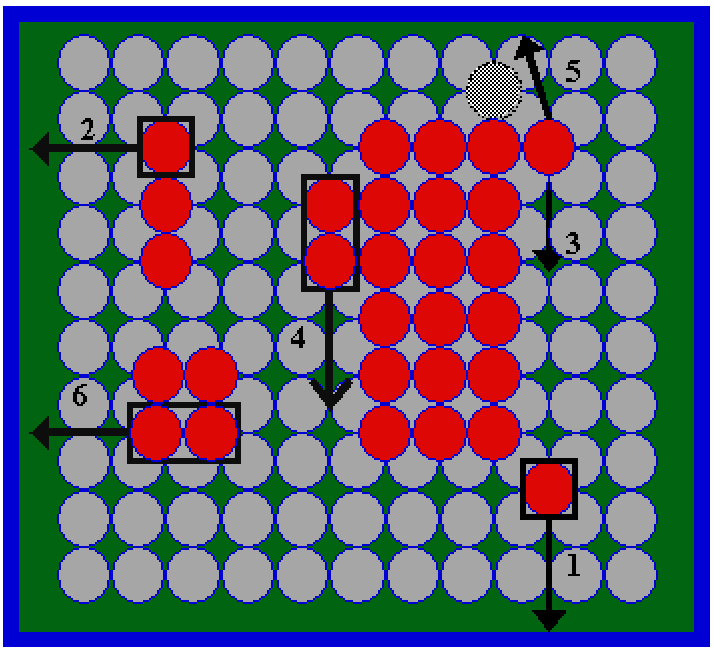

Figure 5.9 More detailed diffusion processes. This figure is similar to Figure 5.6, except that we consider more complicated diffusion processesThe corresponding barriers for several metals are given in Table 5.3. Terrace diffusion, linear chain splitting, single atom edge diffusion, dimer edge diffusion, corner crossing, and dimer shearing are indicated by the label from “1” to "6" respectively.

Table 5.2 Diffusion barriers calculated with EAM

Process	Cu/Cu(100) (eV)	Ag/Ag(100) (eV)	Ni/Ni(100) (eV)
E1	0.505	0.478	0.632
E2	0.494	0.480	0.611
E3	0.265	0.260	0.337
E4	0.503	0.474	0.624
E5	0.555	0.519	0.681
E6	0.696	0.651	0.849

data of island density distributions. Since the effect of dimer or linear chain splitting is similar to corner crossing around a square site, we regard it as corner process as well.

In the following, we analyze the effect of corner diffusions in determining the surface morphologies by switching on them one by one. The simulation is carried out for Ag/Ag(100), at the temperature of 280K and flux rate of $3x10^{-4}$ ML/s. In Figure 5.10(a) no corner diffusion is allowed. The morphology is fractal, but not so well detached from each other as shown in Figure 5.8(a) because of the limited activation of adatom diffusion on terrace. In (b), the dimer and chain splitting are turned on. It is clear that the morphology is less fractal and becomes more compact. We further switch on dimer shearing in Figure 5.10(c). Since the temperature is relatively low (0.0241 eV) and the dimer shearing barrier is 0.17 eV higher than linear-splitting, the change of island morphologies compared to (b) is not dramatic.

Real simulations with all diffusion processes shown in Figure5.9 and diffusion barriers as indicated in Table 5.2 are given in Figure 5.11. For copper in (a), the temperature is 335K and the deposition rate is $5x10^{-4}$ ML/s. The size is 70x70 and the coverage is 0.34 ML. For silver in (b), the temperature is 325K and the deposition rate is $3x10^{-4}$ ML/s. These islands are well-defined compact squares.

For the fcc (100) systems of Cu/Cu, Ag/Ag, and Ni/Ni, taking our EAM results (Vt, Ve, Vc) = (0.505,0.265,0.555), (0.478,0.260,0.519), and (0.632,0.337,0.681), respectively (all in eV) and assuming $\nu_t=\nu_e=\nu_c=10^{12}$ s^{-1}, $F=10^{-4}$

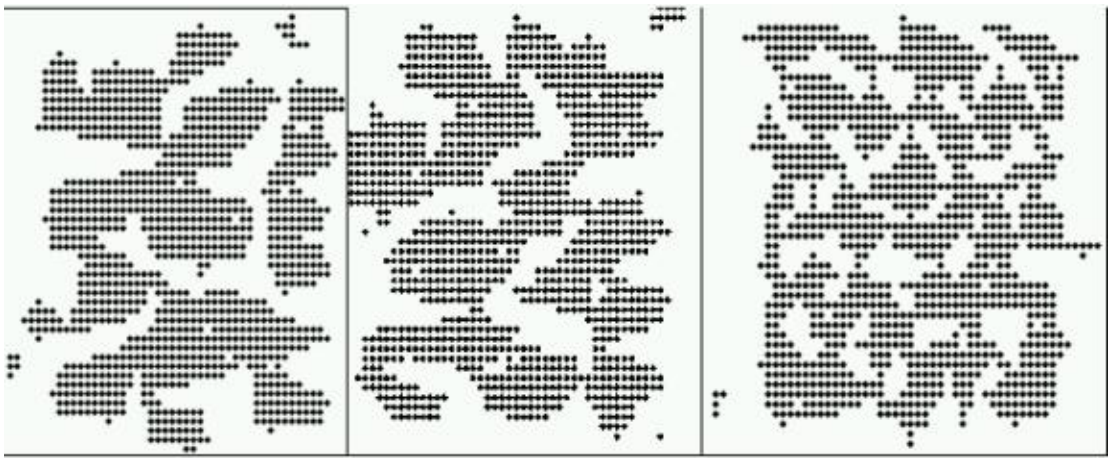

Figure 5.10 Control of cross-corner barriers in Ag/Ag(100). (a) All cross-corner mechanisms are prohibited. (b) Shearing of dimer and linear chains is allowed. (c) All processes including dimer shearing are activated.

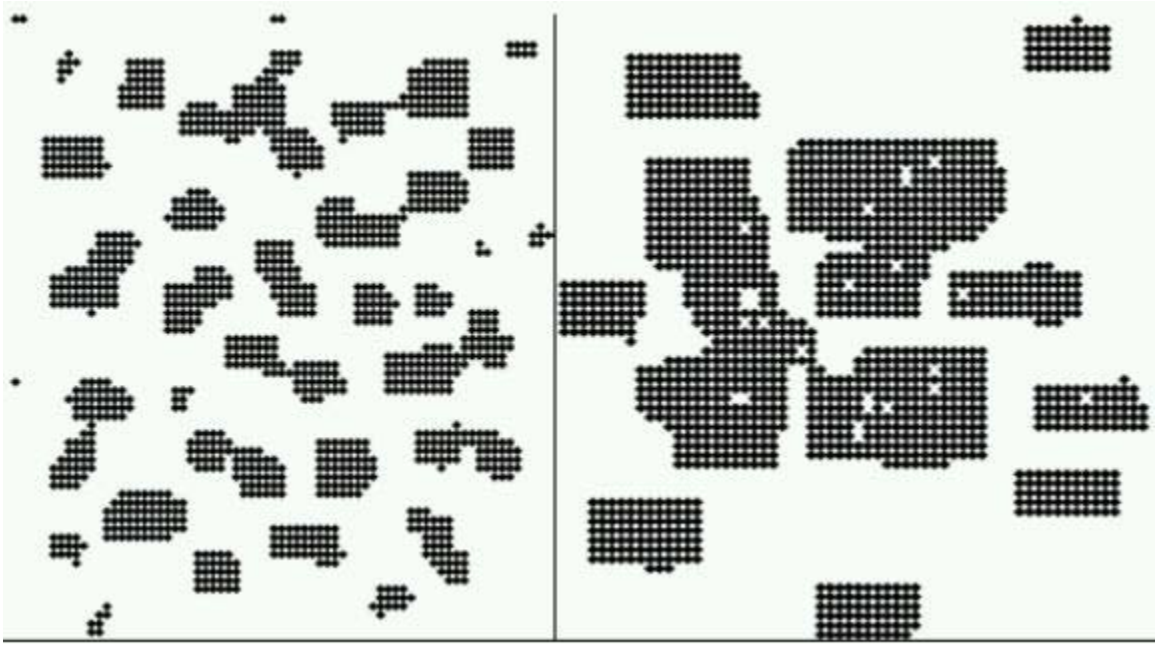

Figure 5.11 Simulations of island formation for two realistic systems. These simulations of island formation in homoepitaxial growth on fcc (100) surface of (a) Cu and (b) Ag are based on EAM calculations of diffusion barriers as shown in Table 5.2

MLs^{-1}, θ=0.1 ML, T=300K, we have R~$7.0x10^{-4}$ (Cu), $2.9x10^{-4}$ (Ag), and $7.8x10^{-3}$ (Ni), indicating that only compact islands can be obtained in these systems at such typical growth conditions. This conclusion again agrees with existing experiments [122,185,125-127].

5.7.4 Discussion s

5.7.4.1 Influence of the flux rate

As we mentioned earlier, it has been a long-standing puzzle in the literature to explain the experimental observation that upon decreasing the flux rate 100 times, the Ag dentritic islands formed on Pt (111) change their morphologies and assume those of the ramified fractals [179,195]. The formation of the orientational dentritic islands was thought to be the result of the asymmetric diffusion of adatoms from corner sites to type "A" and type "B" [173,164]. We test the possibility within our model to observe this behavior. However, our simulations with a reduction of the flux rate by about 200 times indicate that the relative barrier relations between the terrace, corner and edge diffusion scaled by temperature are the sole factors governing the island morphologies. In the ramified fractal growthregime, a decrease of the deposition rate leads to formation of larger fractals; within dentritic region, a decrease of flux rate leads to formation of larger dentritic islands. Figure 5.12 represents the simulation results of island morphologies at different deposition rates. The barriers are same as that used in the earlier study of temperature effect (Figure 5.8 (a)). The simulation

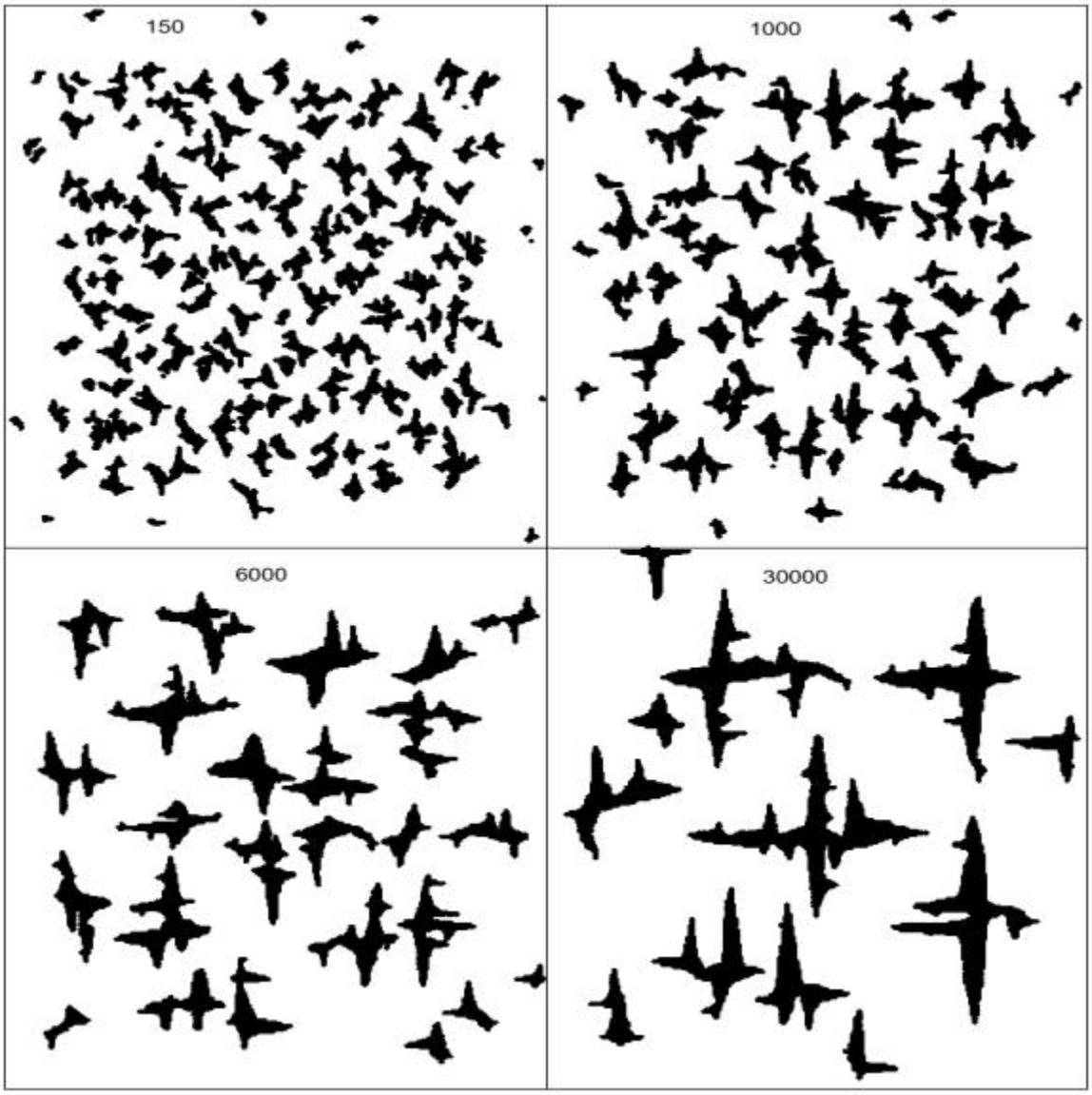

Figure 5.12 Variation of island morphologies with deposition rate. The numbers in the panels indicate the frequency at which an atom can be chosen to jump between the deposition of two consecutive atoms.

temperature is 100 K, at which the edge diffusion is activated but the corner diffusion is frozen. With the decrease of flux rate from $6x10^{-3}$ to $3x10^{-5}$ ML/s, smaller dendrites will collapse together to form larger ones. What we observe at high flux seems to be immature morphologies of what we can obtain at the low flux. The dentritic arms extend longer and longer as the deposition becomes slower and slower.

5.7.4.2 Growth of noncompact islands on square surfaces

In reality, it is known that it is easy to obtain random or dendrite fractals on fcc (111) surfaces. In homoepitaxial growth on fcc (100) surfaces, so far only compact islands have been observed. There have been some explorations [178] on the underlying reasons but a clear answer is still missing. So far theoretical and experimental studies have shown that, in general, $V_c > V_e >> V_t$ on hexagonal surfaces (fcc (111) or hcp (0001)), and $V_c \sim V_t >> V_e$ on fcc (100) surfaces (Table 5.2) [173,116,137-138,156]. Also it is typical that on hexagonal surface, the terrace diffusion barrier V_t <0.1eV while on square lattices V_t >0.4eV. According to the simulations obtained above, these barrier relationships means that :

(i) On fcc(100) surfaces, at temperatures (higher than 250K, as estimated above from a realistically low limit flux) where the terrace diffusion is fast enough to obtain sizable islands, corner crossing can also be appreciably activated because of the comparable terrace and corner diffusion barriers. This makes it unlikely to obtain dentritic islands. Because the edge diffusion is much faster than terrace diffusion, we

can never expect to get random fractals if we can not reverse this relationship.

(ii) On fcc(111) surfaces, at temperatures where terrace diffusion is activated to get sizable islands, edge diffusion is still frozen and it is possible to obtain random fractals. At higher temperatures where edge diffusion becomes active while corner diffusion is still slow, we have a chance to catch the shape transition from the random fractals to dendritic fractals. The distinction of edge diffusion on the "A" and "B" steps and corner diffusion toward the "A" step and the "B" step makes the shape transition on fcc(111) surfaces even more complicated [98-99]. Since the local tgeometries of hexagonal and square lattices are different while dendritic shapes resemble closely the symmetry of the substrate, it is reasonable to expect the dendritic shape is different from what is shown in Figs. 5.5 (a-f). Considering the differences in the barrier relations, we can also conclude from Eq.(20) that the temperature range for fractal growth on fcc(111) or hcp(0001) surfaces is much wider than it is on fcc(100) surfaces. Although Eq.(20) does not exclude the existence of the fractal growth regime on fcc(100) surfaces, the small difference between Vc and Vt makes it improbable under the growth condition to form sizable islands.

5.7.5 Conclusion

Our studies indicate that corner crossing can play an important role in influencing the island morphologies. Fast edge diffusion itself can not guarantee the formation of compact islands. Large corner barriers can lead to the formation of

dentritic islands, which are noncompact. Corner barrier is also tied with the appearance or disappearance of the symmetry of the substrate. These dentrite islands can be well defined by tuning the temperature and the flux rate, which may be useful in nano-technologies where the ability to form different types of islands with a narrow statistical distribution is important. In homoepitaxial growth on fcc(100) surfaces, the activation barrier for corner diffusion is comparable to that for terrace diffusion while edge diffusion is much faster than the first two, making it impossible to grow fractal patterns. On fcc(111) surfaces the subtle difference between the diffusion barriers allows a more complicated phase space for the island morphologies. It is possible that we can introduce some mechanisms such as strain [93,25] to tune these barriers. The importance of exchange [116] diffusion and detachment may complicate our model here. On anisotropic [129,93] surfaces, island morphologies can be quite different from what we have studied here. It is still difficult to understand the appearance of shape transition from dentritic to ramified fractals upon changing the flux from high rate to low rate. One possibility is to consider the dependence of diffusion temperature on the flux rate, which is related to the controversial problem of transient mobility [196].

Chapter 6 Summary

In the dissertation I have used multi-scale theoretical approaches to investigate the thermodynamic, kinetic, and dynamic properties of surface defects with various length scales. The multi-scale approaches range from first-principles calculation within density functional theory to empirical embedded atom method to statistical analysis to kinetic Monte Carlo simulations.

As introductory efforts, we have studied the properties of ideal surfaces based on our first-principles calculations. First, we have proposed a new method that has the promise to predict the direction of relaxation of the atoms in the surface layer strictly based on the bulk properties of the given system. Our fist-principles based interpretation of STM images within the framework of the Tersoff-Hamann theory has also achieved good agreement with STM experiments in revealing the anisotropy of electron density corrugations on several open surfaces of metallic systems.

In our study of the thermodynamic properties of intrinsic line defects on a vicinal TaC(910) surface, our Monte Carlo simulations in comparison with STM images have confirmed the existence of long-range attraction between steps.

In our study of the properties of extrinsic point defects underneath a GaAs surface, we have established through our theoretical analysis that many-body effects in a system with purely repulsive interactions can give rise to an effective attractive

interaction at high dopant densities. This study may have an important impact on better understanding of and possibly overcoming the fundamental solubility limits in doping of semiconductors.

In our study of the morphological evolution of monatomic-layer-height islands grown on surfaces, we have carried out Kinetic Monte Carlo simulations to illustrate the importance of island corner barriers. We have shown that if the island corner barrier effect is operational in preventing adatoms located at an island edge to reach a neighboring edge defining the island corner, the islands thus formed must be non-compact, in the form of fractal or dendrite islands. Furthermore, based on our embedded atom method (EAM) calculations and rate equation analysis, we have explained why fractal islands have rarely been observed on fcc(100) surfaces,

References

[1] G. Binnig, H. Rohrer, Ch. Gerber, and E. Weibel, Phys. Rev. Lett., 50, 120(1983)

[2] K. Takayanagi, Y. Tanishiro, M. Takahashi, and S. Takahashi, J. Vac. Sci. & Tech.A, 3, 1502(1985)

[3] H. C. Manoharan, C. P. Lutz, and D. M. Eigler, Nature, 403, 512(2000); M. F. Crommie, C. P. Lutz, and D. M. Eigler, Science, 262, 218(1993)

[4] W. K. Burton, N. Cabrera, F. C. Frank, Philos. Trans. R. Soc. London, Ser. A 243, 299 (1951)

[5] H. Brune, M. Giovannini, K. Bromann and K. Kern, Nature, 394,451(1998)

[6] J. L. Li, J. F. Jia, X. J. Liang, X. Liu, J. Z. Wang, Q.K. Xue, Z. Q. Li, J. S. Tse, Z.Y. Zhang, and S. B. Zhang, Phys. Rev. Lett., 88, 66101(2002)

[7] M. Tsuchiya, P. M. Petroff, and L. A. Coldren, App. Phys. Lett., 54, 1690(1989)

[8] N. A. Melosh, A. Boukai, F. Diana, B. Gerardot, A. Badolato, P.M. Petroff, J.R. Health, Science, 300, 5616(2003); F. Liu, J. Tersoff, and M.G. Lagally, Phys. Rev. Lett., 80, 1268(1998)

[9] Zheng Gai, G. A. Farnan, J. P. Pierce, and J. Shen, App. Phys. Lett., 81, 742(2002)

[10] J. Tersoff and D. R. Hamann, Phys. Rev. Lett., 50, 1998(1983); *ibid*, Phys. Rev. B 31, 805 (1985); *ibid*, Phys. Rev. Lett., 57, 440(1986)

[11] J.-K. Zuo, Tianjiao Zhang, J. F. Wendelken and D. M. Zehner, Phys. Rev. B, 63, 33404(2001)

[12] Ph. Ebert, Tianjiao Zhang, F. Kluge, M. Simon, Zhenyu Zhang, and K. Urban,

Phys. Rev. Lett., 83,757(1999)

[13] J. Zhong, Tianjiao Zhang, Z. Zhang, and M. G. Lagally, Phys. Rev. B 63, 113403 (2001)

[14] M. Metropolis, A.W. Rosenbluth, M.N. Rosenbluth, A.N. Teller and E. Teller, J. Chem. Phys., 21, 1087(1953); Tianjiao Zhang, MS Thesis, Peking University (1996)

[15] M.Bowker and D.A. King, Surf. Sci.,71, 583(1978); A. F. Voter, Phys. Rev. B 34, 6819(1986); H.C. Kang and W. H. Weinberg, J. Chem. Phys. ,90,2824(1989); H. Metiu, Y.-T. Lu and Z.Y. Zhang, Science, 255, 1088(1992); Z.Y. Zhang and M.G. Lagally, Science 276, 377(1997)

[16] M.S. Daw and M.I. Baskes, Phys. Rev. Lett.,50, 1285(1983) ;ibid, Phys. Rev. B, 29, 6443(1984); J.H. Rose, J.R. Smith, F. Guinea and J. Ferrante, Phys. Rev. B, 29, 2963(1984); S. M. Foiles, M. I. Baskes and M. S. Daw, Phys. Rev. B, 33, 7983(1986)

[17] Tianjiao Zhang, J.-H. Cho, E. W. Plummer, Z.Y. Zhang, to be submitted

[18] Tianjiao Zhang, L. Petersen, Z.Y. Zhang, E. W. Plummer, to be submitted

[19] P. Hohenberg and W. Kohn, Phys. Rev. 136, B684(1964)

[20] W. Kohn and L. J. Sham, Phys. Rev. 140, A1133(1965)

[21] J.P. Perdew and Y. Wang, Phys. Rev. B, 45, 13244(1992); J. P. Perdew, S. Burke, and M. Ernzerhof, Phys. Rev. Lett., 77, 3865(1996)

[22] P. Blaha, K. Schwarz, and J. Luitz, WIEN97, Vienna University of Technology 1997, (improved and updated UNIX version of the original copyrighted WIEN-code,

which was published by P. Blaha, K. Schwarz, P. Sorantin, and S. B. Trickey, in Comput. Phys. Commun. 59, 399(1990))

[23] K, Binder(Ed), *Applications of the Monte-Carlo Methods in Statistical Physics*, (Springer, Heidelberg, 1983)

[24] M. G. Lagally, Physics Today, Nov. 1993, p24-31

[25] H. Ibach, Surf. Sci. Rep., 29, 193(1997); inid, 35, 71(1999)

[26] P. Hanesch and E. Bertel, Phys. Rev. Lett., 79,1523(1997)

[27] X.-S. Wang, J.L. Goldberg, N.C. Bartelt, T.L. Einstein and E. D. Williams, Phys. Rev. Lett. 65,2430 (1990)

[28] J. Frohn, M. Giesen, M. Poensgen, J. F. Wolf, and H. Ibach, Phys. Rev. Lett. 67, 3543 (1991)

[29] C. Alfonso, J. C. Heyraud and J.J. Metois, Surf. Sci. 262,371(1992)

[30] S. Song and S.G. Mochrie, *Phys. Rev. Lett*. 73, 995(1994)

[31] E.D. Williams, Surf. Sci., 299/30, 502(1994)

[32] W.W. Pai, J.S. Ozcomert, N.C. Bartelt, T.L. Einstein and J.E. Reutt-Robey, Surf. Sci., 307, 747(1994)

[33] M. Giesen, Surf. Sci., 370, 55(1997); Z.-T., Tian and T.S. Rahman, Phys. Rev. B, 47, 9751(1993)

[34] V. I. Marchenko and A. Y. Parshin, Zh. Eksp. Teor. Fiz. 79, 257(1980) [Sov. Phys. JETP 52, 129(1980)]

[35] A. F. Andreev and Yu. A. Kosevich, Zh. Eksp. Teor. Fiz. 81, 1435(1981) [Sov.

Phys. JETP 54, 761(1981)]

[36] L.D. Landau and E. M. Lifshitz, *Theory of Elasticity (3rd)*,(translated by J.B. Sykes and W.H. Reid, Pergamon Press) 1986

[37] J. Steward, O. Poland and J.M. Gibson, Phys. Rev. B, 49, 13848(1994)

[38] A.C. Redfield and A. Zangwill, *Phys. Rev*. B46, 4289 (1992)

[39] J. Tersoff, Y.H. Phang, Z.Y. Zhang and M.G. Lagally, 75, 2730(1995)

[40] L.E. Shilkrot and D.J. Srolovitz, Phys. Rev. B, 53, 11120(1996)

[41] J. M. Blakely and R.L. Schwoebel, Surf. Sci. 26, 321(1971)

[42] M.C. Payne, N. Roberts, R.J. Needs, M. Needels, and J.D. Joannopoulos, Surf. Sci. 211/212,1(1989).

[43] K.H. Lau and W. Kohn, Surf. Sci., 65, 607(1977)

[44] E. Rolley, E. Chevalier, C. Guthmann and S. Balibar, Phys. Rev. Lett ,72, 872(1994)

[45] L. Barbier, L. Masson, J. Cousty, B. Salanon, Surf. Sci., 345, 197(1996)

[46] D. O. Edwards, M. S. Pettersen, and H. Baddar A. F. Andreev, in *Excitations in 2D and 3D Quantum Fluids*, edited by A. F. G. Wyatt and H. J. Lauter (Plenum, New York, 1991) p.361

[47] E. Pehlke and J. Tersoff, Phys. Rev. Lett. 67, 1290(1991), and references therein.

[48] V.I. Marchenko, JETP Lett. 33, 381 (1981)

[49] E. E. Gruber and W. W. Mullins, J. Phys. Chem. Solids 28, 875 (1967)

[50] M.E. Fisher and D.S. Fisher, Phys. Rev. B, 25, 3192(1982)

[51] C. Jayakaprash, C. Rottman, and W. F. Saam, Phys. Rev. B 30, 6549(1984)

[52] Y. Akutsu, N. Akutsu, and T. Yamamoto, Phys. Rev. Lett. 61, 424(1988)

[53] N.C. Bartelt, T.L. Einstein and E.D. Williams, Surf. Sci. Lett. 240, L591(1990)

[54] Joós, T.L. Einstein and N.C. Bartelt, Phys. Rev. B, 43, 8153(1991)

[55] P. Noziegares, in: *Solids Far From Equilibrium*, edited by C. Godregache (Cambridge Univ. Press, Cambridge, 1991)

[56] K. Besocke and H. Wagner, Phys. Rev. B, 8, 4597(1973)

[57] K. Besocke, B. Krahl-Urban, and H. Wagner, Surf. Sci., 68, 39(1977)

[58] W. Kossel, Nachr. Ges. Wiss. Goumlttingen, Math.-Phys. Kl. 135(1927)

[59] I. Stranski, Z. Phys. Chem. (Leipzig) 136, 259(1928)

[60] R. Smoluchowski, Phys. Rev. 60, 661 (1941)

[61] M. D. Thompson and H. B. Huntington, Surf. Sci. 116, 522 (1982)

[62] V. V. Voronkov, Kristallografiya 12, 831(1967) [Sov. Phys. Crystallogr. 12, 728 (1968)]

[63] T. L. Einstein, CRC Crit. Rev. Solid State Mater. Sci. 1, 261(1978)

[64] K. H. Lau and W. Kohn, Surf. Sci. 75, 69(1978); K. H. Lau, and W. Kohn, Surf. Sci., 65, 607(1977)

[65] R.J. Phaneuf and E.D. Williams, Phys. Rev. Lett. 58, 2563 (1987)

[66] J.-K. Zuo and D.M. Zehner, Phys. Rev. B46, 16122 (1992)

[67] E. D. Williams, R.J. Phaneuf, Jian Wei, N.C. Bartelt and T.L. Einstein, Surf. Sci.

294, 219(1993)

[68] J.-K. Zuo, R.J. Warmack, D.M. Zehner and J.F. Wendelken, Phys. Rev. B47, 10743 (1993)

[69] J.-K. Zuo, J.M. Carpinelli, D.M. Zehner and J.F. Wendelken, Phys. Rev. B53, 16013(1996)

[70] K. Sudoh, T. Yoshinobu, H. Iwasaki and E.D. Williams, Phys. Rev. Lett. 80, 5152 (1998)

[71] V.B. Shenoy, Shiwei Zhang and W.F. Saam, Phys. Rev. Lett. 81, 3475(1998)

[72] M. Lassig, Phys. Rev. Lett. 77, 526(1996)

[73] S.M. Bhattacharjee, Phys. Rev. Lett. 76, 4568(1998)

[74] H. van Beijeren and I. Nolden, in *Structure and Dynamics of Surfaces II*, edited by W. Schommers and P. von Blanckenhagen (Springer Verlag, Berlin, 1987), pp. 259-300

[75] A. Rettori and J. Villain, J. Phys. (Paris) 49, 257(1988)

[76] M. Uwaha, J. Phys. Soc. Jpn. 57, 1681(1988)

[77] M. Ozdemir and A. Zangwill, Phys. Rev. B 42, 5013(1990)

[78] J.W.M. Frenken and P. Stoltze, Phys. Rev. Lett. 82, 3500 (1999)

[79] S. van Dijken, H.J.W. Zandvliet and B. Poelsema, Phys. Rev. B 55, 7864 (1997)

[80] J.R. Noonan, H.L. Davis and G.R. Gruzalski, J. Vac. Sci. Technol. A5, 787 (1987)

[81] O.L. Alerhand, D. Vanderbilt, R.D. Meade and J.D. Joannopoulos, Phys. Rev.

Lett., 61, 1973(1988)

[82] R. B. Dingle, Philos. Mag. 46, 861 (1955)

[83] R. M. Feenstra et al., Phys. Rev. Lett. 58, 1192 (1987); Ph. Ebert et al., Phys. Rev. Lett. 77, 2997 (1996)

[84] M. B. Johnson et al., Appl. Phys. Lett. 63, 2923 (1993)

[85] Ph. Ebert et al., Phys. Rev. B 51, 9696 (1995); Ph. Ebert, K. Urban, and M. G. Lagally, Phys. Rev. Lett. 72, 840(1994); G. Lengel et al., Phys. Rev. Lett. 72, 836 (1994)

[86] J. A. Stroscio, R. M. Feenstra, and A. P. Fein, Phys. Rev. Lett. 58, 1668 (1987); R. J. Hamers, J. Vac. Sci. Technol. B 6, 1462 (1988); C. Domke et al., J. Vac. Sci. Technol. B 16, 2825 (1998)

[87] J. B. Mullin et al., J. Appl. Phys. 47, 2584 (1976)

[88] T. T. Tsong, Phys. Rev. Lett. 31, 1207 (1973)

[89] Ph. Ebert et al., Phys. Rev. Lett. 76, 2089 (1996)

[90] K.-J. Chao et al., Phys. Rev. Lett. 79, 4822 (1997)

[91] T. L. Hill, *Statistical Mechanics* (McGraw-Hill, NewYork, 1956)

[92] S. Yu, T. Y. Tan, and U. Gösele, J. Appl. Phys. 69, 3547(1991)

[93] H. Brune, Surf. Sci. Rep., 31, 121(1998)

[94] R. Kern, G. Le Lay and J. J. Metois, Current Topics in Material Science (ed. E. Kaldis, Amsterdam, North-Holland), Vol 3, 131 (1979); E. Bauer, Z. Krist., 110, 372(1958); F.C. Frank and J.H. van der Merwe., Proc. Roy. Soc. London A 198,

205(1949); M. Volmer, A. Weber, Z. Phys. Chem., 119, 277(1926); I.N. Stranski, L. Krastanow, Sitzungsberichte der Akademie der Wissenschaften Wien, Mathematisch Naturwissenschaftliche Klasse, Abteilung IIb, Chemie, Band 146, 797(1938)

[95] J. A. Venables, G.D.T. Spiller, M. Hanbücken, Rep. Prog. Phys., 47, 399(1984)

[96] E. Bauer, J.H. v.d. Merwe, Phys. Rev. B 33, 3657(1986)

[97] G. Ehrlich and F. G. Hudda, J. Chem. Phys. 44, 1039 (1966)

[98] R. L. Schwoebel and E. J. Shipsey, J. Appl. Phys. ,37, 3682 (1966)

[99] B. Voigtländer, Surf. Sci. Rep., 43, 127(2001)

[100] Zhenyu Zhang, Fang Wu, and Max G. Lagally, Annu. Rev. Mater. Sci. 27, 525(1997)

[101] Zhenyu Zhang, Qian Niu and Chih-Kang Shih, Phys. Rev. Lett., 80, 5381(1998) and references therein

[102] J. Frenkel, Z. Phys., 26, 117(1924)

[103] G. Zinsmeister, Vacuum, 16, 529(1966); ibid, Thin Solid Films 7, 51 (1971)

[104] J.A. Venables, J.A. Venables, Phil. Mag. 17, 697(1973)

[105] G.S. Bales and D.C. Chrzan, Phys. Rev. B, 50, 6057(1994); A. K. Myers-Beaghton and D. D. Vvedensky, Phys. Rev. B, 42, 5544(1990)

[106] M. J. Stowell, Phil. Mag. 26, 349(1972)

[107] J. A. Venables , Phys. Rev. B, 36, 4153(1987)

[108] G.D.T. Spiller,P. Akhter and J. A. Venables, Surf. Sci. 131,517(1983)

[109] M.C. Bartelt, J.W. Evans, Phys. Rev. B, 54, 1(1996)

[110] S. Liu, L. Bönig, H. Metiu, Surf. Sci., 392, L56(1997)

[111] H. Brune, G.S. Bales, J. Jacobsen, C. Boragno, K. Kern, Phys. Rev. B, 60, 5991(1999)

[112] B. Müller, B. Fischer, L. Nedelmann, H. Brune, K. Kern, Phys. Rev. B, 54, 17858(1996)

[113] J. V. Barth, Surf. Sci. Rep.40, 75(2000)

[114] J.J.D. Miguel, A. Sánchez, E. Ceboilada, J.M., Gallage, J. Farrón, S. Ferrer, Surf. Sci., 189/190, 1062(1987); H. J. Ernst, F. Fabre, and J. Lapujoulade, Phys. Rev. B 46, 1929(1992)

[115] G. C. Wang and Q. Jiang, Surf. Sci. 324, 357(1995)

[116] G. L. Kellog, Surf. Sci. Rep., 21, 1(1994)

[117] E. W. Müller, Z. Phys., 131, 136(1951)

[118] T.T. Tsong, Atom-Probe Field Ion Microscopy, (Cambridge University Press, cambridge, 1990)

[119] D.W. Bassett and P.R. Webber, Surf. Sci., 70, 520(1978)

[120] J.D. Wrigley and G. Ehrlich, Phys. Pev. Lett., 44, 661(1980)

[121] G. Binnig, H. Rohrer, Ch. Gerber, and E. Weibel, Phys. Rev. Lett., 49, 57(1982)

[122] J. A. Stroscio, D. T. Pierce, R. A. Dragoset , Phys. Rev. Lett., 70, 3615 (1993)

[123] J. A. Stroscio, D. T. Pierce, Phys. Rev. B, 49, 8522(1994)

[124] H. Röder, E. Hahn, H. Brune, J.P. Bucker, K. Kern, Nature, 366, 141(1993)

[125] H.J. Ernst, F. Fabre, and J. Lapujoulade,Phys. Rev. B 46, 1929(1992)

[126] H. Durr, J.F. Wendelken, J.-K. Zuo, Surf. Sci. 328, L527 (1995)

[127] J. F. Wendelken, A. K. Swan, W. W. Pai, and J.-K. Zuo, in: Z. Y. Zhang and M. G. Lagally(Eds.) Morphological Organization in Epitaxial Growth and Removal (World Scientific, 1998) p320

[128] M. Bott, M. Hohage, M. Morgenstern, T. Michely, G. Comsa, Phys. Rev. Lett., 76, 1304(1996)

[129] H. Brune, H. Röder, C. Boragno, K. Kern, Phys. Rev. Lett., 73, 1955(1994)

[130] P. J. Feibelman, Phys. Rev. Lett., 65, 729(1990)

[131] P. J. Feibelman, Phys. Rev. Lett., 58, 2766(1987)

[132] G.L. Kellogg, A.F. Voter, Phys. Rev. Lett., 67 622(1991)

[133] G.L. Kellogg, Appl. Surf. Sci., 67, 134(1993)

[134] Tianjiao Zhang and Zhenyu Zhang, unpublished

[135] A.F. Voter, Proc. SPIE, 821, 214 (1987);J. B. Adams, S. M. Foiles, and W. G. Wolfer, J. Mater. Res., 4, 102 (1989)

[136] D. J. Oh and R. A. Johnson, J. Mater. Res. 3, 471 (1988)

[137] C. L. Liu, J. M. Cohen, J. B. Adams, and A. F. Voter, Surf. Sci., 253, 334 (1991)

[138] C-L. Liu and J. B. Adams, Surf. Sci., 265, 262 (1992)

[139] M. Karimi, G. Vidali, and I. Dalins, Phys. Rev. B 48, 8986 (1993)

[140] C. L. Liu, Surf. Sci. 316, 294 (1994)

[141] M.Karimi, T. Tomkowski, G. Vidali and O. Biham, Phys. Rev. B, 52, 5364 (1995)

[142] Z. P. Shi, Z.Y. Zhang, A. K. Swan, and J. F. Wendelken, Phys. Rev. Lett. 76., 4927(1996)

[143] P.R. Schwoebel, S.M. Foiles and C.L. Bisson, Phys. Rev. B, 40, 10639(1989)

[144] L. D. Roelofs, S. M. Foiles, M. S. Daw, and M. I. Baskes, Surf. Sci. 234, 63 (1990)

[145] J. S. Nelson, M. S. Daw, and E. C. Sowa, Phys. Rev. B 40, 1465 (1989)

[146] M. Karimi and M. Mostoller, Phys. Rev. B 45, 6289 (1992)

[147] P.A. Taylor, J.S. Nelson and B.W. Dodson, Phys. Rev. B, 44, 5834(1991)

[148] U. Landman, W. D. Luedtke and E.M. Ringer, Wear, 153, 3(1992)

[149] S. M. Foiles, Phys. Rev. B 32, 7685(1985)

[150] J.K. Nørskov and N.D. Lang, Phys. Rev. B 21, 2131(1980)

[151] N D Lang and W Kohn, Phys. Rev. B,1, 4555(1970)

[152] M. C. Payne, M. P. Teter, D. C. Allan, T. A. Arias, and J. D. Joannopoulous, Rev. Mod. Phys. 64, 1045 (1992)

[153] A. R. Williams, P. J. Feibelman, and N. D. Lang, Phys. Rev. B 26, 5433 (1982)

[154] P.J. Feibelman, Phys. Rev. B 35, 2626 (1987) and reference therein

[155] P.J. Feibelman, J.S. Nelson, G.L. Kellogg, Phys. Rev. B, 49, 10548(1994)

[156] R. Stumpf and M. Scheffler, Phys. Rev. B,53, 4958(1996)

[157] M. Scheffler, J. Neugebauer, and R. Stumpf, J. Phys. Condensed Matte, 5,

A91(1993)

[158] R. Stumpf and M. Scheffler, Surf. Sci., 307-309, 501(1994)

[159] R. Stumpf and M. Scheffler, Phys. Rev. Lett. 72, 254(1994)

[160] X. Gonze, R. Stumpf, and M. Scheffler, Phys. Rev. B 44, 8503(1991); J. Neugebauer and M. Scheffler, Phys. Rev. B 46, 16067 (1992)

[161] B. Lang, R.W. Joyner, and G.A. Somorjai, Surf. Sci. 30, 440(1972); M.A. van Hove and G.A. Somorjai, Surf. Sci.,92, 489(1980); D. R. Eisner and T.L. Einstein, Surf. Sci., 286, L559 (1993)

[162] J.S. Nelson and P.J. Feibelman, Phys. Rev. Lett. 68, 2188(1992)

[163] P.J. Feibelman, Phys. Rev. Lett. 69, 1568(1992)

[164] M. Hohage, M. Bott, M. Morgenstein, Z. Y. Zhang, T. Michely, and G. Comsa, Phys. Rev. Lett., 76,2366(1996)

[165] C.M. Zhang, M.C. Bartlet, J.M. Wen, C.J. Jenks, J.W. Evans, P.A. Thiel, J. Cryst. Growth, 174, 851(1997)

[166] G. Boisvert, L.J. Lewis, M.J.Puska and R.M. Nieminen, Phys. Rev. B, 52, 9078(1995)

[167] P. J. Feibelman, Surf. Sci., 313, L801(1994)

[168] C. Ratsch, A.P. Seitsonen and M. Scheffler, Phys. Rev. B, 55, 6750(1997)

[169] J.J. Mortensen, B. Hammer, O.H. Nielsen, K.W., Jacobsen and J.K. Nørskov, in: A. Okiji, H. Kasai, K. Makoshi (Eds.), Elementary Processes in Excitations and Reactions on Solid Surfaces, vol. 121, (Springer, Berlin, 1996) p173

[170] T.A. Witten and L.M. Sander, Phys. Rev. Lett.,47, 1400(1981)

[171] T.A. Witten and L.M. Sander, Phys. Rev. B, 27, 5686 (1983).

[172] P. Meakin, Phys. Rev. A, 27, 1495(1983)

[173] H. Brune, K. Bromann, J. Jacobsen, K. Jacobsen, P. Stoltze, J. Nørskov, and K. Kern, Surf. Sci. 349,L115 (1996)

[174] B Gleich, M. Ruff, R J Behm, Surf. Sci. 386, 48(1997)

[175] F B. de Mongeot, M Scherer, B Gleich, E Kopatzki, and R J Behm, Surf. Sci. 411, 249(1998)

[176] J. Villain, J. Phys. I 1,19(1991)

[177] M. G. Lagally and Z.Y. Zhang, Nature, 417, 907(2002)

[178] Z.Y. Zhang, X. Chen, M. G. Lagally, Phys. Rev. Lett. 73,1829(1994)

[179] H. Brune, C. Romainczyk, H. Röder and K. Kern, Nature, 369, 469(1994)

[180] R.Q. Hwang, J. Schroder, C. Gunther, and R.J. Behm, Phys. Rev. Lett. 67, 3279 (1991)

[181] M. Bott, T. Michely, and G. Comsa, Surf. Sci. 272, 161 (1992)

[182] T. Michely, M. Hohage, M. Bott, and G. Comsa, Phys. Rev. Lett. 70, 3943(1993)

[183] H. Roder, K. Bromann, H. Brune, and K. Kern, Phys. Rev. Lett. 74, 3217 (1995)

[184] M. Kalff, G. Comsa, and T. Michely, Phys. Rev. Lett. 81,1255(1998)

[185] E. Kopatzki, S. Gunther, W. Nichtl-Pecher, and R.J. Behm, Surf. Sci.,284,154

(1993)

[186] B. Müller, L. Nedelmann, B. Fischer, H. Brune, J.V. Barth, and K. Kern, Phys. Rev. Lett. 80 ,2642(1998)

[187] A. Brodde, Wihelmi, D. Badt, H. Wengelnik, and H. Neddermeyer, J. Vac. Sci. Technol. B 9, 920(1991)

[188] G.S. Bales and D.C. Chrzan, Phys. Rev. Lett., 74, 4879(1995)

[189] A. Pimpinelli, J. Villain, and D.E. Wolf, J. Phys., (Paris), 3, 447(1993)

[190] M.C. Bartelt and J.W. Evans, Surf. Sci. 314,L829(1994)

[191] W.W. Mullins, R.F. Sekerka, J. Appl. Phys., A., 34, 323(1966)

[192] Y.G. Li, M.C. Bartelt, J.W. Evans, N. Waelchli, E. Kampshoff, and K. Kern, Phys. Rev. B 56, 12539 (1997)

[193] Y.W. Mo, J. Kleiner, M.B. Webb, M.G. Lagally, Phys. Rev. Lett., 66, 1998(1991)

[194] A. Pimpinelli, J. Villain, and D.E. Wolf, Phys. Rev. Lett.,69, 985 (1992)

[195] H. Brune, K. Bromann, H. Röder and K. Kern, Thin Solid Films, 264, 23 (1995)

[196] W.F. Flynn, J.W. Evans, and P.A. Thiel, J. Vac. Sci. Technol. A 7(1989) 2162

Appendices

Appendix A Relaxation of Lattice Structure on Perfect Metallic Surfaces

A.1 Introduction

A.1.1 Charge smoothing and Finnis-Heine model

There has been a long-standing interest in understanding the modification of ionic positions near metallic crystal surfaces, especially for the design of molecular devices and for the electrical connection of micro devices. After an infinite crystal is split into halves, the energy of the atoms close to the exposed surfaces increases sharply. These atoms move toward either the vacuum or the bulk. As early as 1941, Smoluchowsky [1] thought that, according to quantum theory, because of the sharp increase of electron density corrugation along the boundary, the kinetic energy of electrons near the surface would increase significantly. To decrease the energy, some of electrons should move toward the bulk. The weakening of binding potential field acting on surface electrons should also allow the spreading of some electrons toward the vacuum. This idea is demonstrated in Figure A.1. Later, Finnis and Heine (FH) [2] presented arguments that the elementary concepts governing the bulk total energy and crystal structure of sp bonded metals may be also relevant at the surface. They concluded that the dominant feature governing ionic relaxation at the surface of such

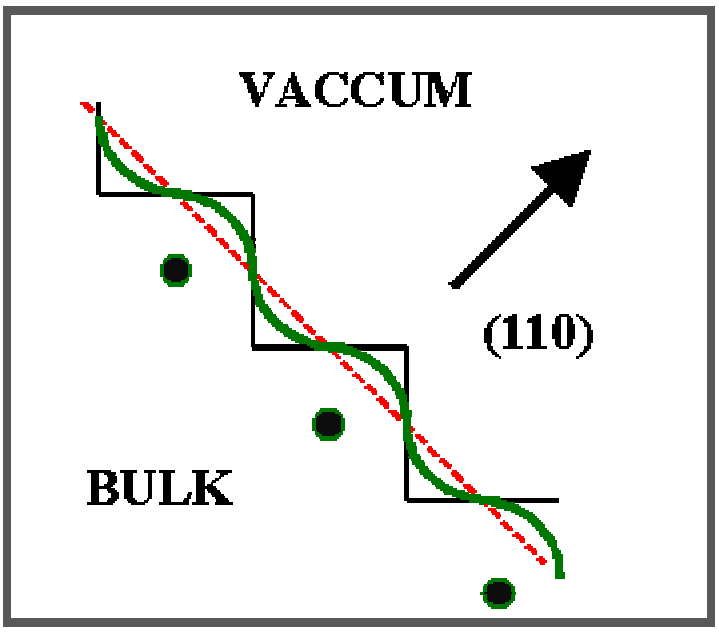

Figure A.1 Electron redistribution at surfaces. Smoluchowsky [1] thought that after the bulk is cut along the zigzag Wigner-Size boundary, charge smoothing leads to a flat electron density profile. Further charge spreading brings to a sinuous distribution.

a metal is the electrostatic force on a surface ion arising from a uniform background density of electrons filling the ion's 'surface-flattened' Wigner-Seitz cell (Figure A.1). This simple surface-cell model is based on the above charge-smoothing concept. The application of this idea to the fcc (111), (001) and (110) surfaces of aluminum predicted ionic relaxations in qualitative agreement with reported low-energy electron diffraction (LEED) determinations [3]. Later this model was widely used to investigate why contraction on open surfaces (such as fcc (110)) is larger than that on close surfaces (such as fcc (111)).

Going beyond the study of Finnis and Heine, Alldredge and Kleinman [4] considered the importance of crystalline effect. Their self-consistent electronic structure calculations of the lithium bcc (001) surface and the initial forces of relaxation suggested that crystalline effects not considered by FH [2] are very important. Alldredge and Kleinman [4] had used Hellmann-Feynman theory to calculate the electrostatic force on the surface ions as a function of their displacements normal to the surface. In their treatment, ion positions, except the outmost layer, are kept fixed. This is based on their observation that the initial force of relaxation on deeper-layer ions is about 30 times smaller than that on a surface ion. However, due to their limited computation power in 1974, they only calculated the self-consistent electronic distribution for one set of ionic positions. The Hellmann-Feynman forces at other significantly different position were based on the same

electronic distribution, which as noted by the authors is a violation of the adiabatic approximation.

A.1.2 Abnormal expansion and contraction on closely packed surfaces

Recently, quite a few LEED experiments [7-15] and ab initio calculations [8,13,16-28] indicated that for a given geometry of the metal surfaces, the relaxation behaviors can change drastically, from expansion in hcp (0001) Be [7-8, 17-19], Mg [9,20], fcc (111) Al [14,16], Pt [15,28] to contraction in hcp (0001) Ti [22-23], Zr [21-23], Ru [13,24](see Table A.1). In the traditional Finnis-Heine picture of surface relaxation [2], it was expected that every surface should contract. For closely packed surface, it is predicted that only a small contraction should happen, which is contradictory to the above observations. To explain the controversy, several pictures based on surface states and chemical bond characteristics have been proposed [16-19,22].

Specifically, Feibelman [22] used the difference of hybridization energy gain vs promotion energy cost between Be and Zr (also Ti) to explain the phenomena that a hcp (0001) surface of Be shows extraordinary expansion. For Be, a large energy (2.7eV) is needed to promote the excitation to form chemical bonds, which is difficult. According to his argument, this energy can be gained only by significant hybridization. At the surface of (0001), since half of the neighbors have been removed, it is likely that surface atoms will not bond strongly with the second-layer

Table A.1 Surface relaxation of several close packed surfaces

Surface	Experiment (LEED) (%)	Theory (%)
Be hcp(0001)	+3.1±0.7(110K) [8,7]	+2.5 [17-19,8]
Mg hcp(0001)	+1.9±0.3 (100K) [9]	+1.5 [20]
Al fcc(111)	+1.7±0.3 (160K) [14]	+1 [16]
Pt fcc(111)	+1.1±0.4 (90K) [15]	+1.25 [28]
Ti hcp(0001)	-2±2(300K) [10]	-7.7 [22-23]
Zr hcp(0001)	-1.6±0.8(300K) [11]	-6.3 [21-23]
Ru hcp(0001)	-2.1(100K) [13]	-4.0 [13,24]

atoms any more and the p_z component in the bulk Be is demoted to the atomic Be. Demotion to p_x-p_y is difficult because intra-first-plane bonds can not get appreciable stronger since they can not get shorter. This leads to the expansion. This argument is corroborated partly by the fact that the dimer bond of Be is unusually 11% longer than the nearest-neighbor distance in the bulk. In contrast, promoting the $4d^2 5s^2 \rightarrow 4d^3 5s^1$ in Zr ($3d^2 4s^2 \rightarrow 3d^3 4s^1$ in Ti) costs only 0.5ev (0.8ev in Ti), which means that after removing one half of the neighbors, it is still possible to form strong chemical bonds with the second-layer atoms. And the bonds between inter-plane atoms become stronger and shorter, which is because that a d shell in Zr and Ti offers more orbital flexibility than a p shell in Be since there are three more d orbitals with significant inter-planar weight rather than one. This leads to contraction, which is also partially corroborated by their calculation that the dimer bond of Zr (Ti) is 29% (33%) shorter than the nearest-neighbor distance in the bulk. This chemical picture is the same as the "inverse bond-order bond-length correlation" observed for the group II metals [29].

In this chapter, I present our study of surface relaxation based on a conjecture about the very dynamic process of the surface atoms' response from the moment the bulk is split. More attention is paid on a qualitative understanding of the direction of relaxation than a quantitative agreement of the relaxation scale with experimental results. By this way, we seek to know whether it is possible to predict the direction of surface relaxation from the electron density distribution of the bulk crystal. In

previous ab initio studies of surface relaxations, even for the same crystal, if we want to know the relaxation of the material along different surface orientations, it will be necessary to construct different surface unit cells and carry out intensive self-consistent minimization.

A.2 Conjecture of Surface Relaxation Dynamics

The ideal emulation of the physical relaxation process can be divided into four major steps:

(1) An infinite crystal is split along certain boundary into halves.

(2) Under new circumstances, electrons close to the exposed surfaces respond immediately and find their ground states within the freeze-in lattice frame (also called as charge smoothing or redistribution).

(3) Net forces acting on surface nuclei drive them to relax to the configuration of lowest energy.

(4) Step (2) and (3) repeated once and again until the system arrives at the final configuration where both the electrons and the lattice are fully relaxed.

Here we assume that the initial steps (1), (2) and (3) are dominant processes and their contributions determine whether the first inter-layer space should contract or expand while the step (4) would only change the scale of the final result. Three different terminology will be used to describe the surface during the relaxation: fresh-cut

surface (neither electrons nor nuclei relaxed, as in step 1); ideal surface (electrons fully relaxed while nuclei not relaxed, as in step 2); optimized surface (both electrons and lattice fully relaxed, as in step 3 or 4).

In general, the force acting on an atom in the bulk crystal can be written as:

$$F_{bulk} = F^{u}_{bulk} + F^{l}_{bulk} \qquad (1)$$

in which the first and second terms in the right are attributed to the force contribution from the upper and lower part of materials as divided by the boundary (Figure A.2). Despite that their sum is zero, in general these two terms separately are not equal to zero. In each part, the force contribution can be subdivided into that due to electrons and nuclei, respectively. For the lower part, it can be written as:

$$F^{l}_{bulk} = F^{l}_{e} + F^{l}_{n} \qquad (2)$$

After we cut the bulk along the boundary, we throw away the upper part. According to our definition of fresh-cut surface, the force represented by Eq. (2) is also that felt by atoms on fresh-cut surfaces. For the ideal surface, the electrons are redistributed and the force acting on a surface atom can be written as:

$$F_{ideal} = F^{l}_{bulk} + \delta F^{l}_{e} \qquad (3)$$

in which the second part is the force contribution due to the net change of electron density distributions. This part is also called as contribution from Friedel oscillation. If we can find such a cutting boundary so that δF^{l}_{e} is negligible,

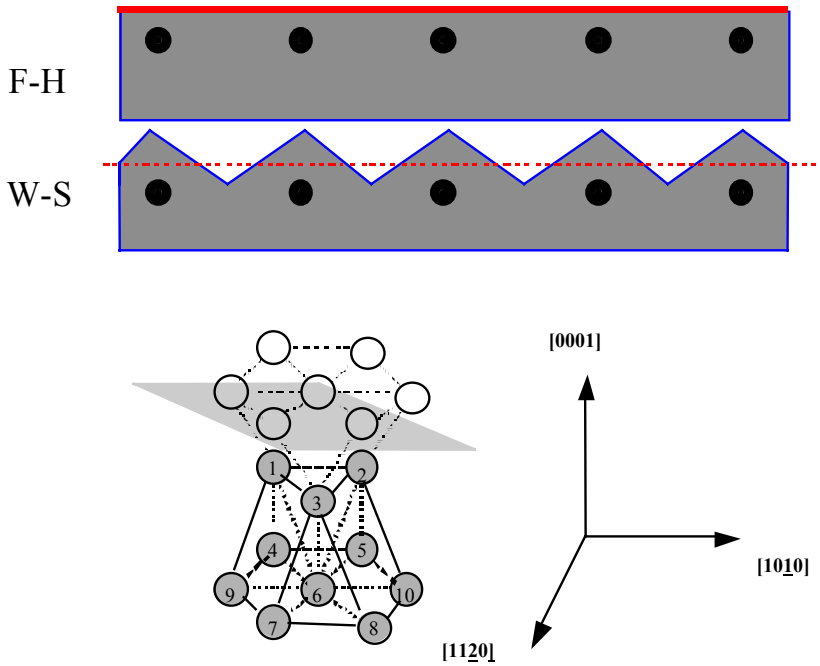

Figure A.2 Sketch of fresh-cut surfaces. The zigzag curve is along the Wigner-Seitz (W-S) boundary; the flat line is the Finnis-Heine (F-H) cut as represented by the shaded plane cutting the hcp lattice in the bottom. The Finnis-Heine plane is the middle plane of two continuous layers parallel to (0001). Atoms 1, 2 and 3 are part of the first layer of the hcp (0001) surface. The projections of 1,2,3 onto the second layer are located at the triangular centers bound by (4,6,9), (5,6,10), and (6,7,8) respectively.

$$F_{ideal} \approx F^{l}_{bulk} \qquad (4)$$

it will be possible for us to predict the direction of the relaxation purely from the bulk information.

In step (1), it is necessary to define how the bulk is cut. As to the bulk itself, usually people in solid state physics would like to adopt the Wigner-Seitz cell and suppose that it is a natural boundary between atoms. It is essential to recognize that this is based on a point charge concept and local symmetry arguments. A more physical boundary is likely to follow where the electron density is minimal, because there the bonds between atoms along this boundary should be the weakest. However, constructing such a physical boundary is much more complicated than the Wigner-Seitz boundary. It is unknown whether there can be some analytic deduction besides brute determination from ab initio calculations. In the present study, we choose two simpler profiles. One is called Finnis-Heine cut as adopted in Finnis and Heine's paper [2]. It is important to notice that in their original paper, this boundary is taken as the ideal surface, i.e., after charge smoothing. Here we choose it as a starting boundary of the fresh-cut surface. The next one is the Wigner-Seitz cut along the Wigner-Seitz boundary, which was also used by Smoluchowsky [1] as the starting boundary.

In the following calculation of the force on the fresh-cut surface, we do not use a corresponding planar summation technique similar to that of [4]. It is because

LAPW methods expand the wave functions inside the muffin-tin using the atomic orbitals, which makes it difficult to express them in the plane wave basis again. Instead, we just make the clumsy summation of the Coulomb force cell by cell. The charge neutrality is maintained within 0.2% when cutting boundaries are constructed.

A.3 Prediction of Surface Relaxation on Hcp (0001) Be and Zr

A.3.1 Calculation of fresh-cut surfaces

The following numerical analysis is based on full-potential LAPW calculation using WIEN97 software [31]. We choose hcp (0001) Be and Zr as examples (Table A.1). It is observed that for Be, the first inter-layer space is expanded [7-8, 17-19] while for Zr it is contracted [11,21-23], which provide a reliable standard to test our ideas. The improved generalized gradient approximation (GGA) [32] of the exchange-correlation function is used. The charge density and potential cut-off is 196 Ry. In the bulk calculation, the irreducible Brillioun Zone is sampled with 240 k points. The calculated lattice constants by total energy minimization (a, c (in Å): Be, 2.26, 3.56; Zr, 3.23, 5.19) agree well with previous studies [33-34, 17-19].

First, we consider the Finnis-Heine (F-H) cut (Figure 2). The bulk is truncated along a hcp (0001) plane in the middle of neighboring layers. The force calculated consists of ion-ion repulsion and ion-electron attraction (Eq. (2)). The size of the summation is the stacking of 14 layers along c axis with 2929 atoms in each layer.

The directions of forces on the first layer atoms indicate that both for Be and Zr, the first inter-layer space should contract. This is the net result. The effect due to the force on the second layer atoms is also taken into consideration. The indication that the surface atoms should move toward the bulk is consistent with Finnis and Heine's work [2]. In their study, a uniform electron distribution was used to approximate the ideal surface, and the calculation demonstrated that the first inter-layer space of Al fcc (111) should contract. Since the force on the second-layer atoms is much smaller, our calculation in some sense is a more accurate LAPW version of the force I indicated in [4].

From Table A.1, both hcp (0001) Be [7-8, 17-19] and fcc (111) Al [6,14,26] expand actually, which simply suggests that Finnis and Heine's approximation of charge smoothing on closely packed surface is too simplified to give reliable directions of relaxation as noticed in the literature [14,7,22]. Until this stage our calculation has not yet included charge-smoothing processes. Still Finnis-Heine's picture predicted the trends that open surface contracts much more than close surface. These cross-checks may suggest that the capability of Finnis-Heine's picture in predicting the trends is more likely due to the topological similarity of this flat FH cutting boundary to that of the atoms near the surface than to the approximation of charge smoothing physically sound.

In the second type of fresh-cut surface (Figure A.2), the boundary is replaced by Wigner-Seitz cell as assumed in [1]. Now there are some electron convex outside

of the Finnis-Heine plane and some concave left inside. Our calculation indicated that for both Be and Zr, the forces point toward the vacuum, leading the surface atoms to expand away from the bulk. A test calculation adopting a uniform electron distribution also gave the similar result.

Since we know that the surface relaxation behaviors of Zr and Be are very different, comparing the above two different considerations of the surface density profiles may allow us to draw the conclusion that for hcp (0001) surface, it is possible to be a universal result that for F-H cutting the first inter-layer spacing should contract while for W-S cutting it should expand. Given that the force on the second layer atoms is quite small, this conclusion may be applicable to fcc(111) surfaces as well. This suggests that stopping at these two types of fresh-cut surfaces, we can not obtain an unambiguous understanding of the direction of surface relaxation. Some more physically sound density profiles taking into account the inherent difference of the bulk would be needed to give meaningful results.

A.3.2 Charge smoothing of ideal surfaces

Next, we compare the difference between hcp Be and Zr and look at their different trends of charge smoothing.

Shown in the top panels of Figure A.3 is how electrons are distributed in the fresh-cut hcp (0001) surfaces of Be and Zr. The valence electron density contour is obtained in the F-H plane. Since these regions are relatively far away from the nuclei

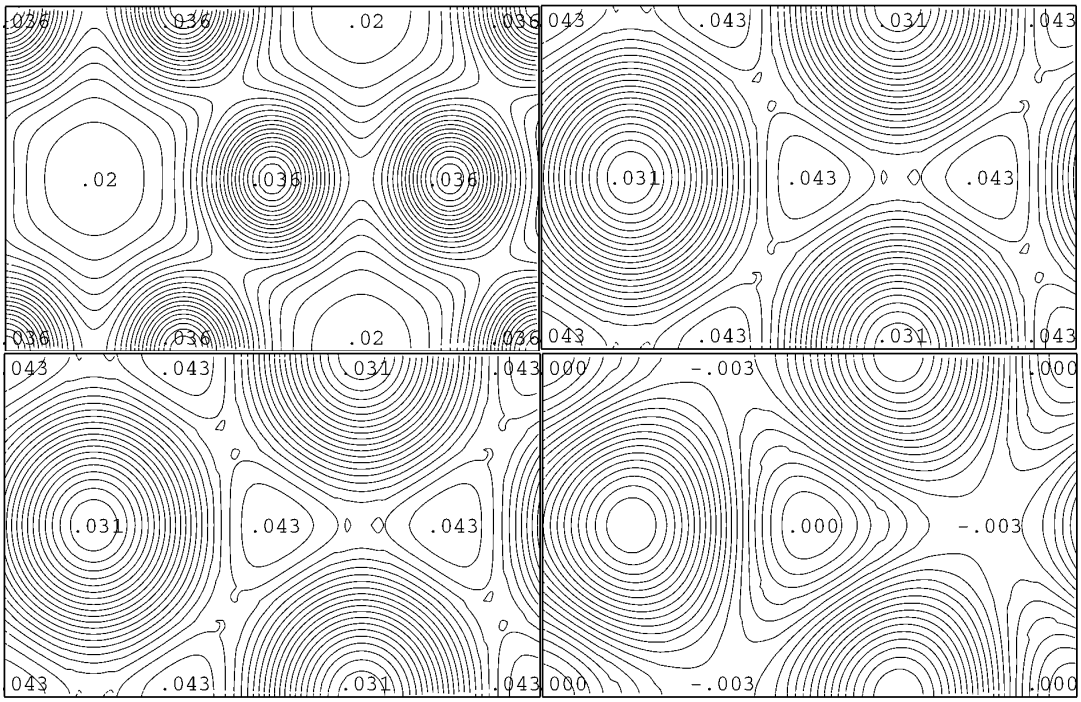

Figure A.3 Charge density profiles of Be and Zr. These density contour plots are along the Finnis-Heine plane. The upper two are the bulk distribution of Zr (left) and Be (right). Corresponding to the structure in Figure A.1, in each panel the four corners and the center represent the images of (4,5,7,8,6) while the other three maxima refer to those of (1,2,3). In Be, regions along the maximum points are called ridges, which indicate the formation of bonds. The bottom plots are the density difference between the first inter-layer F-H plane of the ideal surface and the bulk. In Zr (left), density right above (4,5,6,7,8) is decreased (-. 001), while that below (1,2,3) is maintained (.000). In between there's accumulation of charges (++) where the density is increased about .001. In Be (right), above (4,5,6,7,8) there is little change (.000) while below the first layer (1,2,3) the density is decreased (-. 003).

and are less bounded by the lattice potential, it is likely that after we split the bulk, electrons located there are severely disturbed. Although Zr has 4 valence electrons ($4d^2 5s^2$, in the calculation, the core states $4s^2$ $4p^6$ are also counted as valence electrons), its average density (0.025 electron per au3) is smaller than that of Be ($2s^2$) (0.037 electron per au3). In both cases, the maxima are located right above the nuclei (0.036 electron per au3 for Zr; 0.043 electron per au3 for Be). It is clear that Zr has a ion core more densely packed than Be does. In Be, although the interstitial charge density is minimal in the plane (0.031 electron per au3), its magnitude is still comparable with regions above the nuclei. These electrons are restricted by directional distribution of electrons along the ridges between neighboring maxima. These characteristics agree with previous study that in Be there is hybridization of s electrons with p orbital while its bulk property is semi-metallic and anisotropic [35,33-34]. For Zr, the interstitial space has fewer electrons, largely forming hollow regions. This is consistent with the general observation that electrons in d metals are more localized.

In the following, we analyze how charge smoothing occurs from the above fresh-cut surface. For charge smoothing to happen, the following two prequisites should be fulfilled: (1) there exist valence electrons to be smoothed and (2) there exist hollow regions energetically favorable to accommodate incoming extra electrons. As in Smoluchowsky's work [1], we adopt Weizsäcker's expression for the kinetic energy per volume of electron [36]:

$$K.E. = A\rho^{5/3} + B\frac{(\nabla\rho)^2}{\rho} \quad (5)$$

with $A = \frac{4\pi h^2}{5m}\left(\frac{3}{8\pi}\right)^{5/3}$, $B = \frac{h^2}{32\pi^2 m}$, and ρ is the density of electrons. From the above formula itself and if we only consider the importance of kinetic energy part in charge smoothing, we would draw the conclusion that electrons would more likely flow from bulk toward the vacuum space to decrease the corrugation and electron density. However, the lattice energy due to electron-ion attraction and the exchange energy due to the Pauli Principle favor a higher density distribution of electrons localized around the nuclei [37]. Theoretical calculation [38] shows that in metals of high valence electron density (Be, Al, Mg), the bulk kinetic energy is so high that it overcomes the exchange-correlation energy and leads to the formation of a large dipole layer near the surface, which contributes significantly to the work function. At low density, under the influence of a strong ion potential, the exchange-correlation effect becomes dominant, the spreading of charge toward vacuum is small, and the contribution of dipole layer to work function can be neglected.

Next we carry out self-consistent calculations to obtain the information of the ideal surfaces of hcp (0001) Be and Zr. For Be, the super cell of the surface is composed of 10 layers of atoms and the vacuum is 7 layers thick. The $\frac{1}{12}$ irreducible Brillioun Zone is sampled with 44 k points. For Zr, the super cell is composed of 10 layers of

atoms and 4.3 layers of the vacuum while the number of k points is 33. The other parameters are the same as that in the bulk calculations. Calculation of the cohesive energy and comparison of electron density in the middle region with the above bulk calculation show that the choice of these parameters is accurate enough for our purposes. Forces acting on surface atoms are obtained automatically by the WIEN97 software [39]. From the result given in Table A.2, it is clear that after the electrons are fully relaxed, the directions of forces acting the first layer atoms of the ideal surface are consistent with the results of the fully relaxed surface (Table A.1). For Be, the direction of force is the same as that of the W-S fresh-cut surface but the magnitude is decreased significantly. For Zr, the direction of force is the same as that of the F-H type and the scale is also decreased. For the comparison to be meaningful, we take the basic assumption that from either F-H or W-S fresh-cut surface, the ideal surface obtained after charge smoothing is the same. It is clear from Table A.2 that for these two types of fresh-cur surfaces, the force due to charge smoothing (δF_e^l in formula (1)) is too large to be negligible.

We compare the electron distribution of F-H fresh-cut surface with the ideal surface. Figure A.4 shows that for both Be and Zr, part of electrons spread out toward the vacuum; however the magnitude and extension of spreading in Be is much larger and longer than that in Zr. In the interstitial space between the first and second layer atoms, Be and Zr have dramatic difference (Figure A.3). In the middle region parallel

Table A.2 Forces on surface atoms with different boundary profiles

Be	Be	Zr
Finnis-Heine Cut	-37 mRy/a.u.	-229 mRy/a.u.
Wigner-Seitz Cut	38mRy/a.u.	254 mRy/a.u.
Ideal Surface	8.2 mRy/a.u.	-24 mRy/a.u.

Here negative number means the force direction is toward the bulk, leading to contraction; others mean expansion.

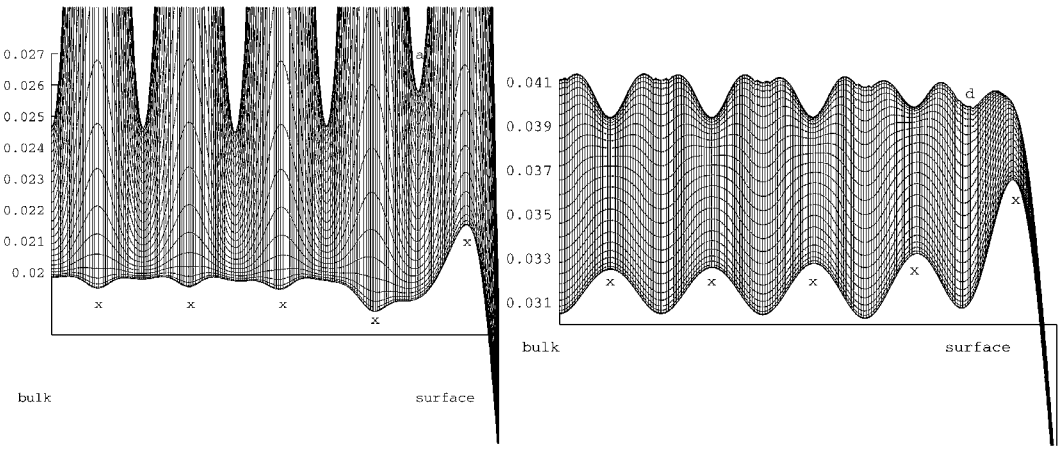

Figure A.4 Variation of interstitial charges near surfaces. This is the dispersion along [0001] of the density distribution in a plane which is parallel to [0001] while passing through the line connecting the triangular center of (6,7,9) and (6,8,10). The origin is the center of the super cell. The vertical axis (electron per au^3) refers to the dispersion of the electron density along the direction perpendicular to [0001] in this plane. "x"s are where the nearby atom 6 or 1 located. For Zr (left), this plane is close to the ion core and the variation is too large and we truncate the top to accommodate the illustration. Both for Be and Zr, the electron distribution near the surface becomes more uniform and the density is increased. The decay of charge in Zr is much sharper than that in Be. The "a" in Zr refers to the accumulation of charge in this region. The "d" refers to the depletion in Be.

to F-H plane, on average the charge density (electron per au^3) is decreased 0.0006 in Be and increased 0.0004 in Zr respectively. For Zr, it corresponds to the chemical picture of strengthening back bonding [22,29] near the surface for d metals. For Be, it suggests that even part of electrons in this region have rushed out into the vacuum.

The above difference is consistent with our knowledge of the difference of band structures between Be and Zr. In the band structure of crystal Be, the lowest vacant states on average are about 1 ev above the Fermi surface [33-34], which makes the bulk-like interstitial space energetically unfavorable to accommodate any extra electrons. Between these vacant states and Fermi level, there can exist many surface states. In the bulk band structure of Zr, the vacant states are very close to the Fermi surface, on average about 0.2 eV above the Fermi level [40]. These band structure characters are given from our bulk calculations as presented in Figure A.5. Energetically, when electrons smooth into the interstitial space between the first and second layer atoms, these states are possible to hold electrons coming from the region exposed to the vacuum. This agrees with Feibelman's chemical picture that in Zr there are extra d orbitals to hold demoted electrons, which does not exist in Be [22].

A.4 Summary

Based on full potential LAPW calculations we considered several possible ways to predict and explain the abnormal difference of surface relaxation between Be

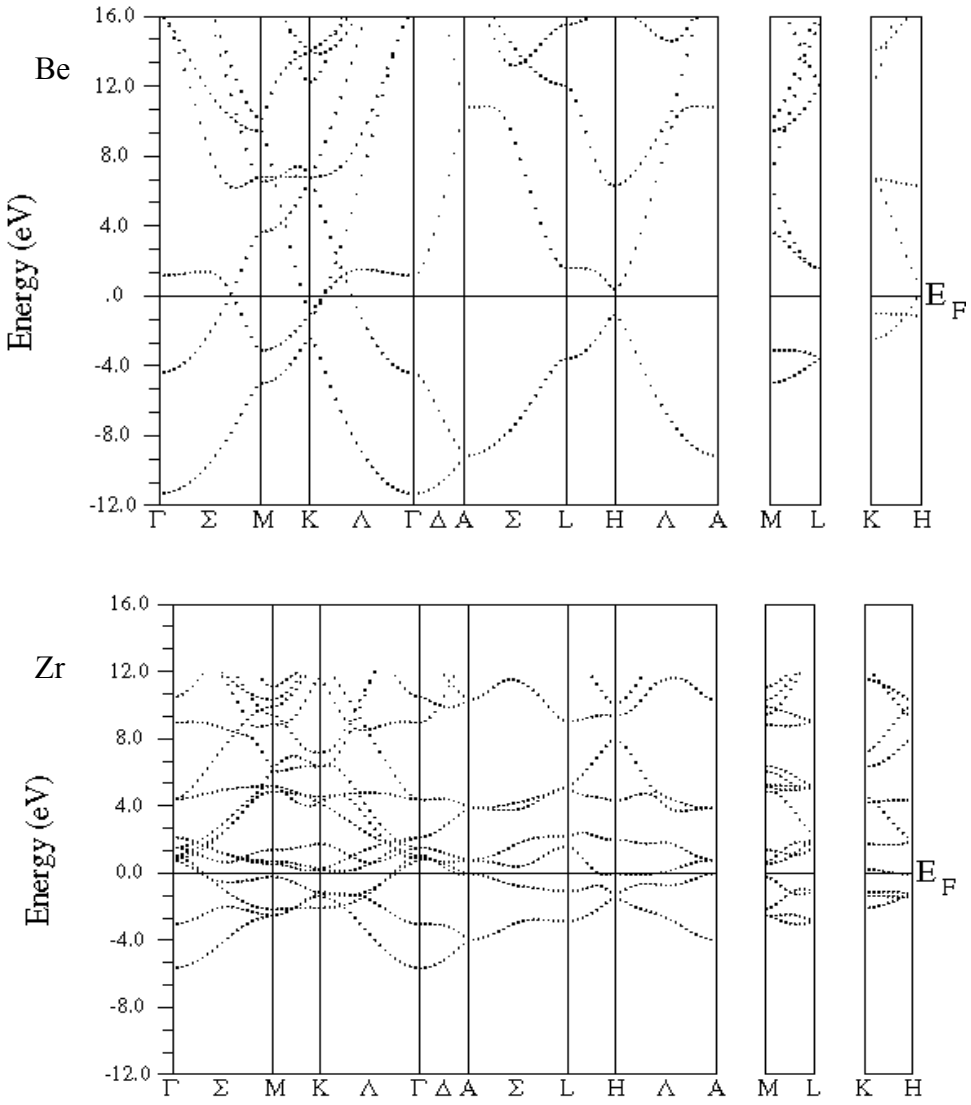

Figure A.5 Band structures of bulk Be and Zr. Here we can notice that at the region close to the surface, there exist many empty low energy states for Zr. For Be, however, such states are few.

and Zr from their respective bulk information. Beginning with the fresh cut of the bulk, we tracked the problem of surface relaxation by emulating the process of dynamic response. How the electrons smooth from fresh-cut surface to ideal surface is closely related to the properties of the crystal. For Be, the overall high valence charge density, delocalized distribution, and a large band gap provide the mechanism that during charge smoothing, electrons are more likely to spread out into the vacuum to form a layer of free electrons floating above the surface. This depletes electrons between the first and second layers and leads the first inter-layer spacing to expand. For Zr, the strong ion potential, the trends of localized distribution of valence charge, and the abundance of low lying vacant states above the Fermi level make it favorable for part of electrons to shift inside. This increases the bonding between the first and second layers and leads the first inter-layer space to contract. Besides Finnis-Heine and Wigner-Seitz boundaries, it may be possible to construct other types of cutting boundary between atoms so that the effect of the charge smoothing would be smaller. If it exists, the prediction of the direction of surface relaxation from the bulk information as indicated in Eq. (4) will be more reliable. Despite that the relaxation behaviors of (0001) Be and Zr surfaces are quite different, our test of Finnis-Heine and Wigner-Seitz boundaries give the same direction. It is possible that following the interstitial region where the electron density is minimal there may be a choice. Along this minimal contour, the bonding is weak and the charge smoothing of fresh-cut surfaces could be small. So far our test of this minimal contour is disappointing

because of the demanding of the computational details and highly accurate electron density distributions.

A.5 Discussion

A.5.1 Multilayer relaxation

So far our discussions are limited to the relaxation behaviors on close-packed surface structures, in which the forces on deeper layers are quite small. It is possible that surface relaxation is not limited in the first layer and can propagate deeper into the bulk. In Table A.3 we give our multilayer relaxations results on several metallic surfaces. These are calculated using the WIEN97 code as mentioned previously. The details are to be presented in Appendix B. It is clear that on open surfaces the relaxation has oscillatory behaviors. On closely packed surface (Be (0001)), the relaxation essentially limited to the first layer. Experimentally, Davis and co-workers used LEED to determine the possible importance of multi-layer relaxation as early as 1978[41]. As mentioned in the introduction, Alldrege and Kleinman predicted a contraction of 20% on Li (001) [4]. In the theoretical investigation of the importance of multi-layer in 1980 [42], Landman et al also noted that on Li (001) the multi-layer relaxation could be important. Barnett et al [43] found that multi-layer relaxations can have some oscillatory behavior with a periodicity equal to the bulk layer stacking period. Later Jiang et al [44] and Adams et al [45] showed that the qualitative trends

Table A.3 Multi-layer relaxation

Results	Be(10$\underline{1}$0)	Mg(10$\underline{1}$0)	Al(110)	Cu(110)	Be(0001)
Dd_{12} / d_{12}	-22.80%	-13.88%	-9.43%	-10.04%	2.2%
Dd_{23} / d_{23}	5.63%	6.90%	3.88%	4.09%	0.5%
Dd_{34} / d_{34}	-13.10%	-7.25%	-3.13%	-0.89%	0.4%
Dd_{45} / d_{45}	3.67%	3.59%	-0.08%		
Dd_{56} / d_{56}	-4.94%	-1.93%			

Here we have calculated the multi-layer relaxations on Be hcp (1000), (1010), fcc (110), Mg hcp (1010), Al fcc(110) and Cu fcc(110). Details of the calculation are described in Appendix B.

of the multilayer relaxation of open metal surfaces can even be predicted by calculating the electrostatic forces on the layers of the unrelaxed structures. They simply used uniform electronic background and point ions. This was also confirmed by our test on Mg (1010). First principles calculations by Ho et al [46] also suggested the correlation of the stacking sequence with the oscillation of the multi-layer relaxation. In the calculation of force, it is important to represent the three-dimensional nature of the electron density [43, 46] instead of the one-dimensional profile as originally used by Lang and Kohn [6]. Eguiluz [47] studied the multi-layer relaxation of Al (110) within the frame of perturbation theory, which suggested that the screening of the ions by mobile sp electrons play an significant role. This study also suggested that the convergence of the relaxation be very slow with the thickness of the slab. Increasing the thickness of the slab is accompanied by decreasing of the scale of the relaxation. The predicted scale is smaller than that from other theories and LEED experiments. However, other theoretical calculations and experiments have never gone as deep as the ninth layer to check the convergence. It is unclear whether this slow convergence is due to the limitation of the perturbation frame or it does be the nature. It is possible that Al is not a simple sp-bonded metal and the coupling can not be treated in a perturbation approach. Recently Cho et al [48] suggested that Friedel oscillation can make a significant contribution to multi-layer relaxation. In their study, there indeed exists an agreement of the oscillatory change of the electronic density and the oscillatory variation of the sign of the total force on

the ideal surface ions. According to Eq. (3), to judge whether the charge redistribution is dominant in the relaxation process, it is necessary to deduct the part of force contributions from the fresh-cut surface. As observed in [44-46] and our own test, a simple uniform electronic background would give an oscillatory force as well. To further complicate the answer to the question of whether electrostatic effect (Eq (2)) or Friedel oscillation (Eq. (4)) is dominant, in these studies the choice of the fresh-cut boundary is not physically defined. The jellium edge usually adopted is the Finnis-Heine cut of the fresh-cut surface. Changing a boundary will give different redistribution behavior. However, it is likely that the periodicity of the oscillation would remain.

A.5.2 Thermal expansion of surface relaxation.

Usually ab initio calculations are carried out at 0K while experiments at temperatures much higher. Our previous discussion of the surface relaxation is used at 0K. Generally, it is expected that due to the entropy effect, the lattice constant should be expanded upon increasing the temperature. However, this is for systems of homogeneous lattice atoms and simple lattice structures. In systems where the homogeneity of the lattice atoms disappears, it is likely that the thermal expansion of the system is not uniform any more, which can lead to the fact that some inter-atomic space contracts upon the increase of the temperature. For bulk systems negative thermal expansions have been found in systems such as ZrW_2O_8 [49,57,58], $H_fW_2O_8$

[58], and some semiconductors [50]. On surfaces, due to the broken of symmetry perpendicular to the surface, the inhomogenity of lattice atoms increases significantly. We can understand the occurrence of thermal expansion through the change of anharmonicity and/or the softening of the vibration frequency. On Al(110)[51], Be(10$\underline{1}$0) [56], Mg(10$\underline{1}$0)[52], Cu(100)[53] there have been observations of negative thermal expansion in certain temperature regime in LEED experiment. Study of Al(110) using molecular dynamics [54] indicated that a localized vibration mode perpendicular to the surface in the second layer is responsible for the negative thermal expansion. (See Figure A.6). However, they obtained the information through the mean square displacement of atoms, which is not the right quantity to justify their claim that the underlying reason was anharmonicity. Here it is essential to notice that due to the symmetry breaking perpendicular to the surface, it is possible that the asymmetry can even influence the harmonic coefficient of each layer. Let us take a mean field approximation and assume that along the direction perpendicular to surface, each layer of atoms are vibrating independently in the mean field provided by other atoms. We may expand the total energy of the system as

$$E = \sum_i c_i z_i^{\,2} - g_i z_i^{\,3} - f_i z_i^{\,4} \qquad (6)$$

Here z_i is the displacement of atoms in the layer i around its equilibrium state perpendicular to the surface. In the terminology of Kittel [55], the cubic term represents the asymmetry of the mutual repulsion of the atoms and the fourth-order

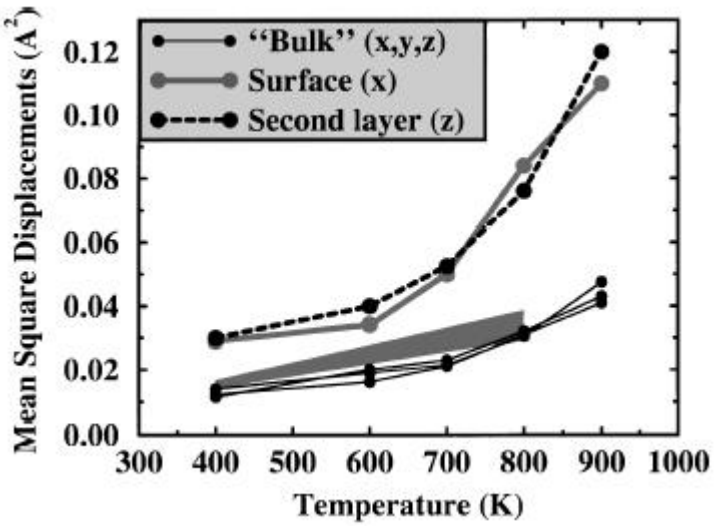

Figure A.6 Layer-resolved mean square displacements on Al(110). The shaded area corresponds to the bulk experimental values of Ref.19 there. ([54]).

term represents the softening of the vibration at large amplitudes. Also he regarded all terms higher than the second order as the anharmonic term. The mean displacement $<z_i>$ and mean square displacement$<z_i^2>$ can be evaluated from

$$< z_i^{\,n} >= \frac{\int z_i^{\,n} e^{-E/k_B T} dz_1 dz_2 \ldots}{\int e^{-E/k_B T} dz_1 dz_2 \ldots} \qquad (7)$$

. We can obtain that

$$< z_i >= \frac{3g_i}{4c_i^{\,2}} k_B T \qquad (8)$$

$$< z_i^{\,2} >= \frac{k_B T}{2c_i} + \frac{15(k_B T)^2}{8c_i^{\,3}} f_i \qquad (9)$$

It is clear from above that analysis of the mean square displacement misses the contribution from the lower order contributions such as the cubic term. The result from [54] is given in Figure 6. In the framework of Eq.(9), it does indicate that the fourth-order term is important in the outmost two layers. One more significant point from Eq.s (8) and (9) is that, given the strong reliance of deviation ($<z_i>$and $<z_i^2>$, it is essential to recognize that to each layer, it can assume a different harmonic coefficient c_i. This difference can also give significant contribution to the expansion or contraction of the inter-layer spaces.

We have performed LAPW calculations (T=0K) to check this possibility. The details of the calculation of the ground state are given in Appendix B. In calculating the

difference of the harmonic term, we allow the atoms in each specific layer to shift above or below their positions in the ground state. The positions of atoms in other layers are fixed. Due to the limitation of computation power, we only have 7 points to fit. To decrease the error due to the limitation of data point, we only fit the energy to the harmonic term. Calculations are carried out on Al(110), Cu(110), Mg (1010) and Be(0001) surfaces. Table A.4 list the result in terms of the vibration frequency $w_i = \sqrt{\frac{c_i}{m}}$. Figure A.7 gives the fitting of the outmost four layers for Al(110). The bottom point in the well indicates the position of the ground state. Since the sample points are

From Table A.4 we can notice that the softening of the vibration frequency is different between Be(0001) and other open surfaces. For the open surfaces Al(110), Cu(110), Mg (10$\underline{1}$0), they indicate somehow the formation of double layers, in the sense that the frequency of the outmost layer w1 are only slightly different from ω_2 while ω_2 is significantly smaller than ω_3. According to Eqs. (8) and/or (9), this inhomogeneous softening of the vibration frequencies has the chance to give inhomogeneous thermal expansions with some interlayer spaces indicating negative thermal expansion while others with positive thermal expansion. Table A.4 also indicate that ω_4 of Al(110) and Mg(1010) is smaller than ω_3. It is not clear whether this is a physical fact or an artificial result due to the limitation of the thickness of the slab calculations. For Be(0001), the situation is different. ω_1 is about 30% smaller

Table A.4.Layer-by-layer variation of vibration frequencies. (Unit is in Hz).

	Be(0001)	Al(110)	Mg(10$\underline{1}$0)	Cu(110)
w_1	1.921×10^{12}	1.088×10^{12}	7.325×10^{11}	8.701×10^{11}
w_2	2.847×10^{12}	1.163×10^{12}	7.711×10^{11}	8.680×10^{11}
w_3	2.994×10^{12}	1.615×10^{12}	1.032×10^{12}	1.083×10^{12}
w_4		1.428×10^{12}	9.795×10^{11}	

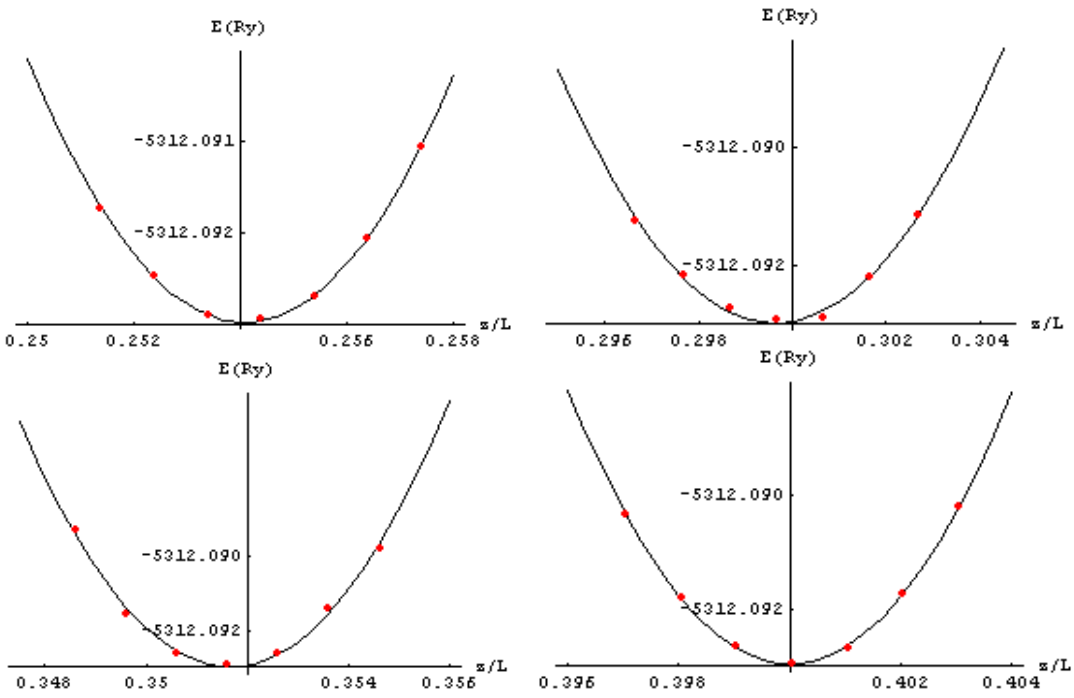

Figure A.7 Mean-field study of inter-layer coupling on Al(110). Shown is the variation of total energy with the shift of each layer perpendicular to the surface. The curves are obtained with parabolic fitting to the data as indicated by the points in each panel.chosen to be equally displaced away from the optimal position, the asymmetric distribution of energies does indicate the existence of anharmonicity terms.

than ω_2. It is also much smaller than that expected from the simple count of the loss of nearest-neighbors, which gives a softening of 13.4%. This is consistent with the experimental observation of unusually large thermal expansion of the outmost inter-layer space [8].

References

[1] R. Smoluchowsky, Phys. Rev., 60, 661(1941)

[2] M W Finnis and Volker Heine, J. Phys. F: Metal Phys., 4, L37(1974)

[3] M R Martin and G A Somorjai, Phys. Rev. B, 7 ,3607(1973)

[4] G. P. Alldredge and L. Kleinman, J. Phys. F: Metal Phys., 4, L207(1974); Phys. Rev. B, 10, 559(1974); Phys. Lett, 48A, 337(1974)

[5] F W de Wette and G E Schacher, Phys Re. 137, A78, A92(1965) ; erratum 138 AB4; CA Sholl, Proc. Phys. Soc., 91 434(1967)

[6] N D Lang and W Kohn, Phys. Rev. B,1, 4555(1970)

[7] H. L. Davis, J.B. Hannon, K.B. Ray, and E.W. Plummer, Phys. Rev. Lett., 68, 2632(1992)

[8] K. Pohl, Jun-hyung Cho, K. Terakura, M. Scheffler, and E. W. Plummer, Phys. Rev. Lett., 80, 2853(1998)

[9] P. T. Sprunger, K. Pohl, H. L. Davis and E. W. Plummer, Surf. Sci., 297, 48(1993)

[10] H. D. Shih, F. Jona, D. W. Jepsen, and P. W. Marcus, J. Phys. C, 9, 1405(1976)

[11] Y. M. Wang, Y. S. Li, K. A. R. Mitchell, Surf. Sci., 343, L1167(1995)

[12] G. Michalk, W. Moritz, H. Pfnr and D. Menzel, Surf. Sci., 129, 92(1983)

[13] P. J. Feibelman, J. E. Houston, H. L. Davis, and D. G. O'Neill, Surf. Sci., 302, 81(1994)

[14] Al(111): J. R. Noonan and H. L. Davis, J. Vac. Sci. Tech. A, 8, 2671(1990)

Ni(111): J. E. Demuth, P. M. Marcus, and D. W. Jepsen, Phys. Rev. B 11, 1460(1975)

Cu(111): S. , Lindgren, L. Walldin, J. Rundgren and P. Westrin, Phys. Rev. B, 29, 576(1984)

Pb(111): Y. S. Li, F. Jona, P. M. Marcus, Phys. Rev. B, 43, 6337 (1991)

[15] N. Materer, U. Starke, A. Barbieri, R. Dll, K. Heinz, M. A. Van Hove, G. A. Somorjai, Surf. Sci., 325, 207(1995)

[16] M. Methfessel, D. Hennig, and M. Scheffler, Phys. Rev. B, 46, 4816(1992)

[17] P. J. Feibelman, Phys. Rev. B, 46, 2532 (1992);

[18] N.A.W. Holzwarth andY. Zeng, Phys. Rev. B, 51, 13653(1995)

[19] R. Stumpf and P. J. Fiebelman, Phys. Rev. B, 51, 13748(1995)

[20] A. F. Wright, P. J. Feibelman, and S. R. Atlas, Surf. Sci., 302, 215(1994)

[21] Masahiru Yamamoto, C. T. Chan and K. M. Ho, Phys. Rev. B, 50, 7932(1994)

[22] P. J. Feibelman, Phys. Rev. B, 53, 13740(1996)

[23] Jun-hyung Cho and Kiyoyuki Terakura, Phys. Rev. B, 56, 9282(1997)

[24] M. Y. Chou and James R. Chelikowsky, Phys. Rev. B,35, 2124(1987)

[25] S.P. Chen, Surf. Sci., 264, L162(1992).

[26] Roland Stump ans Matthias Scheffler, Phys. Rev. B, 53, 4958(1996)

[27] Th. Rodach, K. P. Bohnen and K. M. Ho, Surf. Sci., 286, 66(1993); K.P. Bohnen, and K.M. Ho, Surf. Sci. Rep., 19, 99(1993)

[28] P.J. Feibelman, J. S. Nelson, and G.L. Kellogg, Phys. Rev. B, 49, 10548(1994)

[29] L. Pauling, The Nature of the Chemical Bond, 3rd ed. (Cornell University Press, Ithaca, NY, 1960).

[30] Tianjiao Zhang, unpublished

[31] P. Blaha, K. Schwarz, and J. Luitz, WIEN97, Vienna University of Technology 1997, (improved and updated UNIX version of the original copyrighted WIEN-code, which was published by P. Blaha, K. Schwarz, P. Sorantin, and S. B. Trickey, in Comput. Phys. Commun. 59, 399(1990))

[32] J. P. Perdew and Y. Wang, Phys. Rev. B, 45, 13244(1992);

J. P. Perdew, S. Burke and M. Ernzerhof, Phys. Rev. Lett., 77, 3865(1996)

[33] M. Y. Chou, Pui K. Lam, and Marvin L. Cohen, Phys. Rev. B, 28, 4179(1983)

[34] P Blaha and K Schwarz, J. Phys. F:Met. Phys., 17, 899(1987)

[35] Donald J. Silversmith and B. L. Averbach, Phys. Rev. B, 1, 567(1970)

[36] C. F. von Weizsäcker, Zeits. f. Physik 96, 431(1935)

[37] N. W. Ashcroft and N. D. Mermin, Solid State Physics, (Holt, Rinehart and Winston, 1976), 330-350; Gerald A. Mahan, Many-Particle Physics, (Plenum Press,

New York, 1990), 379-413

[38] N. D. Lang and W. Kohn, Phys. Rev. B, 3,1215(1971); H. L. Skriver and N. M. Rosengaard, Phys. Rev. B, 46, 7157 (1992)); R. M. Nieminen and C. H. Hodges, J. Phys. F, 6, 573(1976); R. N. Barnett, Uzi Landman, and C. L. Cleveland, Phys. Rev. B, 28, 1685(1983)

[39] B. Kohler, S. Wilke, M. Scheffler, R. Kouba, C. Ambrosch-Draxl, Comp. Phys. Commun. 94, 31(1996)]. The force produced by WIEN97 takes into account Pulay correction (P. Pulay, Mol. Phys., 17, 197(1969)) due to insufficiency of the basis function and the possible discontinuity at muffin-tin spheres. When calculating the force of fresh-cut surface, we try to improve the accuracy of the bulk charge distribution so that our comparison of this force to that of the ideal surface is of certain meaning.

[40] O. Jepsen, O. Krogh Andersen and A. R. Mackintosh, Phys. Rev. B, 12, 3084 (1976)

[41] J. R. Noonan, H. L. Davis and L. H. Jenkins, J. Vac. Sci. Technol. 15, 619(1978)

[42] U. Landman, R. N. Hill, and M. Mostoller, Phys. Rev. B,21,448(1980)

[43] R. N. Barnett, U. Landman, and C. L. Cleveland, Phys. Rev. B, 28,1685(1983)

[44] P. Jiang, P. M. Marcus and F. Jona, Solid State Commu., 59, 275(1986)

[45] D. L. Adams, V. Jensen, X. F. Sun and J. H. Vollesen, Phys. Rev. B, 38, 7913(1988)

[46] K. M. Ho, K. P. Bohnen, Phys. Rev. B, 32, 3446(1985)

[47] A. G. Eguiluz, Phys. Rev. B, 35, 5473(1987)

[48] Jun-Hyung Cho, Ismail, Z.Y. Zhang, E.W. Plummer, Phys. Rev. B,59,1677(1999)

[49] G. Ernst, C. Broholm, G. R. Kowach, and A. P. Ramirez, Nature, 396, 147(1998)

[50] S. Biernacki and M. Scheffler, Phys. Rev. Lett., 63, 290(1989) and references therein.

[51] H. Göbel and P. von Blanckenhagen, Phys. Rev. B, 47, 2378 (1993)

[52] Ismail, E. W. Plummer, M. Lazzeri, S. de Gironcoli, Phys. Rev. B,63,233401 (2001)

[53] A. Baddorf et al, unpublished

[54] N. Marzari, D. Vanderbilt, A. De Vita, and M. C. Payne, Phys. Rev. Lett., 82, 3296(1999)

[55] Charles Kittel, Introduction to Solid State Physics (7th), (John Wiley & Sons, Inc.,1996)

[56] Ismail, Ph. Hofmann, A. P. Baddorf, and E. W. Plummer, Phys. Rev. B 66, 245414 (2002)

[57] T. R. Ravindran, A. K. Arora, and T. A. Mary, Phys. Rev. B 67, 64301 (2003)

[58] Y. Yamamura, N. Nakajima, T. Tsuji, M. Koyano, Y. Iwasa, S. Katayama, K. Saito, and M. Sorai, Phys. Rev. B 66, 14301 (2002)

Appendix B Electronic Corrugation on Perfect Metallic Surfaces

In the studies that we have presented in chapters 3-5, the experimental data provided by STM are significant in helping our understanding. A significant part of our effort has been on the interpretation of STM images. As real surface structures always have defects, it will be very helpful in our understandings if we can have some knowledge of the surface morphologies of perfect surfaces without any defects. In this Appendix, we present our ab initio calculation results of the electronic corrugations on several perfect metallic surfaces. These calculations indicate that the partial electronic density profiles comparable to experimentally obtained STM images can have non-trivial features independent of the substrates even on open surfaces.

B.1 Theory for the Calculation of STM images

A full simulation of STM imaging system using ab inito calculation is still a computational challenge. The ab initio calculation carried out here is of an half-infinite defect-free surface structure. To make the comparison with STM image, we need some analytic approach to model the tunneling behavior between the STM tip and the surface electrons. Here we choose the model used by Tersoff and Hamann

[2]. The analysis is along the line of Bardeen's perturbation theory [22] for interpreting tunneling phenomena through metal-insulator-metal junction [23].

In the framework of perturbation theory and long-time approximation as implied in the Fermi golden rule, the tunneling current can be written as

$$I = \frac{2\pi e}{\hbar}\sum_{\mu\nu} f(E_\mu)[1 - f(E_\nu + eV)]\left|M_{\mu\nu}\right|^2 \delta(E_\mu - E_\nu) \qquad (1)$$

where *f(E)* is the fermi-Dirac distribution function and V the applied voltage. The matrix M represents the integration of the perturbation term H_{st} between tip states and sample states. This is defined as

$$M_{\mu\nu} = \int \phi^*{}_\nu H_{st} \psi_\mu dV \qquad (2)$$

where ϕ, ψ are unperturbed wave functions of the tip and sample. The tip and sample are assumed to be independent and unperturbed systems. Bardeen proved [22] that the tunneling matrix element can be evaluated by integrating a current-like operator over a plane lying in the insulator slab. In one-particle form, it takes

$$M_{\mu\nu} = -\frac{i\hbar^2}{2m_e}\int [\phi_\nu^* \nabla \psi_\mu - \psi_\mu \nabla \phi_\nu^*].d\mathbf{S} \qquad (3)$$

Tersoff and Hamann [2] simplified the tip as a spherical potential well of radius R. Using the s-wave to represent the tip state and assuming a low voltage, they obtained a linear dependence of the current with the electronic density of the sample at the tip position $\mathbf{r}_0$ at Fermi level E_F [2].

$$I \propto \sum_{\mu} \left|\psi_{\mu}(\mathbf{r}_0)\right|^2 \delta(E_{\mu} - E_F) \qquad (4)$$

This above formula has been used successfully to understand the topological image of gold [24]. Later Chen [6] extended this approach to tip states of higher angular moment. He showed that the tunneling current involves the first (second) derivative of the surface wave functions in the case of p (d) tip states. In the case of short tip-sample distance, the perturbation approach is not valid any more. Green's function method [5] and scattering theory [8,9] have been applied to understand these phenomena.

Our calculations presented here are limited in the framework of Tersoff and Hamann. The calculations are based on Eq. (4). Since we are solely interested in the change of electron density in a constant height mode, the linear constant is neglected.

B.2 Preparation of the Calculation

Calculations are performed in the following way. At first, the bulk lattice constants are obtained through the minimization of the total energy. Next, fully relaxed double-side slab calculations are carried out to obtain the information of the surfaces. The final step involves extracting the electron density distribution at a certain distance away from the surface in a narrow energy window around the Fermi energy. The choice of distance and energy window should be comparable with what are used in a typical STM experiment setup. These calculations are carried out with

WIEN97 code [19] as used in Appendix A. After the surface charge distribution in the real space becomes available, Fourier transformation (FT) is performed to obtain the distribution in the reciprocal space. Six surface structures are considered: hcp Be(0001), Be(10$\underline{1}$0), Mg(10$\underline{1}$0), fcc Al(110), Cu(110), and artificial fcc Be(110). The related input parameters are listed in Table B.1. The calculated bulk lattice constants and surface energies are given in Table B.2. The bulk lattice constants agree well with the results listed in the textbook [25]. The results of surface relaxation have been included in Table A.3. As discussed in Appendix A, the inter-layer distances of hcp Be(10$\underline{1}$0), hcp Mg(10$\underline{1}$0), fcc Al(110), fcc Cu(110), and artificial fcc Be(110) have oscillatory behavior as widely observed on open metal surfaces.

When calculating the STM image, we considered two energy windows, which involves the integration of the electron density contributions from Fermi energy to 340mev (wide) or 68mev (narrow) below. We also considered the empty state images and the characters are very similar to the results presented here. The tip-surface distance is also considered of two categories, 3.0Å (far) or 1.5 Å (close). This distance is considerably closer than what is generally assumed in experiments, which is about 4-5 Å. About this, we note the recognition of previous studies that LDA calculations can not reproduce physics well in the region faraway from the surface. In combination, each surface has 4 theoretical STM images under different situations. When the tip-surface distance is as close as 1.5 Å, it is very possible that the perturbation approach assuming negligible tip-sample interaction should fail to work

Table B.1 Parameters used in the calculation.

Parameters	Be(10$\underline{1}$0)	Mg(10$\underline{1}$0)	Al(110)	Cu(110)
Exchange-Correlation function	LDA	LDA	LDA	GGA
Mode	Non-relativity	Non-relativity	Non-relativity	Relativity
K points in reduced BZ	54	54	54	48
Max L for basis inside sphere	11	11	11	11
Max L for non-muffin-tin matrix	5	5	5	5
Plane wave cut-off	9	8.1	8.3	9.8
Potential and charge cut-off	13	13	13	17
Layers of atoms in surface slab	12	12	11	9
Vacuum space (Å)	10.6	14.5	14.4	10.5

Table B.2 Lattice constants and surface energies.

Results	Be(10$\underline{1}$0)	Mg(10$\underline{1}$0)	Al(110)	Cu(110)
Lattice Constant(Å)	2.22 (2.27) 3.52 (3.59)	3.13 (3.21) 5.10 (5.21)	4.00 (4.05)	3.63 (3.61)
Surface Energy(ev/ $Å^2$)	0.132	0.07	0.08	0.111

Values inside parenthesis are taken from [25].

any more. However, as a pure comparison of the reliance of partial electron density on the distance away from the surface, it is still meaningful.

B.3 Results of the Calculation

For the calculation with the condition of narrow energy window (65meV) and far tip-sample distance (3Å), which is closer to the experimental conditions, the charge distributions in the area of one surface rectangular unit cell and the Fourier Transform of the STM image for hcp(10$\underline{1}$0) Be and Mg and fcc(110) Al and Cu are presented in Figure B.1. Experimental STM images for Be hcp(1010) [14-15] and Cu fcc(110) [16] are presented in Figure B.2. All images are highly corrugated along ΓA (across atomic row); along ΓA (along atomic row), these materials show important difference. For Be, it is essentially flat and there is no corrugation along the atomic row. For Cu, there is slight corrugation along the atomic row. For Mg, the corrugation is a little larger. Of these metals, Al is the most corrugated along the atomic row, which is comparable to that across the atomic row. Images obtained for the other three conditions are qualitatively similar to the result shown in Figure B.1, despite that there is some quantitative difference. Somehow, the difference between Be hcp(1010) and Cu fcc(110) is not as dramatic as that indicated in Figure B.2. On the FT of STM for Be hcp (1010) in Figure B.2(c), essentially there is no indication of corrugation along M direction at all.

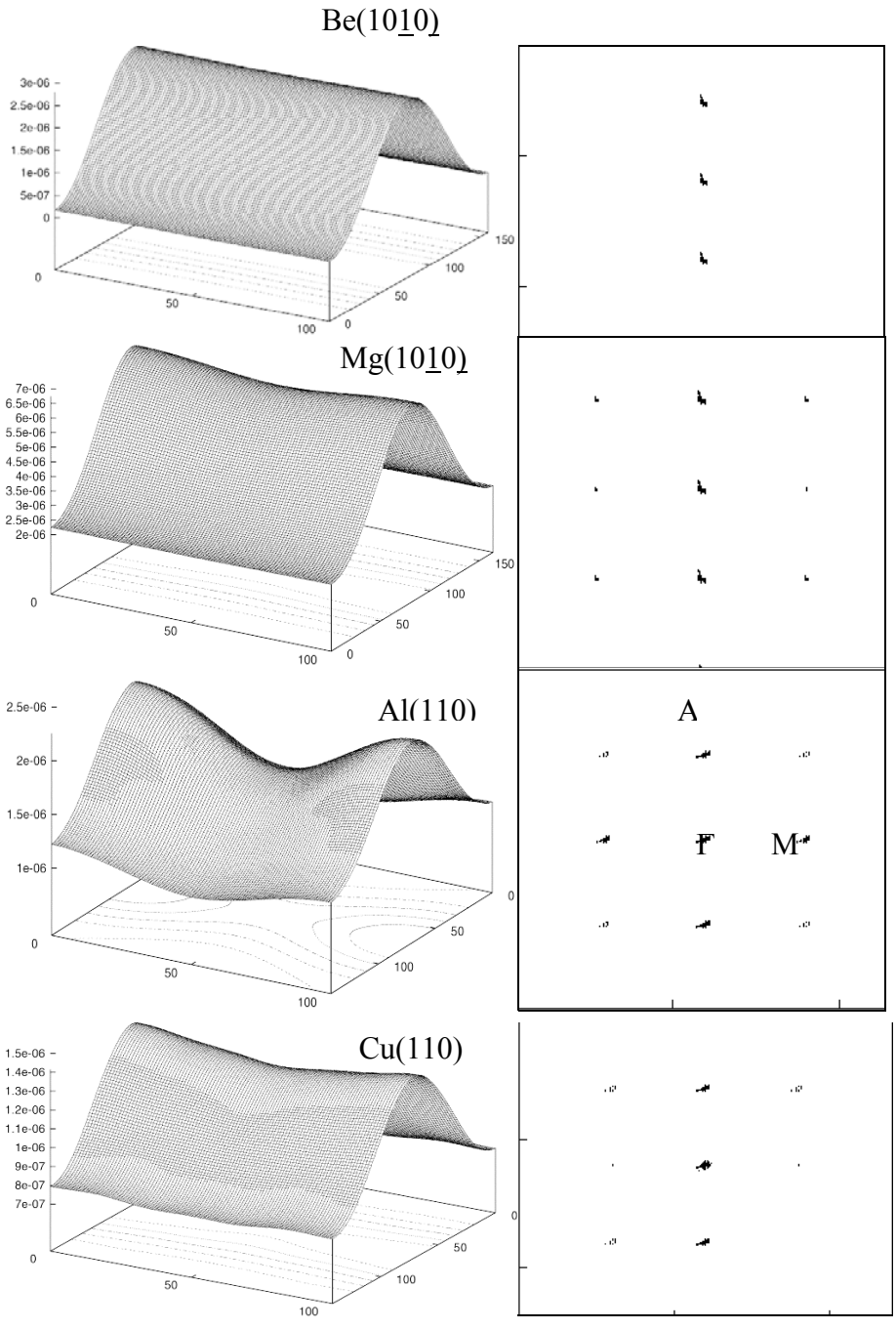

Figure B.1 Calculated (FT) STM images.

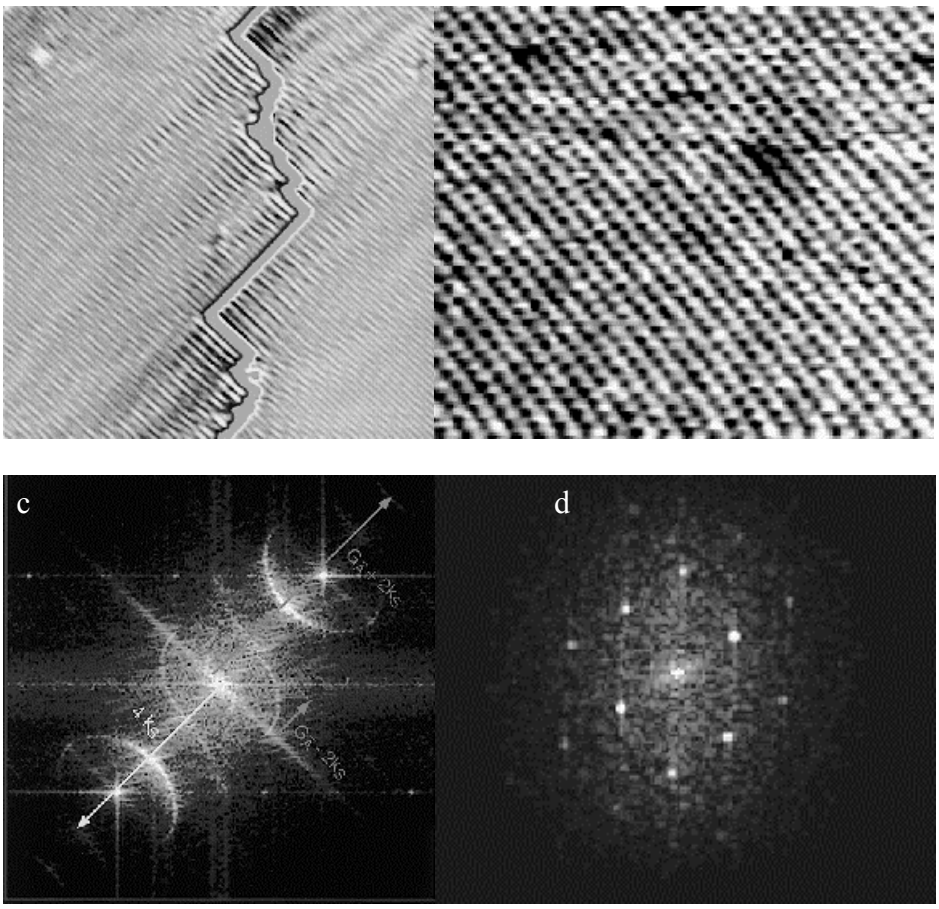

Figure B.2 Electronic corrugation on Be(10$\underline{1}$0) and Cu(110) surfaces. Shown here are STM images for (a) Be(10$\underline{1}$0) [13-14] (b) Cu(110) [15]. The tunneling current I (nA), bias V(mv) and temperature(K) T are (I, V, T) = (0.1, -50, 4), (1.1, 66, 237). Their corresponding FT-STM are shown in (c), (d).

For a quantitative comparison, the numerical results for the calculated FT of STM images are given in Table B.3. The intensity at the center of the reciprocal space (00) is defined to be 1; intensities at other points are relative to it. It indicates that the corrugation along the atomic row for Cu (110) is 2-20 times larger than that for Be (1010). However, the corrugation across the atomic row for Cu(110) is 2-10 times smaller than that for Be (1010). If we define anisotropy as the ratio of the intensity at A (across the atomic row) to that at M (along the atomic row), the above analysis means that the anisotropy of corrugation in Be (1010) (13-1000) is much larger than that in Cu (3-10), which explains the significant difference between STM images of Cu(110) and Be(10$\underline{1}$0) in Figure B.2. The unusual anisotropy of Be (1010) has been reported in [15]. This quantitative information also indicates the importance of quantificating image intensities in the data analysis, which can in certain degree exclude the ambiguity due to the resolution of the apparatus as indicated in Figure B.1.

To test whether the stacking sequence is the physical reason in bringing out the difference in the STM images, we constructed an artificial Be fcc(110) surface. The total energy per atom for bulk fcc Be is 0.04ev higher than that for hcp structure, which is consistent with the fact that Be assumes hcp structure. The quantitative information of calculated images for Be fcc(110) is given in Table B.4. It has some difference from that of (10$\underline{1}$0) structure, but the main feature is the same. This excludes stacking sequence as the (main) reason. However, it is still possible that the

Table B.3 Relative intensity of the Fourier-transformed electron density distributions on hcp (10$\underline{1}$0) of Be, Mg and fcc (110) of Al and Cu.

	Be(10$\underline{1}$0)	Mg10$\underline{1}$0)	Al(110)	Cu(110)
Narrow & close	1 (00) 0.5 (01) 0.03 (10)	1 (00) 0.3 (01) 0.04 (10)	1 (00) 0.3 (01) 0.2 (10)	1 (00) 0.3 (01) 0.1 (10)
Narrow & far	1 0.5 $3.0*10^{-3}$	1 0.3 0.01	1 0.1 0.06	1 0.1 0.01
Wide & close	1 0.4 0.03	1 0.2 0.03	1 0.3 0.2	1 0.2 0.06
Wide & far	1 0.4 $4.0*10^{-4}$	1 0.2 0.01	1 0.1 0.04	1 0.05 $7*10^{-3}$

influence of stacking sequence is different in different materials, which we can not be excluded as I have not carried out the corresponding calculation on the artificial hcp Cu(10$\underline{1}$0). In Table B.4 we compared the relative intensity of the charge corrugation on different surfaces of Be. It clearly indicates that the electron distribution on Be hcp(0001) is the least corrugated , which agrees with STM experiment [17].

B.4 Discussion and Summary

Based on tables B.3 and B.4, we make some discussion about the dependence of corrugation on voltage and the tip-sample separation. It is very clear that the closer the tip to the sample, more corrugated is the charge density distribution. The dependence of the corrugation with the bias is very weak, with a slight tendency that the larger the bias, the less corrugated the surface. This is different from recent calculations for Cr and Mn on Fe (001) [12] and bcc (110) surfaces of W, Ta and Fe [13], where strong dependence of corrugation amplitudes on the applied bias voltage is observed.

It is important to notice that so far we have utilized the simplicity of Eq. (4) to calculate the STM image. The comparison is also based on this formula. However, it is possible that (a) the tip-sample interaction is large, which leads to the distortion of the sample and/or the tip wave functions (b) the state of tip is not of s-wave nature. Both of these two factors can complicate the understanding of sample properties

Table B.4 Relative coefficient of the Fourier-transformed electron density distributions on different Be surfaces.

Be	Hcp(10$\underline{1}$0)	Fcc(110)	hcp (0001)
Narrow & close	1 (00) 0.5 (01) 0.03(10)	(00) 0.4 (01) 0.05 (10)	1 (00) $4.0*10^{-3}$ (01)
Narrow & far	1 0.5 $3.0*10^{-3}$	1 0.2 $1.0*10^{-3}$	1 $8.0*10^{-4}$
Wide & close	1 0.4 0.03	1 0.4 0.01	1 $4.0*10^{-3}$
Wide & far	1 0.4 $4.0*10^{-4}$	1 0.2 $1.0*10^{-4}$	1 $5.0*10^{-4}$

based on STM images. In understanding the electronic corrugation obtained from STM experiment, it is essential to distinguish the enhanced corrugation due to the tip state [6] and the variation of tip-sample coupling strength with the tip-sample separation from the intrinsic corrugation of the surface [26].

In summary, we have carried out ab initio calculations of STM images of several perfect metallic surfaces within the framework of Tersoff-Hamman approximation. The quantitative analysis of the electron density corrugation has achieved good agreement with experiment results.

References:

[1] M.H. Hettler, W. Wenzel, M.R. Wegewijs, and H. Schoeller, Phys. Rev. Lett., 90, 76805(2003); Ch. Loppacher, M. Guggisberg, O. Pfeiffer, E. Meyer, M. Bammerlin, R. Lüthi, R. Schlittler, J. K. Gimzewski, H. Tang, and C. Joachim, Phys. Rev. Lett. 90, 66107 (2003)

[2] J. Tersoff and D. R. Hamann, Phys. Rev. Lett., 50, 1998(1983); ibid, Phys. Rev. B 31, 805 (1985);ibid, Phys. Rev. Lett., 57, 440(1986)

[3] E. Stoll, Surf. Sci., 143, L411(1984)

[4] N. D. Lang, Phys. Rev. Lett., 55, 230(1985); ibid, 56,1164(1986)

[5] C. Noguera, Phys. Rev. B, 42, 1629(1988); ibid,J. of Microsc. 152, 23(1988)

[6] C.J. Chen, J. Vac. Sci. Technol. A, 6, 319(1988); ibid, Phys. Rev. Lett., 65,

448(1990); ibid, Phys. Rev. B, 42, 8841 (1990)

[7] T.E. Feuchtwang and P. H. Cutler, Phys. Scr. 35, 132(1987)

[8] R. Wiesendanger and H.-J. Güntherodt (Eds.) , Scanning Tunneling Microscopy III (2nd), (Springer, 1996)

[9] G.A.D Briggs and A.J Fisher, Surf. Sci. Rep., 33, 1(1999) and reference therein

[10] G. Binnig, H. Rohrer, Ch. Gerber, and E. Weibel, Phys. Rev. Lett., 49, 57(1982);ibid, 50, 120 (1983)

[11] R.J. Hamers, and U.K. Köhler, J. Vac. Sci. Technol., A7, 2854(1989); R. M. Feenstra, Phys. Rev. B, 44, 13791, (1991); W. Han, E. R. Hunt, O. Pankratov, and R. F. Frindt, Phys. Rev. B 50, 14746 (1994)

[12] S. Heinze, S. Blügel, R. Pascal, M. Bode, and R. Wiesendanger, Phys. Rev. B, 58, 16432(1998)

[13] S. Heinze, X. Nie,S. Blügel, and M.Weinert, Chem. Phys. Lett.,315, 167(1999)

[14] B.G. Briner, Ph. Hofmann, M. Doering, H.-P. Rust, E.W. Plummer and A.M. Bradshaw, Europhys. Lett. 39, 67(1997)

[15] Ph. Hofmann, B.G. Briner, M. Doering, H.-P. Rust, E.W. Plummer, and A.M. Bradshaw, Phys. Rev. Lett. 79, 265 (1997)

[16] L. Petersen, Ph. Hofmann, E. W. Plummer and F. Besenbacher, J. Electron Spectrosc. Relat. Phenom., 109, 97(2000)

[17] P. T. Sprunger, L. Petersen, E. W. Plummer, E. Lægsgaard, and F. Besenbacher, Science 275, 1764 (1997)

[18] L. Petersen, P.T. Sprunger, Ph. Hofmann, E. Lægsgaard, B.G. Briner, M. Doering, H.-P. Rust, A.M. Bradshaw, F. Besenbacher, and E.W. Plummer, Phys. Rev. B, 57, R6858 (1998) and reference therein.

[19] P. Blaha, K. Schwarz, and J. Luitz, WIEN97, Vienna University of Technology 1997, (Improved and updated UNIX version of the original copyrighted WIEN-code, which was published by P. Blaha, K. Schwarz, P. Sorantin, and S. B. Trickey, in Comput. Phys. Commun. 59, 399(1990))

[20] Tianjiao Zhang, L. Petersen, Z.Y. Zhang, E. W. Plummer, to be submitted

[21] B. Engels, P. Richard, K. Schroeder, S. Blügel, Ph. Ebert, and K. Urban, Phys. Rev. B, 58, 7799(1999)

[22] J. Bardeen, Phys. Rev. Lett. 6, 57(1961)

[23] I. Giaever, Phys. Rev. Lett. 5, 147(1960); 9, 147 (1962)

[24] G. Binnig, H. Rohrer, Ch. Gerber, and E. Weibel, Bull. Am. Phys. Soc. 28, 461 (1983); ibid, Surf. Sci., 131, L379(1983)

[25] Charles Kittel, Introduction to Solid State Physics (7th), (John Wiley & Sons, Inc.,1996)

[26] G. A. D. Briggs and A. J. Fisher, Surf. Sci. Rep., 33, 1(1999)

[27] E. Hulpke (Ed.), Helium Atom Scattering from Surfaces, (Springrt-Verlag,1992)

[28] N. Esbjerg, J. K. Nrskov, Phys. Rev. Lett. 45, 807(1980), M. J. Stott, E. Zaremba, Phys. Rev. B 22, 1564(1980)

Vita

Tianjiao Zhang was born in Sichuan, China. He obtained his Bachelor of Science from Department of Physics, Xiamen University in 1993. His minor was Semiconductor Physics. Later, he went to Department of Physics, Beijing University for Master Degree and graduated in 1996. There he did research on protein folding.

He went to US thereafter and studied chemistry in Dartmouth College for about two quarters. In the summer of 1997 he entered the Ph.D. program in Physics in the University of Tennessee, Knoxville and began working with Dr Zhenyu Zhang on Surface Sciences. In the end of 1999, he left for California to try his fortune in Corporate America. In the spring of 2003, he began to work with Dr Zhenyu Zhang again and completed his Ph.D. study.